Università degli Studi di Milano-Bicocca
Facoltà di Scienze Matematiche, Fisiche e Naturali
—
École Polytechnique, Palaiseau

The CMS Electromagnetic Calorimeter for the Higgs Boson Search $H \to ZZ^{(*)} \to 4e$ at the LHC

Coordinatore: prof. **Claudio Destri**

Tutori: dr. **Yves Sirois**
prof. **Tommaso Tabarelli de Fatis**

Tesi di Dottorato di
Federico Ferri
Matricola R00281

Scuola di Dottorato di Scienze
Corso di Dottorato di Ricerca in Fisica e Astronomia
XVIII ciclo – Anno Accademico 2004-2005

The CMS Electromagnetic Calorimeter for the Higgs Boson Search $H \to ZZ^{(*)} \to 4e$ at the LHC

Coordinatore:	prof.	**Claudio Destri**
Tutori:	dr.	**Yves Sirois**
	prof.	**Tommaso Tabarelli de Fatis**

Tesi sostenuta il giorno 10 gennaio 2006 presso l'Università degli Studi di Milano-Bicocca di fronte ad una commissione composta da:

dr.	Yves Sirois
prof.	Tommaso Tabarelli de Fatis
dr.	Philippe Bloch (referee)
prof.	Ezio Menichetti (referee)

Tesi di Dottorato di
Federico Ferri
Matricola R00281

Contents

Introduction

The Standard Model of electroweak interactions shows an incredibly good agreement between theory and experiments. However, it does not yet give an answer to a number of fundamental questions, namely the most important of all: the origin of particle mass. One of the mechanisms proposed to justify massive particles (and so to explain the breakdown of the $SU(2)_L \times U(1)_Y$ symmetry group, upon which the Standard Model theory is built) is based on a scalar field which will manifest itself through a massive scalar particle called Higgs boson, which remains to be found. Extensive direct and indirect searches for this particles have been carried out at the LEP2 experiment and have fixed a lower bound ($m_H > 114.4$ GeV/c^2 at 95% C.L.) and an upper bound ($m_H < 237$ GeV/c^2) to the mass of the Higgs boson, indicating a value of 114 GeV/c^2 at 95% C.L. as the best fit to the experimental values.

The work presented in this thesis has been carried out in the contest of the Compact Muon Solenoid (CMS) collaboration. CMS is one of the two general purpose experiments (in conjunction with ATLAS) which are being installed at the Large Hadron Collider (LHC) at CERN, along with two experiments dedicated to the physics of the b quark (LHCb) and to heavy ions (ALICE). LHC is a proton-proton collider with a nominal energy of 14 TeV/c^2 in the center of mass and a nominal luminosity of 10^{34} cm^{-2} s^{-1} and will allow to search for the Higgs boson in the full range of the allowed masses. The golden channel for the detection of what is favoured to be a "light" Higgs boson is via its decay into two photons, which will provide for the signal a clean experimental signature over the hadronic background. However, a decay channel that is remarkably important not only for the possibility to detect this particle but also for the determination of its properties (e.g. spin, CP, couplings to gauge fermions etc.) is the one in which the Higgs boson decays into a pair of electrons and positrons via an intermediate state of two Z bosons ($H \to ZZ^{(*)} \to 4e$). In this context, the electromagnetic calorimetry of the detector is particularly important and must offer

excellent energy and angular resolutions.
This thesis has focused on the characterization of the CMS electromagnetic calorimeter, both with test beam data and with simulation, and on the study of the expected performance of the CMS detector for the discovery of the Higgs boson in the channel $H \to ZZ^{(*)} \to 4e$.

After a theoretical overview of the Standard Model (chapter 1) the LHC collider and the CMS detector will be presented (chapter 2).
Chapter 3 illustrates the results of test beam studies devoted to the analysis of the electronic noise and of the signal amplitude reconstruction from the readout of the electromagnetic calorimeter.
The detailed simulation of the CMS detector allows for the study of the electron reconstruction inside CMS, which has to face the strong solenoidal magnetic field (4 T) inside CMS and the tracker material in front of the calorimeter. The results are presented in chapter 4.
Chapter 5 shows the analysis of the expected CMS performance for the sequential detection technique of the Higgs boson in the channel $H \to ZZ^{(*)} \to 4e$, using both a standard selection and a Neural Network approach to analyze the data.

Chapter 1

Standard Model Physics (and Beyond)

The theoretical path towards a unified theory of weak and electromagnetic interactions began in 1933 when Fermi proposed his theory of the β decay. It took more than four decades to reach what is now called the Standard Model of electroweak interactions which, together with the Quantum Cromo-Dynamics, provides at present the most accurate description of three of the known interaction of Nature with elementary particles and fields.

The aim in this chapter is not to give a complete and exhaustive description of the theory, but rather to illustrate its basic principles, their consequences and the fundamental questions that are still not fully answered.

1.1 General Concepts

The Feynman–Gell-Man Lagrangian describing weak $V-A$ interaction processes at low energy is manifestly non-renormalizable, since it contains operators with mass dimension of 6 (while a necessary condition for the renormalizability is the presence of operators with mass dimension less than or equal to 4). For example the Lagrangian describing the nucleon β decay and the muon decay is given by

$$\begin{aligned}\mathcal{L} = & -\frac{G_\beta}{\sqrt{2}}\overline{p}\gamma_\alpha(1-a\gamma_5)n\overline{e}\gamma^\alpha(1-\gamma_5)\nu_e \\ & -\frac{G_\mu}{\sqrt{2}}\overline{\nu}_\mu\gamma^\alpha(1-\gamma_5)\mu\overline{e}\gamma^\alpha(1-\gamma_5)\nu_e,\end{aligned} \tag{1.1}$$

where γ_α, γ_5 are Dirac matrices, $a \simeq 1.23$ is a constant determined experimentally. Remarkably, the coupling constants for the two processes, G_μ and G_β, are equal and usually denoted by G_F, called Fermi constant and roughly estimated by $((\hbar c)^3/300 \text{ GeV})^2$.
A possible remedy to the non-renormalizability is the introduction of a mediator for the point-like weak interaction providing a term in the matrix elements to fix the quadratic divergences in higher order perturbative calculations. This mediator must be a massive vector (to explain the short range of the weak force) and exist in nature in two charged states (to explain the charge-changing manifestations of the weak interactions). For a complete cancellation of all the divergences at all orders, a neutral vector boson is also required.
To satisfy all the requirements in a coherent and consistent way, three of what Weinberg calls "good ideas"('t Hooft, 2005) are needed: the quark model, the idea of gauge (or local) symmetry and that of spontaneously broken symmetry. In what follows, the attention will be focused on the last two aspects.

1.1.1 Local Invariance

Since its first formulation in Maxwells equations which unify electric and magnetic interactions (1864), the concept of gauge invariance has held an increasingly important role in the description of Nature and its fundamental interactions. The freedom of choosing many potentials to describe the same physics can in fact be reformulated in terms of a gauge symmetry in the Lagrangian. Such a reformulation leads to conserved charges (via Noethers theorem) and to other important consequences such as the introduction of new fields and interactions into the theory.

In electrodynamics, for example, requiring the fermion free-particle Lagrangian

$$\mathcal{L}_{\text{free}} = \overline{\psi}(i\gamma^\mu \partial_\mu - m)\psi \tag{1.2}$$

to be invariant under a local $U(1)$ symmetry $\psi \to e^{iq\alpha(x)}\psi$ suggests a redefinition of the derivative ∂_μ (so called covariant derivative) as

$$\mathcal{D}_\mu \equiv \partial_\mu + iqA_\mu(x), \tag{1.3}$$

where A_μ is a new vector gauge field. Provided that the gauge field A_μ transforms as

$$A_\mu(x) \to A_\mu(x) - \partial_\mu \alpha(x), \tag{1.4}$$

the object $\mathcal{D}\psi$ behaves in fact as the field ψ under a $U(1)$ phase rotation:

$$\mathcal{D}\psi \to e^{iq\alpha(x)}\mathcal{D}\psi. \tag{1.5}$$

The new invariant Lagrangian $\mathcal{L}$ becomes then

$$\mathcal{L} = \mathcal{L}_{\text{free}} - q\overline{\psi}\gamma^{\mu}\psi A_{\mu}, \tag{1.6}$$

where the last term couples the field A_μ to ψ: a new field (identified with the photon) has appeared in the theory.
To obtain the complete QED Lagrangian it suffices to introduce a kinetic term for the field A_μ, that is a locally invariant term depending on the field and its derivatives but not on ψ. It can be shown (see for example (Peskin and Schroeder, 1995)) that out of the four possible combinations only one fulfils the necessary requirements of renormalizability of the theory and good behaviour under discrete symmetries:

$$F_{\mu\nu} = \partial_\mu A_\nu - \partial_\nu A_\mu. \tag{1.7}$$

It will be useful in the following to notice that $F_{\mu\nu}$ can be rewritten as the commutator between two covariant derivatives:

$$\begin{aligned}[\mathcal{D}_\mu, \mathcal{D}_\nu] &= [\partial_\mu, \partial_\nu] + iq([\partial_\mu A_\nu] - [\partial_\nu A_\mu]) - q^2[A_\mu, A_\nu] \\ &= iq(\partial_\mu A_\nu - \partial_\nu A_\mu),\end{aligned} \tag{1.8}$$

that is

$$[\mathcal{D}_\mu, \mathcal{D}_\nu] = iqF_{\mu\nu}. \tag{1.9}$$

The complete QED Lagrangian is then

$$\mathcal{L}_{\text{QED}} = \mathcal{L}_{\text{free}} \; - \; q\overline{\psi}\gamma^{\mu}\psi A_{\mu} \; - \; \frac{1}{4}F_{\mu\nu}F^{\mu\nu}. \tag{1.10}$$

It must be stressed that A_μ is a massless field: a mass term would be in fact proportional to $A_\mu A^\mu$, thus violating the gauge invariance:

$$A_\mu A^\mu \to (A_\mu - \partial_\mu\alpha)\,(A^\mu - \partial^\mu\alpha) \neq A_\mu A^\mu. \tag{1.11}$$

Yang and Mills proved that when when the symmetry group is non-Abelian, the construction of the theory follows the same principles (Yang and Mills, 1954). The physical consequences are however different and are crucial for the description of the weak interactions. As an example, it can be

considered the invariance under a local transformation of the $SU(2)$ group (which in the original Yang-Mills paper was supposed to be the isotopic spin for a doublets of Dirac fields, the proton and the neutron). If the field ψ transforms as

$$\psi(x) \to G(x)\psi(x) \equiv e^{i\alpha^i(x)\frac{\sigma^i}{2}}\psi(x), \tag{1.12}$$

where σ^i are the group generators, then the covariant derivative takes the form

$$\mathcal{D}_\mu \equiv \partial_\mu - igB_\mu, \quad B_\mu \equiv b^i_\mu \frac{\sigma^i}{2}, \tag{1.13}$$

b^i_μ being three vector fields, one for each generator of the gauge symmetry group.
To assure the local invariance, B_μ must transform according to

$$B_\mu(x) \to G(x)\left(B_\mu(x) + \frac{i}{g}\partial_\mu\right)G^\dagger(x). \tag{1.14}$$

Following by analogy the Abelian case, the kinetic term for b^i_μ can be found and the Lagrangian completed. Indeed, considering a field-strength tensor built up with the commutator between two covariant derivatives one finds

$$[\mathcal{D}_\mu, \mathcal{D}_\nu] = -igF^i_{\mu\nu}\frac{\sigma^i}{2}, \tag{1.15}$$

with

$$F^i_{\mu\nu} = \partial_\mu b^i_\nu - \partial_\nu b^i_\mu - ig\left[b^i_\mu, b^j_\nu\right]. \tag{1.16}$$

Using the Pauli's matrix identity to simplify the kinetic term $(F_{\mu\nu})^2$ and expanding the covariant derivative, the Yang-Mills Lagrangian becomes

$$\mathcal{L}_{\rm YM} = \mathcal{L}_{\rm free} \; - \; \frac{g}{2}\overline{\psi}\gamma^\mu b^i_\mu \sigma^i \psi \; - \; \frac{1}{2}{\rm tr}F_{\mu\nu}F^{\mu\nu}. \tag{1.17}$$

As for the Abelian case, the symmetry completely dictates the form of the interaction, thereby leading to a richer scenario.
In addition to the gauge boson propagator and to the coupling of the gauge fields to the fermions, the theory has three- and four-gauge-bosons vertices (fig. 1.1), as a consequence of the non linear term in $F_{\mu\nu}$. These new self-interactions for the (massless) gauge bosons exist even without fermions, while Abelian gauge theories without fermionic fields are free (i.e. non-interacting) theories.
The principle of local invariance is a consistent way to have massless vector bosons candidates into the theory: in order to be used to describe the weak interactions, however, they must acquire a mass, hence requiring a spontaneous breaking of the symmetry. The mechanism by which this symmetry breaking occurs therefore needs to be identified.

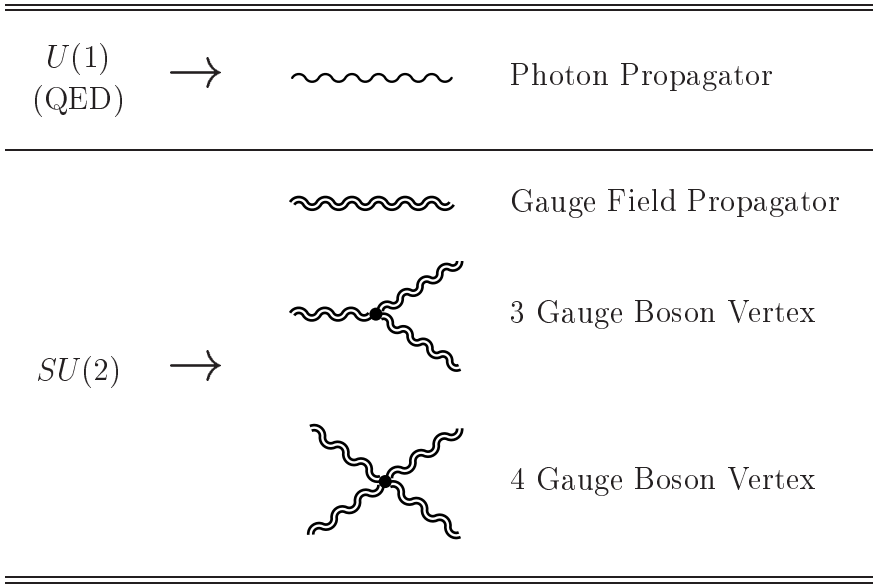

Figure 1.1: Examples of couplings prescribed by an Abelian gauge symmetry ($U(1)$) and a non-Abelian one ($SU(2)$).

1.1.2 Spontaneously broken symmetries

If a theory is described by a Lagrangian invariant under a given symmetry but its physical vacuum is not, then the symmetry is said to be spontaneously broken.

There are in Nature several occurrences of spontaneous symmetry breaking. A ferromagnetic system is a canonical example. Above the Curie temperature the magnetic dipole moments show a rotational $SO(3)$ symmetry with all the dipoles randomly oriented in a three dimensional space (paramagnetic phase). The introduction of an external magnetic field explicitly breaks this $SO(3)$ symmetry down to $SO(2)$ by forcing the spins to be aligned along a privileged direction (parallel to the field itself). Turning the field off restores the original symmetry.
The system behaves differently when its temperature is below the Curie temperature. The lowest energy configuration corresponds to a parallel alignment of the magnetic dipoles: there is a non-zero magnetization along a preferred direction even in absence of external fields (i.e. of explicit terms in the Lagrangian breaking its symmetry). The $SO(3)$ symmetry is then spontaneously broken down to $SO(2)$ by the system's ground state, which "chooses" one particular configuration among infinite possibilities (the vacuum is infinitely degenerate). However, once a ground state configuration

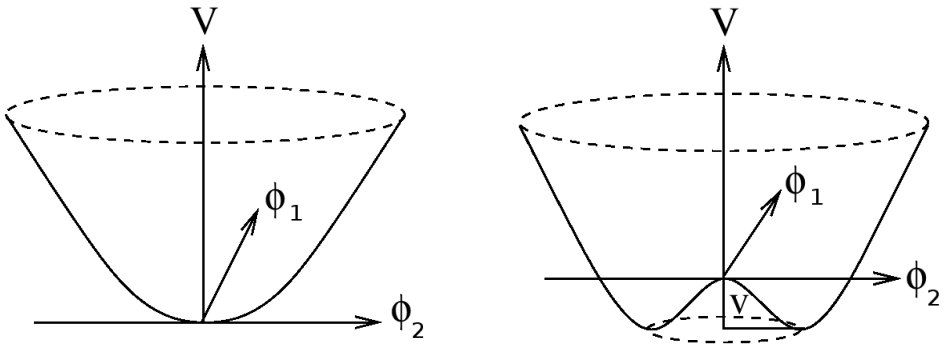

(a) (b)

Figure 1.2: Form for the potential $V(\phi^*\phi)$ of equation 1.19 depending on the sign of μ^2: negative (a) and positive (b).

has been chosen, it can not be changed unless an amount of energy is introduced into the system for each of the dipoles, in order to reorient them in a different direction.

The simplest example of spontaneous symmetry breaking in field theory is realized with discrete symmetries (namely parity). It shall be however discussed the slightly more advanced example of a complex scalar theory invariant under a global $U(1)$ symmetry.

The starting Lagrangian is of the form

$$\mathcal{L} = \partial_\mu \phi (\partial^\mu \phi)^* - V(\phi^* \phi), \tag{1.18}$$

where the effective potential $V(\phi\phi^*)$ is chosen as

$$V(\phi^*\phi) = -\mu^2 \phi^* \phi + \frac{\lambda}{2}(\phi^*\phi)^2, \qquad \lambda > 0. \tag{1.19}$$

Two cases, depending on the sign of μ^2, are considered (fig. 1.2).
If $\mu^2 < 0$, the symmetry is exact and there exists a unique vacuum state for the theory, at $\langle\phi\rangle = 0$.
On the other hand, if $\mu^2 > 0$ (which also means that μ can no longer be interpreted as a mass for the field ϕ) the vacuum state is infinitely degenerate for all the configurations satisfying

$$|\phi| = \left(\frac{\mu^2}{\lambda}\right)^{1/2} \equiv v. \tag{1.20}$$

Choosing one of them spontaneously breaks the $U(1)$ symmetry. The Lagrangian is still invariant under $U(1)$ so all the properties connected with

the original symmetry are preserved.
By explicitly choosing a vacuum configuration with only a real part

$$\langle\phi\rangle_0 = v, \tag{1.21}$$

it is possible to expand about this ground state by defining

$$\phi(x) = v + \frac{1}{\sqrt{2}}\left(\phi_1(x) + i\phi_2(x)\right), \tag{1.22}$$

with ϕ_1 and ϕ_2 real scalar fields.
The potential then becomes

$$V(\phi^*\phi) = -\frac{\mu^4}{2\lambda} + \frac{1}{2}\mu^2\phi_1^2 + \mathcal{O}(\phi_i^3) \tag{1.23}$$

and, omitting the constant terms, the Lagrangian can therefore be expressed as

$$\mathcal{L} = \frac{1}{2}(\partial_\mu\eta)(\partial^\mu\eta) + \frac{1}{2}(\partial_\mu\zeta)(\partial^\mu\zeta) + \mu^2\phi_1^2. \tag{1.24}$$

The field ϕ_1 has acquired a mass $m_1 = \sqrt{2}\mu$ while ϕ_2 is massless.
It is possible to get the flavour of this effect by looking at the form of the potential (fig. 1.2): the mass term for ϕ_1 is a consequence of the restoring force against radial oscillations, while the symmetry under $U(1)$ rotations that the Lagrangian still exhibits means that no restoring forces against angular oscillations exist, thereby allowing a massless ϕ_2 field.

The appearance of massless scalars when a global continuous symmetry is spontaneously broken is a consequence of a general theorem known as Goldstone's theorem. The number of new massless particles (so called Goldstone bosons) in the theory is related to the degrees of freedom of the symmetry group: a rotation in N dimensions is described by $N(N-1)/2$ parameters, each of them corresponding to a continuous symmetry. After a spontaneous breakdown of the $O(N)$ symmetry to an $O(N-1)$, there are still $(N-1)(N-2)/2$ unbroken symmetries. The number of massless Goldstone bosons corresponding to the broken symmetries is then $N(N-1)/2 - (N-1)(N-2)/2 = N-1$. It is trivial to verify that in the previous example this leads to exactly one Goldstone boson.

One can now asks what happens requiring $U(1)$ to be a local symmetry in the previous example. The derivation of the potential (1.19) is still valid, but plugging the ϕ expansion (1.22) into the Lagrangian gives rise to a

different result because of the different kinetic term due to the covariant derivative[1]. One in fact obtains that

$$(\mathcal{D}_\mu\phi)(\mathcal{D}^\mu\phi)^* = \frac{1}{2}(\partial_\mu\phi_1)^2 + \frac{1}{2}(\partial_\mu\phi_2)^2 + \sqrt{2}qv\cdot A_\mu\partial^\mu\phi_2 + q^2v^2A_\mu A^\mu + \mathcal{O}((A_\mu,\phi_1,\phi_2)^3). \tag{1.25}$$

The last term is simply a mass term for the gauge boson A_μ which is proportional to the vacuum expectation value v of the field ϕ ($m = \sqrt{2}qv$). This (miraculous!) interplay between local invariance and spontaneous symmetry breaking, first noticed by Higgs (Higgs, 1964), allows to reconcile the problems associated with the description of the weak interactions. The need of massive gauge bosons is satisfied by requiring the theory to fulfill (very elegant) local symmetry principles at the price of introducing new fields subjected to appropriate effective potentials (which is less elegant, indeed). In a certain way the massless gauge bosons "eat" the Goldstone scalars to get one more degree of freedom, the transversely polarized state proper of massless particles.

1.2 The $SU(2)_L \times U(1)_Y$ Model

The Standard Model of electroweak interactions unifies weak and electromagnetic interactions. It is a gauge theory with exact symmetries which are spontaneously broken. Proposed independently by Weinberg, Glashow and Salam ((Weinberg, 1967), (Glashow, 1961)), the Standard Model was formulated on the basis of the largest possible symmetry group associating the leptons ($SU(2) \times U(1)$) as inferred by experimental results at that time. It led to the unification of weak and electromagnetic interactions, respectively the $SU(2)$ and $U(1)$ sub-groups.

Summarized below are the main experimental facts explained by the theory, as outlined by (Renton, 1990):

- leptons and quarks are half-spin particles;
- when weak charged current interactions occur (mediated by $W^\pm$ exchange) leptons and quarks come in weak isospin doublets;
- charged current interactions appear to be purely left-handed ($V - A$ is a chiral theory) and to violate C and P maximally, while (almost) conserving CP;

[1] The covariant derivative is defined as $\mathcal{D}_\mu \equiv \partial_\mu + iqA_\mu$ (eq. 1.3).

- leptons and quarks come in three generations;
- charged lepton and quark masses substantially increase from one generation to the next, while neutrinos are very light particles;
- in addition to charged currents, there are two kinds of neutral currents: one coupling to all quarks and leptons (mediated by Z exchange) and the other coupling only to electromagnetic charged particles (mediated by γ exchange);
- short-range weak interactions are mediated by three massive particles ($W^{\pm}$, Z, with mass $m \sim \mathcal{O}(100\ \mathrm{GeV}/c^2)$) while infinite-range electromagnetic interactions are mediated by one massless boson (γ).

Not all of these facts were known when the first papers by Weinberg, Glashow and Salam were published. The presence of a weak neutral current, for example, was one of the most successful prediction of the theory.

1.2.1 The Gauge Sector

Imposing the local invariance of the theory under a $SU(2) \times U(1)$ transformation gives four (massless) gauge fields, three corresponding to the $SU(2)$ symmetry ($W^i\mu$, $i = 1, 2, 3$) and one to the $U(1)$ (B_μ). They appear in the definition of the covariant derivative

$$\mathcal{D}_\mu = \partial_\mu - igW_\mu^i \tau^i - ig' \frac{Y}{2} B_\mu, \tag{1.26}$$

where g and g' are the coupling constants of the $SU(2)$ and $U(1)$ groups respectively[2], $\tau^i \equiv \sigma^i/2$ are the generator of $SU(2)$ and Y is a quantum number usually called weak hypercharge.
Following the formalism outlined in the previous section, a scalar Higgs field ϕ is introduced into the theory in order to give a mass to the weak gauge fields. The $U(1)$ symmetry, which corresponds to the massless photon, must however not be broken.
The simplest choice for ϕ is a doublet representation of $SU(2)$:

$$\phi \equiv \begin{pmatrix} \phi^0 \\ \phi^+ \end{pmatrix}. \tag{1.27}$$

[2]Since $SU(2)$ and $U(1)$ commute, they can have different coupling constants

Giving to ϕ a charge 1/2 under $U(1)$, its complete $SU(2) \times U(1)$ transformation becomes

$$\phi \;\rightarrow\; e^{i\alpha^i \tau^i}\, e^{i\beta/2}\phi. \tag{1.28}$$

If ϕ acquires a vacuum expectation value of the form

$$\langle\phi\rangle = \frac{1}{\sqrt{2}} \begin{pmatrix} 0 \\ v \end{pmatrix}, \tag{1.29}$$

where α and β are real numbers. then $\langle\phi\rangle$ is not invariant under any of the original four generators. It is invariant, however, under the transformation corresponding to $\alpha^1 = \alpha^2 = 0$ and $\alpha^3 = \beta$, i.e. the linear combination $Q = (\tau^3 + Y/2)$ corresponding to the electric charge. Three massive bosons acquire therefore a mass via the Goldstone scalars associated with the three broken symmetries, but the photon remains massless.
By evaluating the kinetic term for $(\mathcal{D}^\mu\phi)^*\mathcal{D}_\mu\phi$, it is possible to figure out from the mass terms the $W^\pm$ bosons as the linear combination

$$W^\pm_\mu = \frac{1}{\sqrt{2}} \left(W^1_\mu \mp i W^2_\mu\right), \tag{1.30}$$

and the neutral vector boson Z and the electromagnetic vector potential A_μ as

$$\begin{aligned} Z_\mu &= \frac{1}{\sqrt{g^2 + g'^2}} \left(g W^3_\mu - g' B_\mu\right) \\ A_\mu &= \frac{1}{\sqrt{g^2 + g'^2}} \left(g' W^3_\mu + g B_\mu\right) \end{aligned} \quad . \tag{1.31}$$

The masses for the weak gauge bosons are

$$m_{W^\pm} = g\frac{v}{2} \qquad , \qquad m_Z = \sqrt{g^2 + g'^2}\,\frac{v}{2} \tag{1.32}$$

By defining the Weinberg angle as the mixing angle between (W^3, B) that gives (Z, A), the following relations are obtained:

$$\begin{pmatrix} Z \\ A \end{pmatrix}_\mu = \begin{pmatrix} \cos\vartheta_W & -\sin\vartheta_W \\ \sin\vartheta_W & \cos\vartheta_W \end{pmatrix} \begin{pmatrix} W^3 \\ B \end{pmatrix}_\mu, \tag{1.33}$$

with

$$\cos\vartheta_W = \frac{g}{\sqrt{g^2 + g'^2}} \qquad , \qquad \sin\vartheta_W = \frac{g'}{\sqrt{g^2 + g'^2}} \tag{1.34}$$

Rewriting $\mathcal{D}_\mu$ as a function of the gauge bosons mass eigenstates would allow us to identify the electromagnetic current term. This would in turn

lead to the important relation between the electric charge e and the coupling constants g, g':

$$e = g \sin \vartheta_W . \tag{1.35}$$

Moreover the masses of Z and W are not independent:

$$m_W = m_Z \cos \vartheta_W . \tag{1.36}$$

Three free parameters of the gauge sector hence exist: the two coupling constants g and g' and the vacuum expectation value v of the Higgs field. These parameters are usually expressed using the electromagnetic coupling constant $\alpha_{\text{e.m.}}$, the Fermi constant G_F and the mass of the Z boson, which are measured with a very high accuracy (Eidelman *et al.*, 2004). The coupling constant

$$\alpha_{\text{e.m.}} = \frac{gg'}{4\pi\sqrt{g^2 + g'^2}} = \frac{1}{137.03599911(46)} \tag{1.37}$$

is determined from the anomalous magnetic moment of electrons and positrons,

$$\frac{G_F}{(\hbar c)^3} = \frac{1}{\sqrt{2}\, v^2} = 1.16637(1) \times 10^{-5}\ \text{GeV}^{-2} \tag{1.38}$$

from the muon decay, and

$$m_Z = \frac{v}{2}\sqrt{g^2 + g'^2} = (91.1876 \pm 0.0021)\ \text{GeV}/c^2 \tag{1.39}$$

from the Z-lineshape scan at LEP1.

1.2.2 Fermions

If just one family of quarks and leptons is considered (e.g. (e, ν_e), (u, d))[3]in the description of the electroweak processes, the representations of $SU(2)_L \times U(1)_Y$ assigned to the fermions must preserve the chiral nature of the weak charged current interactions and the coupling of electromagnetism to left- and right-handed fermions. These requirements lead to

[3]The generalization to the other two families of fermions (μ, ν_μ), (τ, ν_τ), (c, s), (b, t) is straightforward.

$$
\begin{aligned}
L_{_L} &= \begin{pmatrix} \nu_{e_{_L}} \\ e_{_L} \end{pmatrix} = \mathcal{P}_{_L} \begin{pmatrix} \nu_e \\ e \end{pmatrix} && \rightsquigarrow \quad (2,-1) \\
e_{_R} &= \mathcal{P}_{_R}\ e && \rightsquigarrow \quad (1,-2) \\
Q_{_L} &= \begin{pmatrix} u_{_L} \\ d'_{_L} \end{pmatrix} = \mathcal{P}_{_L} \begin{pmatrix} u \\ d' \end{pmatrix} && \rightsquigarrow \quad \left(2,\tfrac{1}{3}\right) \\
u_{_R} &= \mathcal{P}_{_R}\ u && \rightsquigarrow \quad (1,\tfrac{4}{3}) \\
d'_{_R} &= \mathcal{P}_{_R}\ d' && \rightsquigarrow \quad (1,-\tfrac{2}{3})
\end{aligned}
\tag{1.40}
$$

where $\mathcal{P}_{_L} = \frac{1-\gamma_5}{2}$ and $\mathcal{P}_{_R} = \frac{1+\gamma_5}{2}$ are the projection operators on orthogonal elicity states, and the last column represents the quantum numbers corresponding to the representations of $SU(2)_L \times U(1)_Y$.
From the Gell-Mann–Nishijima relation $Q = \tau_3 + Y/2$ it can be noticed that an eventual right-handed neutrino $\nu_{_R}$, singlet of the gauge group, would have vanishing both charge and weak hypercharge. This neutrino would therefore not interact electroweakly and only indirect measurements could proof its existence.
In the expression given above, down quarks come with a " $'$ ": quark mass eigenstates, in fact, do not coincide with weak interaction eigenstates. The latter are a linear combination of the mass eigenstates through the unitary mixing matrix

$$
\begin{pmatrix} d' \\ s' \\ b' \end{pmatrix} = \begin{pmatrix} V_{ud} & V_{us} & V_{ub} \\ V_{cd} & V_{cs} & V_{cb} \\ V_{td} & V_{ts} & V_{tb} \end{pmatrix} \begin{pmatrix} d \\ s \\ b \end{pmatrix}, \tag{1.41}
$$

which is generally referred to as the Cabibbo-Kobayashi-Maskawa matrix.

It is has been shown experimentally that fermions are massive particles[4]. However, a mass term of the generic form

$$
-m\overline{\psi}\psi = -m(\overline{\psi}_{_L}\psi_{_R} + \overline{\psi}_{_R}\psi_{_L}) \tag{1.42}
$$

would break the gauge invariance in the Lagrangian ($\psi_{_L}$ and $\psi_{_R}$ belong to different representation of $SU(2)$ and have different $U(1)$ charges) and is therefore not allowed. Notwithstanding this unpleasant feature of chiral Lagrangians, it is possible to build a mass term with the help of the Higgs field. The mass term for the leptons is

$$
\mathcal{L}_{\text{Yukawa}} = \sum_{i=e,\mu,\tau} \left(-\lambda_i \overline{L}^i_{_L} \cdot \phi e^i_{_R} + \text{h.c.} \right), \tag{1.43}
$$

[4]Recent results from neutrino oscillation experiments seem to indicate non-zero masses also for neutrinos.

where λ_i are new dimensionless parameters of the theory. Replacing the field ϕ by its expectation value yields

$$\mathcal{L}_{\text{Yukawa}} = \sum_{i=e,\mu,\tau} \left(-\lambda_i \frac{v}{\sqrt{2}} \overline{e}^{\,i}_{L} e^{i}_{R} + \text{h.c.} \right). \tag{1.44}$$

It follows that the mass for the lepton i is proportional to its Yukawa coupling to the Higgs:

$$m_i = \frac{1}{\sqrt{2}} \lambda_i v. \tag{1.45}$$

Proceeding in the same way for the quark mass terms, one obtains

$$\mathcal{L}_{\text{Yukawa}} = \sum_{i=d,s,b} \left(-\lambda_i \frac{v}{\sqrt{2}} \overline{d}^{\,i}_{L} d^{i}_{R} + \text{h.c.} \right) + \sum_{i=u,c,t} \left(-\lambda_i \frac{v}{\sqrt{2}} \overline{u}^{\,i}_{L} u^{i}_{R} + \text{h.c.} \right), \tag{1.46}$$

and for the mass of the quark i

$$m_i = \frac{1}{\sqrt{2}} \lambda_i v. \tag{1.47}$$

An additional complication for quarks, which is not made explicit here, is that the Yukawa couplings involve mass eigenstates. To have the corresponding expression in terms of the weak eigenstates base, the Cabibbo-Kobayashi-Maskawa matrix elements (1.41) must be properly introduced, in order to pass from the mass eigenstates to the weak interaction ones.

1.2.3 Anomaly Cancellation

Even if a theory is renormalizable (and non-Abelian gauge theories are, as demonstrated by 't Hooft ('t Hooft, 1976)) there can be currents whose conservation (through gauge invariance + Noether's theorem) holds at tree level but is violated in first loop diagrams. An examples of such a current is given in figure 1.3: all the divergences coming from these loops must cancel out to give a finite theory at all perturbative orders.
It can be shown that

$$A^{abc} \propto \text{tr} \left[\gamma_5 \tau^a \left\{ \tau^b, \tau^c \right\} \right] = A^{abc}_{+} - A^{abc}_{-}, \tag{1.48}$$

where the trace is taken over all the fermion families and in the last equivalence the factor γ_5 has been explicitly set equal to ∓ 1 for left- and right-handed fermions respectively.

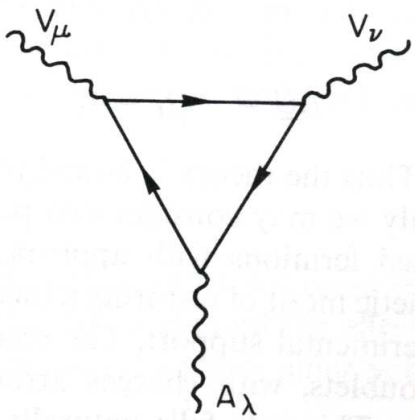

Figure 1.3: Example of a triangle anomaly. In this case the axial-vector current is represented.

For a theory which equally couples left- and right-handed fermions, the cancellation comes automatically, since $A_+^{abc} = A_-^{abc}$. Indeed, the Standard Model is a chiral theory, and this automatic cancellation does not take place. It can be shown, however, that the only anomaly in the theory is proportional to

$$\mathrm{tr}\left[\{\tau^a, \tau^b\}Y\right] = \frac{1}{2}\delta^{ab}\sum_{\substack{\text{fermion}\\ \text{doublets}}} Y. \tag{1.49}$$

Using the Gell-Mann–Nishijima relation, the condition for the absence of anomalies can be expressed as a function of electric charge:

$$\Delta Q = Q_R - Q_L = \sum_{\substack{\text{right-handed}\\ \text{doublets}}} Q \quad - \sum_{\substack{\text{left-handed}\\ \text{doublets}}} Q \tag{1.50}$$

Considering a single fermion generation in the Standard Model, one left-handed lepton doublet corresponds to one left-handed quark doublet, while right-handed doublets are absent. This translates in

$$\Delta Q = -Q_L = 1 + \frac{2}{3} - \frac{1}{3} = \frac{1}{3}, \tag{1.51}$$

which means anomalies have been introduced into the theory. By supposing, however that quarks come with an additional three-flavoured charge with respect to the leptons, as suggested by the strong interaction theory, a factor 3, which corresponds to the three different possible "strong charges" the doublet may have, has to be taken into account. The expression for ΔQ

then becomes

$$\Delta Q = -Q_{_L} = 1 + 3 \cdot \left(\frac{2}{3} - \frac{1}{3}\right) = 0, \tag{1.52}$$

so the anomalies cancel (within each single fermion generation).
Given the Standard Model of electroweak interaction, an indication for a description of strong interactions has been found as a condition for its renormalizability.

1.2.4 The Higgs Boson

It has been shown in the previous sections how the Higgs field give mass to gauge bosons and fermions, but this is not the only consequence of the introduction of a scalar field into the theory. As demonstrated in section 1.1.2 a new massive scalar particle is expected to appear.
To see how this can happen within the Standard Model, one can parametrize the expansion of the Higgs field ϕ about its ground state in the following way (so called unitary gauge):

$$\phi(x) = \frac{1}{\sqrt{2}} U(x) \begin{pmatrix} 0 \\ v + H(x) \end{pmatrix}, \tag{1.53}$$

where $U(x)$ is a general transformation of $SU(2)$ to produce the most general double-component spinor ϕ and $H(x)$ is a real field such that $\langle h(x) \rangle = 0$. $U(x)$ can always be eliminated from the Lagrangian by a gauge transformation so it will not be considered in the following discussion.
One seeks to write explicitly in term of the expansion 1.53 all the pieces of the Standard Model Lagrangian containing the Higgs field ϕ. The effective Lagrangian for ϕ and the Yukawa couplings to the fermions.
The usual form of the Lagrangian for ϕ is

$$\begin{aligned} \mathcal{L}_H &= (\mathcal{D}_\mu \phi)^\dagger (\mathcal{D}_\mu \phi) - V(\phi^\dagger \phi) = \\ &= (\mathcal{D}_\mu \phi)^\dagger (\mathcal{D}_\mu \phi) + \mu^2 \phi^\dagger \phi - \lambda (\phi^\dagger \phi)^2, \end{aligned} \tag{1.54}$$

where the potential reaches a minimum at

$$v \equiv \left(\frac{\mu^2}{\lambda}\right)^{1/2}. \tag{1.55}$$

Plugging ϕ in the potential yields

$$\begin{aligned} \mathcal{L}_V &= -\mu^2 H^2 - \lambda v H^3 - \frac{1}{4} \lambda H^4 = \\ &= -\frac{1}{2} m_H^2 H^2 - \sqrt{\frac{\lambda}{2}} m_H H^3 - \frac{1}{4} \lambda H^4, \end{aligned} \tag{1.56}$$

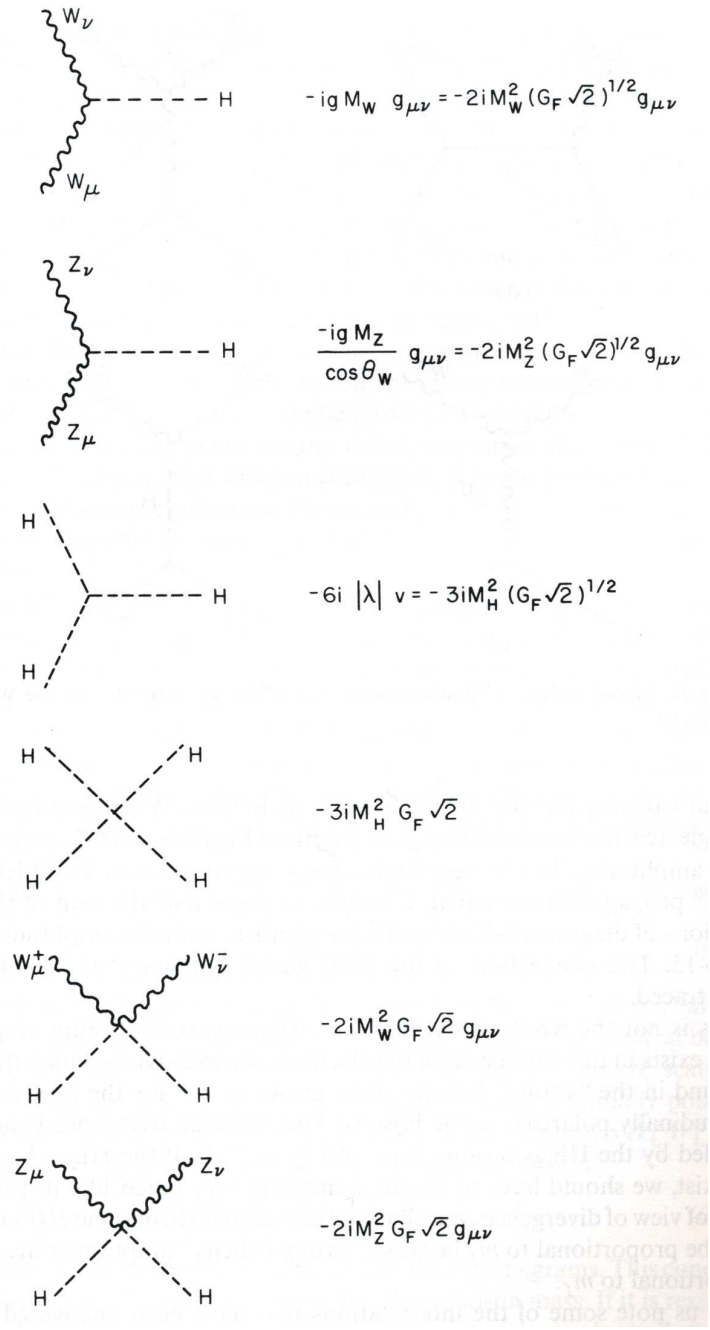

Figure 1.4: Feynman diagrams and rules for the interaction of the Higgs boson and gauge bosons.

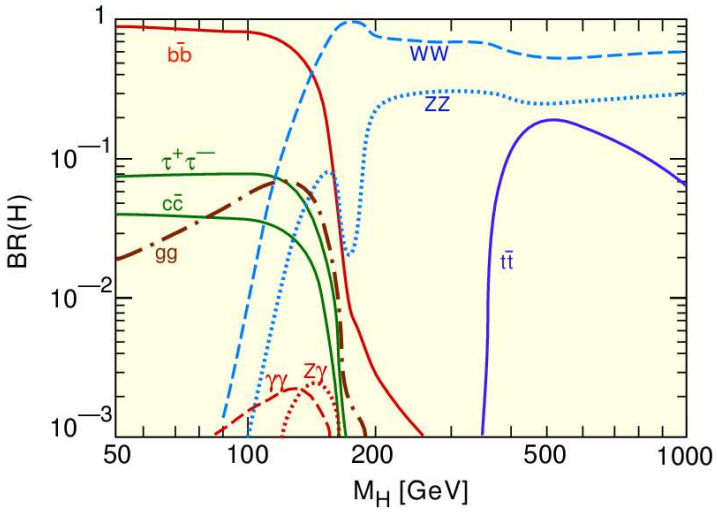

(a)

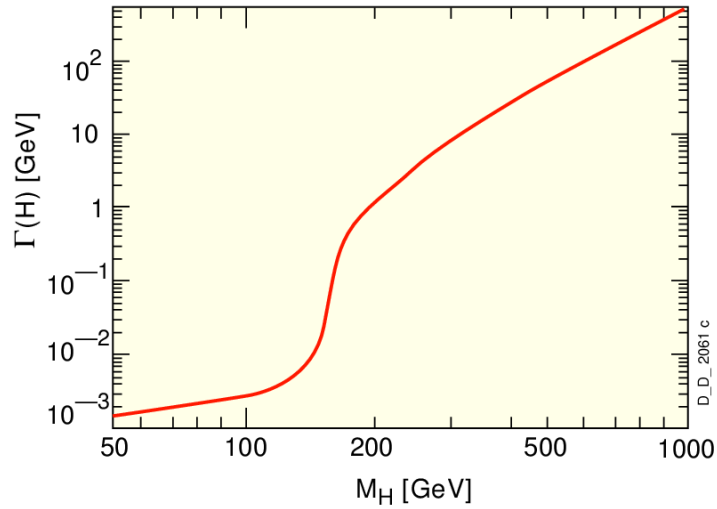

(b)

Figure 1.5: (a) Branching ratio for H decay for a variety of channels as a function of the Higgs boson mass. (b) Total decay width of the Higgs boson as a function of the Higgs boson mass.

The field H is therefore a massive scalar, with a mass given by

$$m_H = \sqrt{2\lambda}\, v, \tag{1.57}$$

and is called Higgs boson.
The kinetic term in $\mathcal{L}_H$ written in terms of ϕ gives

$$\mathcal{L}_K = \frac{1}{2}(\partial_\mu H)^2 + \left(m_W^2\, W_\mu^+ W^{\mu-} + \frac{1}{2} m_Z^2\, Z_\mu Z^\mu \right) \cdot \left(1 + \frac{H}{v} \right)^2 . \tag{1.58}$$

Finally, the Yukawa Lagrangian produces for each fermion f a term of the form

$$\mathcal{L}_f = -m_f\, \overline{f} f \left(1 + \frac{H}{v} \right) \tag{1.59}$$

An illustration of the Higgs boson couplings to the gauge bosons and to the fermions (and the cubic and quartic self-interaction couplings) is given in figure 1.4. As the associated Feynman rules show, the couplings are completely determined by the masses of the particles involved and by the weak interaction coupling constants. In particular, couplings to $W^\pm$ and Z are proportional to mass of the gauge bosons squared, while for fermions couplings are directly proportional to the fermions' mass. The coupling to the gluons and to the photons via fermionic loop is also interesting. Indeed, due to its mass, the t quark gives the dominant contribution. The first coupling relation is particularly important for the Higgs boson production processes at hadron colliders. On the other hand, the second coupling relations provide one of the cleanest signatures for experimental detection.
A detailed view of the branching ratios for the different decays of the Higgs boson is given in figure 1.5(a) as a function of m_H. As a consequence of the linear Higgs coupling to the fermion masses, for $m_H < 2m_W$ the dominant channel is $H \to b\overline{b}$, which corresponds to the decay in the heaviest fermion kinematically accessible. Beyond the threshold for the production of two gauge boson $H \to WW^{(*)}$ and $H \to ZZ^{(*)}$ become dominant because of a factor $m_H^3/m_{W^\pm,Z}^2$ in the partial width. The total decay width of the Higgs boson as a function of the Higgs mass is given in figure 1.5(b): the asymptotic behaviour is proportional to m_H^3.

Existing Constraints on m_H

Although the Higgs mass is a free parameter of the Standard Model, there are theoretical arguments of internal consistency of the theory giving indications and limits on it. On the experimental side, direct and indirect searches

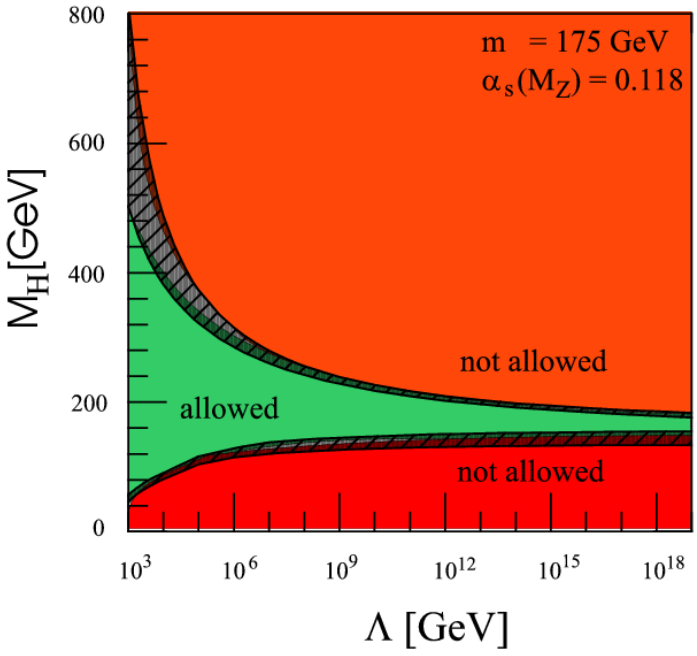

Figure 1.6: Theoretical limits on the Higgs boson mass assuming the validity of the Standard Model up to a scale Λ.

have been carried out.

By assuming the Standard Model to be valid at least up to a certain energy scale Λ, a lower bound for m_H comes from the requirement for the symmetry breaking to actually occur. This transposes into the condition for the potential $V(\langle\phi\rangle) < V(0)$, that is equivalent to $\lambda > 0$ at all scales. On the other hand, since perturbative corrections to the Higgs self interaction terms make λ increasing with energy, requiring λ to keep finite up to the scale Λ translates in an upper bound for m_H . These two theoretical limits are shown in figure 1.6. From what concerns the experimental constraints, results of direct searches at LEPII are shown in figure 1.7: values for m_H up to 114.4 GeV/c^2 are excluded. Indirect constraints based on the requirement that all the measurements of electroweak observables (e.g. asymmetry measurements, mass for $W^{\pm}$, top quark mass etc.) be consistent allow to exclude a Higgs mass greater than 237 GeV/c^2 at 95% C.L.. The best fit for all these measurements gives the value $m_H = 114^{+69}_{-45}$ GeV/c^2 at 95% C.L. (figure 1.7) assuming $m_{\text{top}} = 178 \pm 4$ GeV/c^2.

However, indirect constraints on Higgs boson mass have a limited sensitivity, since second order corrections to Standard Model observables depend

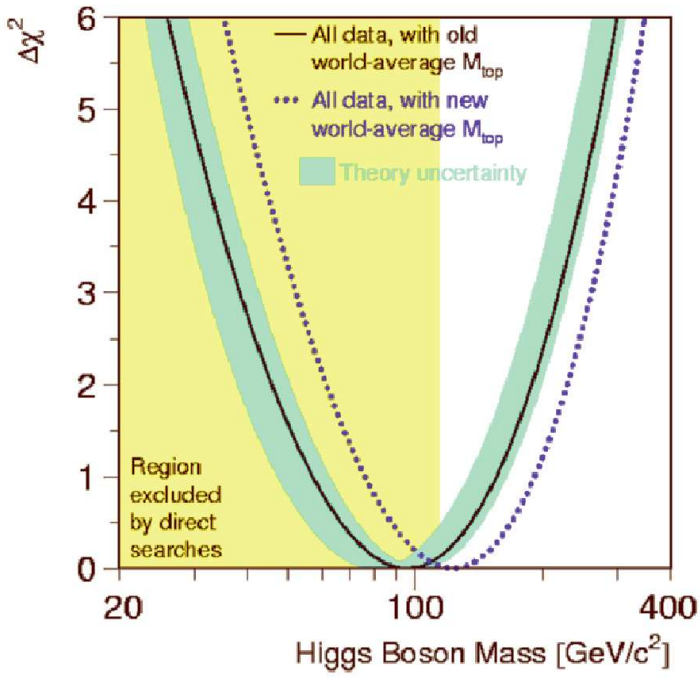

Figure 1.7: Experimental limits on the Higgs boson mass coming from direct searches at LEP (the excluded region is shadowed) and $\Delta\chi^2$ result of a fit on electroweak observables assuming m_H the only free parameter.

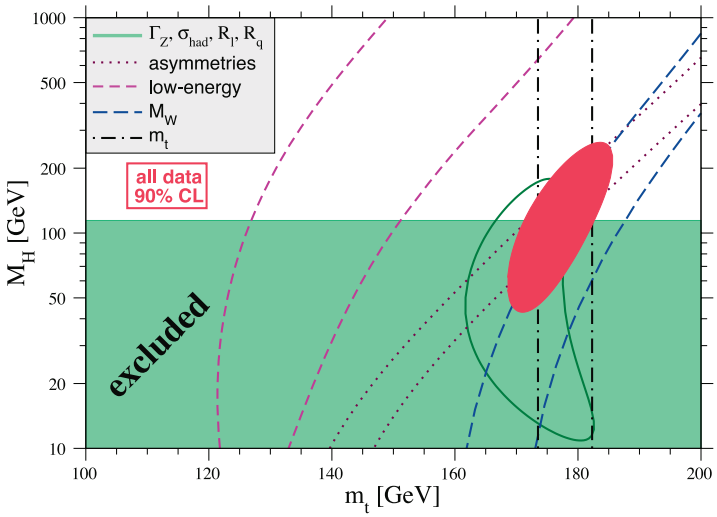

Figure 1.8: One-standard-deviation (39.35%) uncertainties in m_H as a function of m_t for various inputs, and the 90% CL region ($\Delta\chi^2 = 4.605$) allowed by all data. $\alpha_s(m_Z) = 0.120$ is assumed except for the fits including the Z-lineshape data. The 95% direct lower limit from LEP 2 is also shown.

only logarithmically on m_H, while fermions give contributions quadratically dependent on m_f. It turns out that, because of the large mass for the top quark (comparable to the predicted Higgs mass), uncertainty on the top mass can sensibly shift the constraints on m_H, as illustrated in figure 1.8, in which the dependence of electroweak observables on m_H and m_t is made explicit.

1.2.5 Standard Model Higgs Production in $p-p$ collisions

The description of the interaction of two protons is based, within the QCD framework, on the parton model approximation. This consists in considering the incoming beam of hadrons equivalent to a beam of constituents (called partons and identified with quarks and gluons) whose momentum distributions inside the hadron is characterized by parton density functions (pdf) $f_i(x, \mu)$. The probability to find the parton i carrying a fraction between x and $x + dx$ of the initial momentum p of the hadron is given by $dx\ f_i(x, \mu)$, where μ is the typical energy scale of the process. The pdf's do not depend on the particular process considered are and are therefore universal functions. They exhibit a moderate and computable dependence

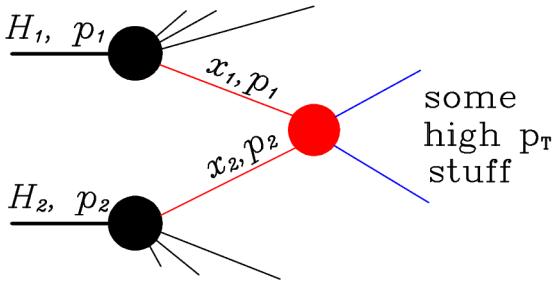

Figure 1.9: Representation of the improved parton model formula (eq. 1.60).

upon the energy scale of the interaction.

The general expression for the production cross section of some final state with high invariant mass from the interaction of two protons beams with momenta p_1 and p_2 (figure 1.9) can then be expressed by the so called improved parton model formula:

$$\sigma(p_1, p_2) = \sum_{i,j} \int dx_1 dx_2 \; f_i(x_1, \mu) f_j(x_2, \mu) \sigma_{ij}(x_1 p_1, x_2 p_2, \alpha_s(\mu), \mu). \quad (1.60)$$

The cross-section for the most important processes at LHC is shown in figure 1.10.

In p-p collisions, the dominant Higgs production mechanism over the entire mass range accessible at LHC (see chapter 2) is via gluon fusion ($gg \rightarrow H$), where the Higgs couples to the gluons through a heavy quark loop (figure 1.11).

The leading contribution to the loop comes from the top quark. The other quarks contribute to the loop by a factor at least smaller by $\mathcal{O}(M_b^2/M_t^2)$ because of the form of the Higgs boson coupling to the fermions.

As summarized in (Del Duca, 2003) QCD corrections at the Next to Leading Order (NLO) have been computed and show an increase of the LO cross section by 10-80%, thereby leading to a significant change of the theoretical predictions. NNLO calculations have recently become available in the heavy top quark limit, thereby replacing the coupling of the Higgs to

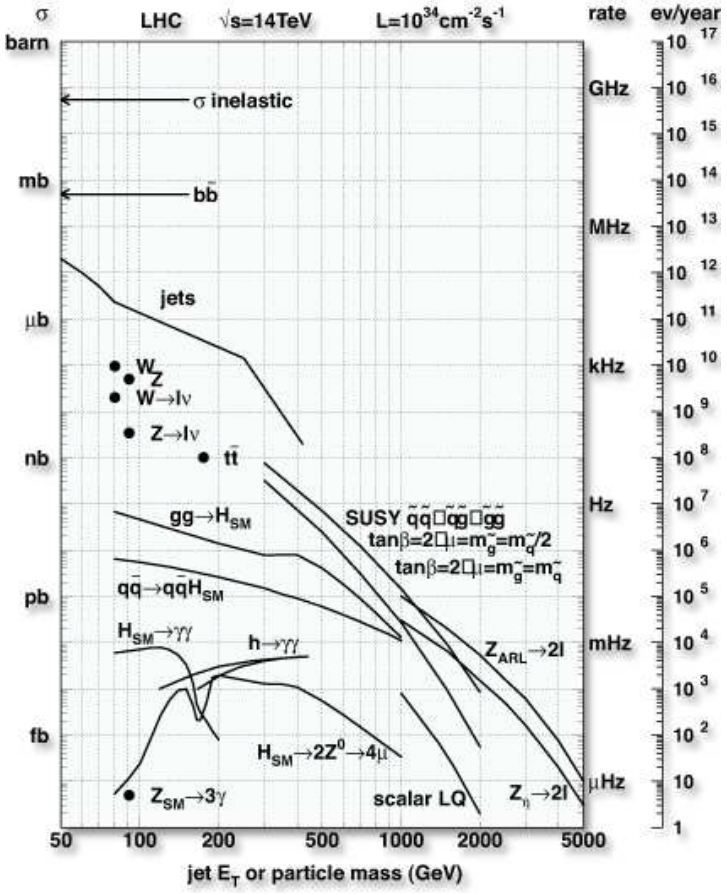

Figure 1.10: Cross-section for the most important process at LHC as a function of the center of mass energy. The rate of events per year is also reported on the right scale, assuming for LHC an integrated luminosity of 100 fb^{-1} (High Luminosity phase).

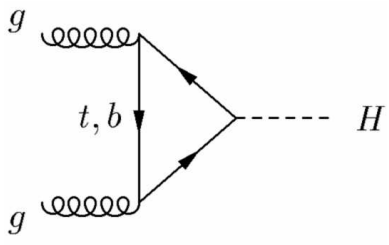

Figure 1.11: Gluon fusion process for the Higgs boson production in hadronic collisions.

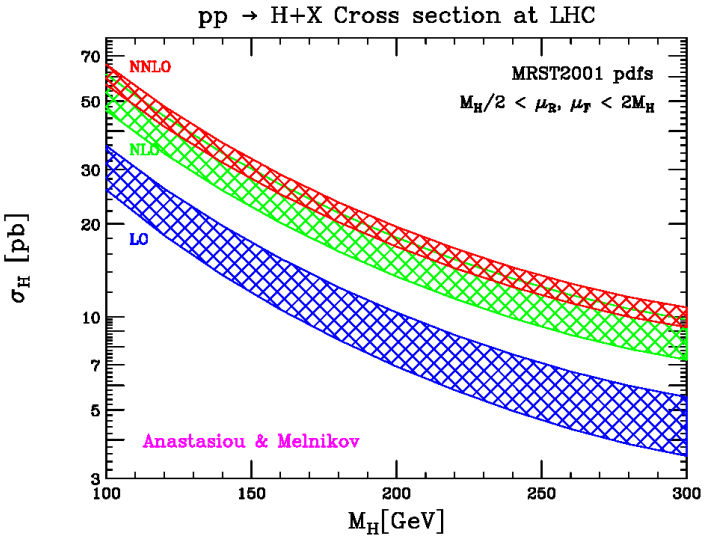

Figure 1.12: Higgs production via gluon fusion in pp collisions at a center of mass energy of 14 TeV/c^2 as a function of the Higgs mass. The production rate has been computed in the large m_{top} limit, to leading order, NLO and NNLO accuracy. The shaded bands display the renormalisation μ_R and factorisation μ_F scale variations. The lower contours correspond to $\mu_R = 2m_H$ and $\mu_F = m_H/2$, while the upper contours to $\mu_R = m_H/2$ and $\mu_F = 2m_H$.

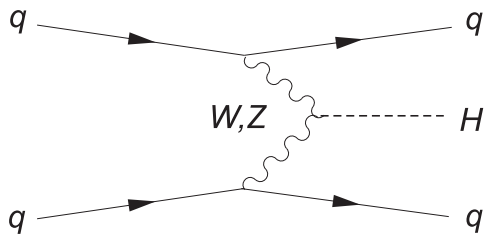

Figure 1.13: Weak boson fusion (WBF) process for the Higgs production in hadronic collisions.

the gluons by an effective coupling (valid if the Higgs mass is smaller than the threshold for the creation of a top quark pair). It is expected to approximate the full massive rescaling factor within 10% up to 1 TeV/c^2, covering the entire Higgs mass range accessible at LHC. NNLO corrections display an increase of about 15% at $m_H = 120$ GeV/c^2 with respect to the NLO evaluation. Figure 1.12 shows the effect of the higher order corrections to the Higgs total cross section via gluon fusion.

The second largest production mechanism for the Higgs boson is via weak boson fusion (WBF, $qq \to qqH$), where the Higgs is radiated off the weak boson exchanged in the t-channel between the two incoming quarks (figure 1.13). Since the distribution functions of the incoming valence quarks peak at values of the momentum fractions $x \approx 0.1$-0.2, the two outgoing quarks are naturally highly energetic. They therefore hadronize into two jets with a large rapidity interval between them, typically at forward-backward rapidities. Another interesting property is the absence of hadronic production in the rapidity interval between the two jets, since the colourless weak interaction boson exchanged between the incoming quarks causes gluon radiation to occurs only as bremsstrahlung off the quark legs. This features can be used to distinguish WBF Higgs production from gluon gluon fusion. NLO corrections in α_s to the WBF production process have been computed and found to be modest (on the order of 5-10%) (Puljak, 2000).

The cross-sections for the two production processes illustrated above along with minor processes such as Higgsstrahlung or $t\bar{t}$ associated production are shown in figure 1.14.

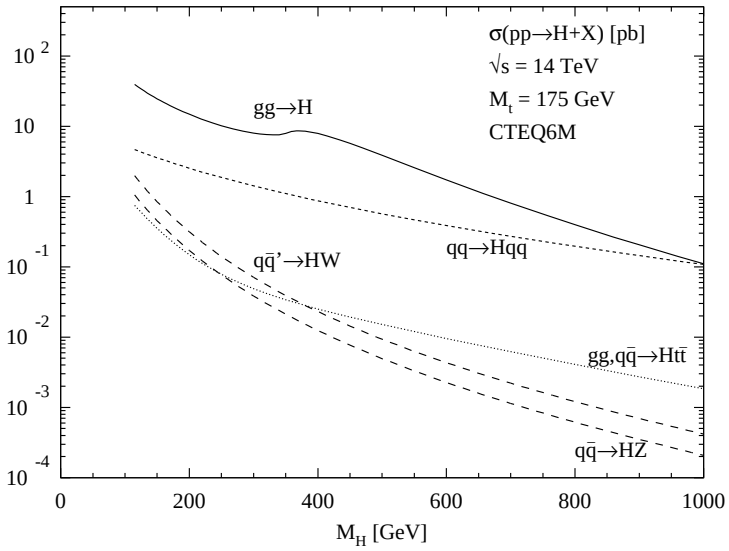

Figure 1.14: Cross-section for the Standard Model Higgs production at LHC.

1.3 Going Beyond

Despite the incredibly good agreement between Standard Model predictions and experiments (for an example of some observables see the figure 1.15), there are both conceptual problems and phenomenological indications of new physics beyond it.

Particle mass and quantum numbers such as the electric charge, weak isospin, hypercharge and colours are not explained by the Standard Model. Furthermore, there is no reason why leptons and quarks come in different flavours and why their electroweak interaction mix in such a peculiar way. Is this an indication towards more elementary constituents of matter than quarks and leptons?

After the extension of the Standard Model, based on experiments, to the group $SU(3) \times SU(2) \times U(1)$ in order to include the strong interactions ($SU(3)$ group), one is also tempted to include gravity in the same way. However, typical energy scales for quantum gravity are of the order of $M_P \sim 1/\sqrt{G_N} \sim 10^{19}$ GeV/c^2, seventeen orders of magnitude higher than the typical electroweak interactions. Can the Standard Model without new physics be valid up to such large energies? This appears unlikely, since there are no indications in the Standard Model of why the typical weak scale of masses is so small relatively to the Planck mass M_P (hierarchy problem).

The Higgs sector of the Standard Model, which reflects the most accepted

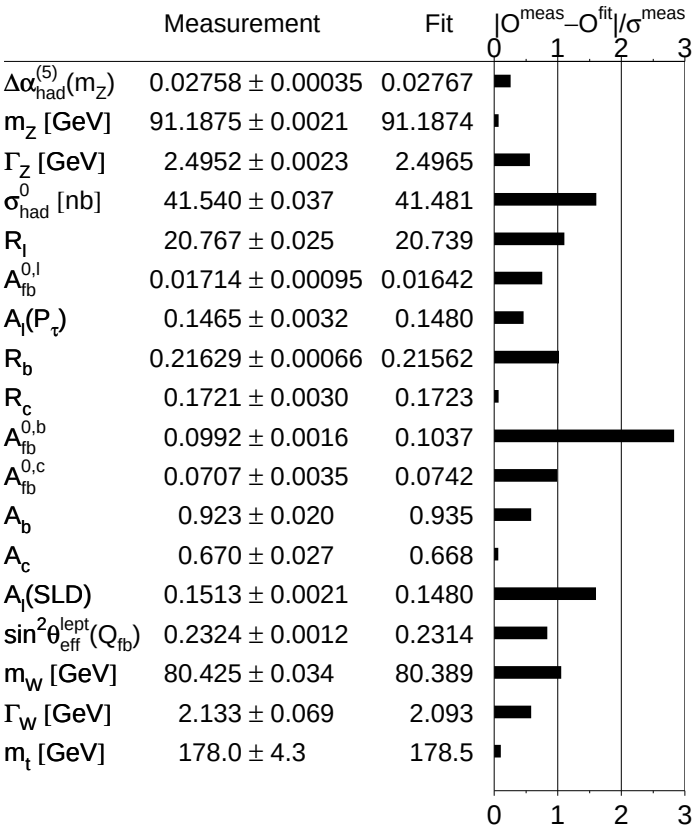

Figure 1.15: Comparison of the measurements with the expectation of the SM calculated for the five SM input parameter values in the minimum of the global χ^2 of the fit (The ALEPH, DELPHI, L3, OPAL, SLD Collaborations, the LEP Electroweak Working Group, the SLD Electroweak and Heavy Flavour Groups, 2005). The pull of each measurement is reported as well. The directed measurements of m_W and Γ_W used here are still preliminary.

mechanism for the electroweak symmetry breaking, is not satisfactory as well. Loop corrections to the Higgs mass are quadratically divergent, giving rise to the so-called naturality problem.

If the Standard Model is not the fundamental theory, it will be valid up to a certain energy scale Λ. This limit can be viewed as a cut off which parametrizes our ignorance on the new physics that will modify the theory at large energy scales. It is then interesting to look at the relevant quantities of the Standard Model upon the cut off scale Λ, requiring that no "unnatural" dependence on Λ arise. For what concerns the Higgs mass, in order not to exceed the limits indicated by direct and indirect searches Λ must be small, of the order of $\mathcal{O}(1\ \mathrm{TeV}/c^2)$, but cannot be too small since new physics has not been detected at the present experiments.

Moreover, another unsatisfactory theoretical aspect of the Standard Model is the number of arbitrary parameters. These include three independent gauge couplings, a possible CP-violating strong-interaction parameter, two independent masses for weak bosons, six quark and three charged-leptons masses, three generalized Cabibbo weak-mixing angles and the CP-violating Kobayashi-Maskawa phase.

On the other hand, from the experimental side there is a strong evidence of neutrino oscillations, implying massive neutrinos and the violation of the family lepton number (and at least nine more arbitrary parameters in the Standard Model to accommodate these effects). Direct measurements of neutrino masses, mainly from β-decay experiments, have imposed upper limits from $\mathcal{O}(1\ \mathrm{eV}/c^2)$ for the electron neutrino to $\mathcal{O}(10^2\ \mathrm{eV}/c^2)$ for the tau neutrino, which are roughly ten order of magnitudes less than the heaviest fermion mass ($m_t \sim \mathcal{O}(10^2\ \mathrm{GeV}/c^2)$). Although there are no symmetries in the theory protecting neutrinos from having a mass (e.g. a massless photon is imposed by the $U(1)$ gauge symmetry, related to the electric charge conservation), the mechanism to give such a mass is not trivial. If a Yukawa coupling via Higgs boson is invoked, a right-handed neutrino must be introduced into the Standard Model, unless the unconfirmed hypothesis that neutrinos are Majorana particles is true. A right-handed neutrino in the Standard Model, however, should be neutral both to electromagnetic and weak charge, from the constraints imposed by LEP on the number of neutrino families ((LEP Electroweak Working Group, 1999)). Thus it will be a singlet of $SU(2) \times U(1)$, with the right of an additional Dirac mass term in the Lagrangian that will be totally unconstrained. So more complicated mechanism for the generation of the neutrino masses within the Standard

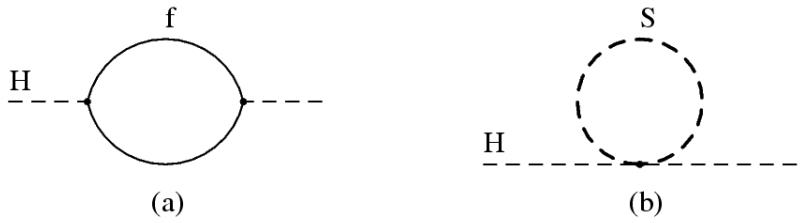

Figure 1.16: One-loop corrections to the Higgs boson mass due to fermionic (a) or bosonic (b) degrees of freedom.

Model should be introduced. The so called "see-saw" mechanism is the most popular alternative, which combines left- and right-handed neutrinos in Dirac and Majorana mass terms, in order to justify such small masses for the neutrinos.
Two are the possible extensions of the Standard Model that will be briefly considered in the following: supersymmetry and extra-dimensions.

1.3.1 Supersymmetry

Mainly motivated to stabilize the Higgs mass quadratic divergences, supersymmetry consists in assuming the existence of a symmetry Q that transforming fermions to bosons and vice versa. For each fermion in the theory is then introduced a new boson and, by analogy, to each bosons is associated a fermion. This has an immediate consequence on the one-loop corrections to the Higgs mass (figure 1.16). In fact, term due to fermionic degrees of freedom enters with an opposite sign with respect to corrections due to bosonic degrees of freedom. If λ_f and λ_s are the Higgs couplings to fermions and bosons respectively, the one-loop correction Δm_H^2 to the Higgs mass becomes proportional to

$$\Delta m_H^2 \propto (\lambda_s - \lambda_f)\Lambda^2 + \mathcal{O}(\Lambda^4). \tag{1.61}$$

For suitable values of the coupling constants the quadratic divergences disappear, leaving only logarithmic divergences.
In a supersymmetric Standard Model each fermion is then coupled to a boson in a supersymmetric multiplet, called "supermultiplet": to each lepton is associated a so called "slepton", a "squark" to each quark. In the same way, each gauge boson has a supersymmetric partner ("gaugino") to form a

spin 0	spin 1/2	spin 1	$SU(3)_C$	$SU(2)_L$	$U(1)_Y$
$\tilde{u}_L, \tilde{d}_L$	u_L, d_L		**3**	**2**	$+\frac{1}{3}$
$\tilde{u}_R$	u_R		**3**	**1**	$+\frac{4}{3}$
$\tilde{d}_R$	d_R		**3**	**1**	$-\frac{2}{3}$
$\tilde{\nu}, \tilde{e}_L$	ν, e_L		**1**	**2**	-1
$\tilde{e}_R$	e_R		**1**	**1**	-2
H_u^+, H_u^0	$\tilde{h}_u^+, \tilde{h}_u^0$		**1**	**2**	$+1$
H_d^0, H_d^-	$\tilde{h}_d^0, \tilde{h}_d^-$		**1**	**2**	-1
	$\tilde{g}$	g	**8**	**1**	0
	$\tilde{w}^\pm, \tilde{w}^0$	$W^\pm, W^0$	**1**	**3**	0
	$\tilde{b}^0$	B^0	**1**	**1**	0

Table 1.1: Particle content of a supersymmetric Standard Model.

gauge supermultiplet.

In the simplest extension of the Standard Model (called Minimal Supersymmetric Standard Model) the Higgs sector is composed by two scalar doublets, with their fermionic partners. In table 1.1 the list of the Standard Model particles and their supersymmetric partners ("superpartners") with the quantum numbers of each supermultiplet is given as a reference.
In order to implement the baryon (B) and lepton (L) number conservation, a new conserved quantum number called R-parity is defined as

$$P_R = (-)^{3(B-L)+2S}, \tag{1.62}$$

where $B = 1/3$ for quarks and squarks and 0 otherwise, $L = 1$ for leptons and sleptons, 0 otherwise, and S is the particle spin. P_R is equal to $+1$ for standard particles while it takes the value -1 for superpartners.
Some consequences of the R-parity conservation are:

- the lightest supersymmetric particle (LSP) with $P_R = -1$ is stable;
- supersymmetric particles decay into states with an odd number of superpartners;
- supersymmetric particles are always produced in even numbers.

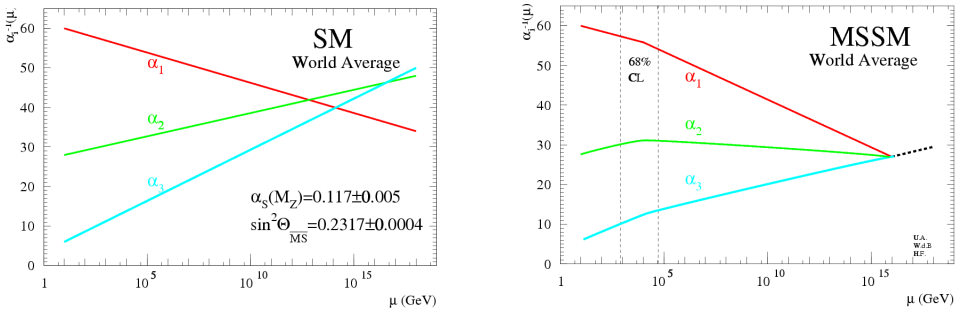

(a) (b)

Figure 1.17: Evolution of the electroweak, strong, and gravitational coupling constants with the energy scale of the interactions for (a) the Standard Model alone and (b) the Minimal Supersymmetric extension of the Standard Model (MSSM).

The first thing to be noticed is that superpartners of standard particles (e.g. a scalar electron) with the same mass would have already been detected in experiments. Since none of them has been observed so far, despite extensive searches at collider machines, the supersymmetry must be broken in a realistic theory. However, the feature of having $\lambda_f = \lambda_s$ to all orders in perturbation theory, that cancel the divergences of the Higgs mass, must be preserved in the broken theory.

The mechanism by which the supersymmetry is broken is the main difficulty in building a supersymmetric extension of the Standard Model. Two are the main solutions proposed.

The first one consists in introducing a so-called soft breaking term in the Standard Model Lagrangian, that is the most general supersymmetric breaking term preserving $\lambda_f = \lambda_s$. This parametrize our ignorance of the breaking mechanism with the introduction of 105 free parameters into the theory that can be reduced by further assumptions based on experimental constraints (e.g. absence of Flavour Changing Neutral Current processes, CP violation etc.).

The second mechanism involves gravity and is generally referred to as the gravity-induced supersymmetry breaking (mSUGRA). It is the results of some underlying mechanism that breaks the symmetry at a very large scale, presumably compatible with the Planck mass scale.

An encouraging indirect evidence of supersymmetry is that the unification of the coupling constant at high energies works better than in the Standard

Model tout-court, as it is shown in figure 1.17. Moreover, supersymmetry is predicted as a natural consequence by most of the attempt to build grand-unified theories (e.g. string theories).

1.3.2 Extra-dimensions

A second possible extension of the Standard Model is based on phenomenological theories involving the gravitational interaction. The general idea behind these theory is to solve the hierarchy problem bringing the gravity down to the weak interaction scale, obtaining the observed Planck mass scale as a results of a $(4+n)$-dimensional world. In our 4-dimensional space gravity would appear weak, as force lines would escape in extra dimensions. The starting point is the observation that electroweak interactions have been probed at distances $\sim \Lambda_{\text{E.W.}}^{-1} = m_W^{-1}$ while gravitational forces have been investigated only to distances of the order of $\sim$ 1 cm, which is 33 orders of magnitude greater than the intrinsic energy scale of gravity, given by $\sim m_P^{-1}$. The assumption that gravity at $\sim$ 1 cm would be the same at $\sim m_P^{-1}$ is then not completely justified. Changes could happen in between.
The proposed theories can be mainly divided into two classes, according to the kind of extra dimension proposed:

- flat compactified extra dimensions;
- warped extra dimensions.

Each of the two previous categories can be divided in two groups:

- gravitational extra dimensions: only the gravitational fields can propagate in extra dimensions;
- universal extra dimension: Standard Model fields and gravitational fields can propagate in extra dimensions.

In the following the principal ideas behind flat compactified and warped gravitational extra dimensions will be briefly illustrated.

A scenario proposed by Arkani-Hamed, Dimopoulos, Dvali (Arkani-Hamed *et al.*, 1998) is that in addition to the space-time dimensions we live in, there are n compact spatial dimensions of radius $\sim R$ accessible to the gravity but not to the other three fundamental forces. Standard Model particles cannot freely propagate in $4+n$ dimensions but would be localized on the four-dimensional subspace (submanifold). The only fields propagating in the

extra-dimensions are gravitons.
The consequence is that in our world gravity manifests itself as an extremely weak force, with typical interaction energies of the order of the Planck scale, despite in the full $(4+n)$ dimensions they are suppress at the weak interaction scale.
At distances $r \ll R$ the gravitational potential between two masses m_1 and m_2 is modified according to the Gauss's law in $(4+n)$ dimensions:

$$V(r) \sim \frac{m_1\, m_2}{m_{P(4+n)}^{n+2}} \cdot \frac{1}{r^{n+1}} \quad , \quad r \ll R. \tag{1.63}$$

On the other hand, when the distance between the two masses is much greater than R, then their gravitational flux lines can no longer penetrate inside the extra dimensions, and the usual $1/r$ potential is obtained:

$$V(r) \sim \frac{m_1\, m_2}{m_{P(4+n)}^{n+2}} \cdot \frac{1}{r} \quad , \quad r \gg R. \tag{1.64}$$

The effective 4-dimensional m_P is then given by

$$m_P^2 \sim m_{P(4+n)}^{n+2} R^n. \tag{1.65}$$

By assuming that $m_{P(4+n)}$ is of the order of m_W and by demanding R to be such that the observed m_P is reproduced, the following value for R is obtained:

$$R \sim 10^{\frac{30}{n}-17} \cdot \left(\frac{\mathrm{TeV}/c^2}{m_W}\right)^{1+\frac{2}{n}}. \tag{1.66}$$

For $n = 1$ this will imply $R \sim 10^{13}$ cm, so deviation from Newton's law should appear at solar system distances. However, if $n \geq 2$ such deviation would appear only below 1 mm, that is distances not yet probed by experiments.
According to this model, the phenomenology of the Standard Model is enriched with a graviton and all its Kaluza-Klein excitations recurring once every $1/R$, per extra dimension n.

A different model (Randall and Sundrum, 1999) is based on the hypothesis of the existence of at least one extra dimension accessible to gravity and that the metric of the space-time discriminates between the traditional four coordinates and the additional ones.
In particular, considering the case of one extra dimension, the four-dimensional

space has the usual "flat" metric multiplied by a "warp" factor rapidly changing as a function of the additional coordinate:

$$ds^2 = e^{-2kr_c\phi}\eta_{\mu\nu}dx^\mu dx^\nu + r_c^2 d\phi^2 \tag{1.67}$$

where k is a scale of the order of the Planck scale, r_c is the compactification radius, ϕ is the coordinate of the extra dimension ($0 < \phi < \pi$) and η is the usual Minkowski's metric tensor.
The gravity scale, which is at the electroweak scale, is given by

$$\Lambda_\pi = m_P\ e^{-kr_c\pi} \tag{1.68}$$

where $\Lambda \sim 1$ TeV$/c^2$ can be obtained with $kr_c \sim 11, 12$. Massive Kaluza-Klein excitations of gravitons appear with a mass given by

$$m_n = kx_n\ e^{-kr_c\pi} = x_n \left(\frac{k}{m_P}\right) \Lambda_\pi, \tag{1.69}$$

where x_n is the n^{th} root of the Bessel function of order 1 ($x_n = 3.8317$, 7.0156, 10.1735 for $n = 1,\ 2,\ 3$).
The coupling of the graviton to the Standard Model particle is proportional to $1/\Lambda_\pi$. The graviton mass is determined by the ratio k/Λ_π. These are the only two parameters of the Randall-Sundrum model.

Bibliography

Arkani-Hamed, N., Dimopoulos, S. and Dvali, G. (1998), *The Hierarchy Problem and New Dimensions at a Millimiter*, hep-ph/9803315.

Del Duca, V. (2003), *Higgs Production at LHC*, International Workshop on QCD, hep-ph/0312184.

Eidelman, S., Hayes, K. *et al.* (2004), *Review of Particle Physics*, Physics Letters B, **vol. 592**, pp. 1+, URL `http://pdg.lbl.gov`.

Glashow, S. L. (1961), *Partial Symmetries of Weak Interactions*, Nucl. Phys., **vol. 22**, pp. 579–588.

Higgs, P. W. (1964), *Broken symmetries, massless particles and gauge fields*, Phys. Lett. 12 (2) (1964), pp. 132–133.

't Hooft, G. (1976), *Computation of the quantum effects due to a four-dimensional pseudoparticle*, Phys. Rev., **vol. D14**, pp. 3432–3450.

't Hooft, G. (2005), *50 Years of Yang-Mills Theory*, World Scientific Publishing Co.

LEP Electroweak Working Group (1999), *A compilation of the lastest electroweak data from LEP and SLC*, Tech. Rep. CERN-EP/99-15.

Peskin, M. E. and Schroeder, D. V. (1995), *An Introduction to Quantum Field Theory*, Addison-Wesley.

Puljak, I. (2000), *CMS discovery potential for the Higgs boson in the* $H \to ZZ^{(*)} \to 4e^{\pm}$ *decay channel. Contribution to the construction of the CMS electromagnetic calorimeter*, Ph.D. thesis, Université Paris VI.

Randall, L. and Sundrum, R. (1999), *A Large Mass Hierarchy from a Small Extra Dimension*, hep-ph/9905221.

Renton, P. (1990), *Electroweak Interactions - an introduction to the physics of quarks and leptons*, Cambridge University Press.

The ALEPH, DELPHI, L3, OPAL, SLD Collaborations, the LEP Electroweak Working Group, the SLD Electroweak and Heavy Flavour Groups (2005), *Precision Electroweak Measurements on the Z Resonance*, p. 302. `hep-ex/0509008`.

Weinberg, S. (1967), *A Model of Leptons*, Phys. Rev. Lett., **vol. 19**, pp. 1264–1266.

Yang, C.-N. and Mills, R. L. (1954), *Conservation of isotopic spin and isotopic gauge invariance*, Phys. Rev., **vol. 96**, pp. 191–195.

Chapter 2

The CMS Detector at LHC

In spite of the remarkable accuracy in the description of elementary particles interactions, the Standard Model does not yet give an answer to a number of fundamental questions (see chapter 1). Building upon its past strength of understanding open problems, the physics community has focused its attention to hadron colliders, which are particularly suitable for the discovery of new physics. The Large Hadron Collider (LHC) at CERN, presently under construction, represents the new generation of hadron colliders and will undoubtedly help to fill gaps in our knowledge.
After a brief description of the machine, the chapter will focus on CMS, one of the two general purpose detectors (ATLAS and CMS) which will be installed at LHC along with two experiments specifically oriented to b physics (LHCb) and heavy ions physics (ALICE). Particular emphasis will be given to the main focus of this thesis, the technical aspects and expected performances of the electromagnetic calorimeter of the CMS detector.

2.1 The Large Hadron Collider

The LHC will provide proton-proton collision at a center of mass energy of 14 TeV/c^2 (7 + 7). The available energy for the interactions of the proton elementary constituents will then reach the TeV range, which is about one order of magnitude greater than the typical LEP and Tevatron interaction energies.
The LHC will be placed in the already existent 26.7 km long LEP tunnel and is supposed to start its activity in 2007. Since collisions will occur between particles of the same charge, two separate acceleration cavities with

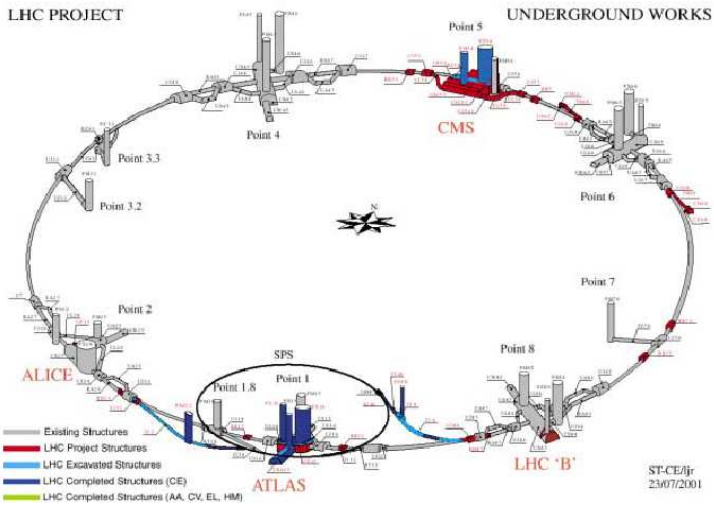

Figure 2.1: Layout of the Large Hadron Collider with the four experiments that will be located at each interaction point.

two different magnetic field configurations are required. Superconducting dipoles operating at 1.9 K will provide a $\sim$ 8.4 T magnetic field. Boosts will be given by 400 MHz superconducting radiofrequency cavities with a voltage ranging between 8 and 16 MV. The channels for the two beams acceleration will be inserted in a single cryostat.

Protons will be delivered to LHC by an upgrade of the CERN existing facility. This facility will bring the protons to the injection energy into LHC of 450 GeV in four steps (figure 2.1): the LINAC will bring them to 50 MeV, the Booster will further accelerate them up to 1.4 GeV, the PS to 25 GeV and the SPS will inject them into the LHC at their initial energy of 450 GeV after a final acceleration step..
The bunches, with a nominal number of 10^{11} protons each, will have a very small transverse spread ($\sigma_x \approx \sigma_y \approx 15$ μm) and will be 7.5 cm long in the beam directions at the collision points. A summary of the main technical parameters of LHC is given in table 2.1.

The luminosity of an accelerator that collides bunches of n_1 and n_2 particles at a frequency f is given by

$$\mathcal{L} = f\frac{n_1 n_2}{4\pi\sigma_x\sigma_y}, \tag{2.1}$$

Parameter	Value
Circumference [km]	27
Number of magnet dipoles	1232
Dipolar magnetic field [T]	8.386
Magnet Temperature [K]	1.9
Beam energy [TeV/c^2]	7
Nominal luminosity [cm^{-2}s^{-1}]	10^{34}
Protons per bunch	$1.05 \cdot 10^{11}$
Bunch spacing [m]	7.48
Bunch time separation [ns]	24.95
Transverse beam size @ I.P. [μm]	200
rms bunch length [cm]	7.5
Crossing angle [rad]	$2 \cdot 10^{-4}$
Beam lifetime [h]	7
Luminosity lifetime [h]	10

Table 2.1: Main technical parameters of the Large Hadron Collider.

where σ_x and σ_y represent the Gaussian beam profile in the plain transverse to the beam axis.
The nominal LHC luminosity is $\mathcal{L} = 10^{34}$ cm^{-2}s^{-1} and corresponds to an integrated luminosity over one year of LHC running of 100 fb^{-1}. This will value be reached after an initial phase at $\sim 10^{33}$ cm^{-2}s^{-1} (so called "low luminosity" phase) which will be mainly dedicated to tune the detector performances, to search for new particles and to study the quark b physics.

The requirements on the Large Hadron Collider create several challenges from the experimental point of view. The need of high statistics to detect rare process requires very high luminosity, with the consequences of a high event rate due to common QCD processes and an extremely dense particle environment.
Indeed, the total p-p cross section at the LHC energy is estimated to be $\sim$ 100 mb (Eidelman *et al.*, 2004), which, given the machine parameters, implies an average of about 20 p-p interaction per bunch crossing, 10^9 interactions per second. A strong online event selection is therefore needed in order to reduce the event rate at around 10^2 Hz, 7 orders of magnitude less, which corresponds to the maximum data storage rate reachable with the existing device technology. An excellent time resolution is also needed

to distinguish events belonging to different bunch crossings, which are separated only by 25 ns.
Regarding the challenge given by the particle density, a typical minimum bias collision at LHC will produce on average 5.5 charged particles with mean transverse momentum around 0.5 GeV/c and 8 primary photons per unit of pseudorapidity. An interesting event, which typically contains high p_T leptons, high E_T hadron jets, b-jets, large missing transverse momentum, will always be superimposed on this pile-up. Detectors must hence have fine granularity in order to separate particles very close in space by means of sophisticated reconstruction algorithms.
Moreover, to extract as much information as possible from an interesting signal, multi-purpose detectors should also fulfill the following requirements:

- full hermeticity to allow for an accurate measure of the missing transverse energy and momentum (coming from almost non-interacting particles, like neutrinos or supersymmetric neutralinos);
- capability to reconstruct leptons in a wide range of transverse momenta and rapidity (to reconstruct gauge bosons, tag b-jets etc.);
- capability to reconstruct charged tracks with a good precision on their transverse momentum and impact point position (to efficiently reconstruct and tag B particles and τ);
- capability to reconstruct hadron jets from QCD process and heavy particles decays.

A very high particle flux traversing each component of the detector also impose restrictive requirements on the material that can be used for the detector construction: the best results will be obtained with the optimal compromise between detector performance and particle radiation resistance.

2.2 The Compact Muon Solenoid

In order to satisfy the previous basic requirements, CMS has opted for a compact detector in a solenoidal magnetic field coaxial with the beam-line. The philosophy adopted for the detector design has been:

i) a redundant efficient muon detection system;

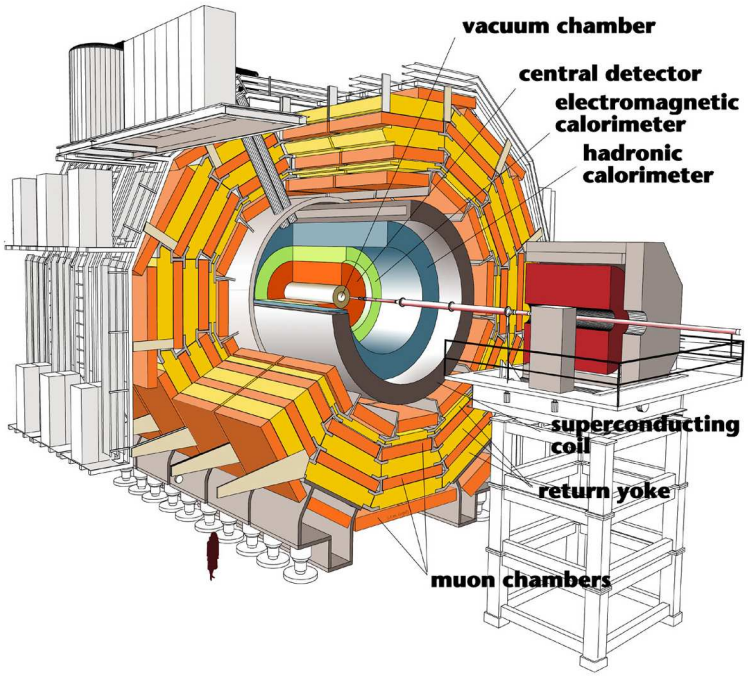

Figure 2.2: Three dimensional representation of the CMS detector.

ii) the best calorimetry compatible with i);

iii) a high quality central tracking to achieve both i) and ii);

iv) a hadron calorimetry with a 4π solid angle coverage;

v) a financially affordable detector.

The apparatus exhibits a cylindrical symmetry around the beam direction and detectors are installed following an onion-like structure of consecutive layers in the central region (barrel) and several disks in the forward region (endcaps). A schematic view of the CMS detector is given in figure 2.2 and a longitudinal view of one quarter of the detector in figure 2.3. The full length is 21.6 m, the diameter is 15 m, for a total weight of $\sim$ 12500 t and an average density of ~ 3.3 g cm^{-3}.
Tracking and calorimetry sub-detectors are placed inside the superconducting solenoid while the muon system is integrated in the return yoke of the magnetic field.
In the following discussion, the different detector components will be described in detail, with particular emphasis for the electromagnetic calorime-

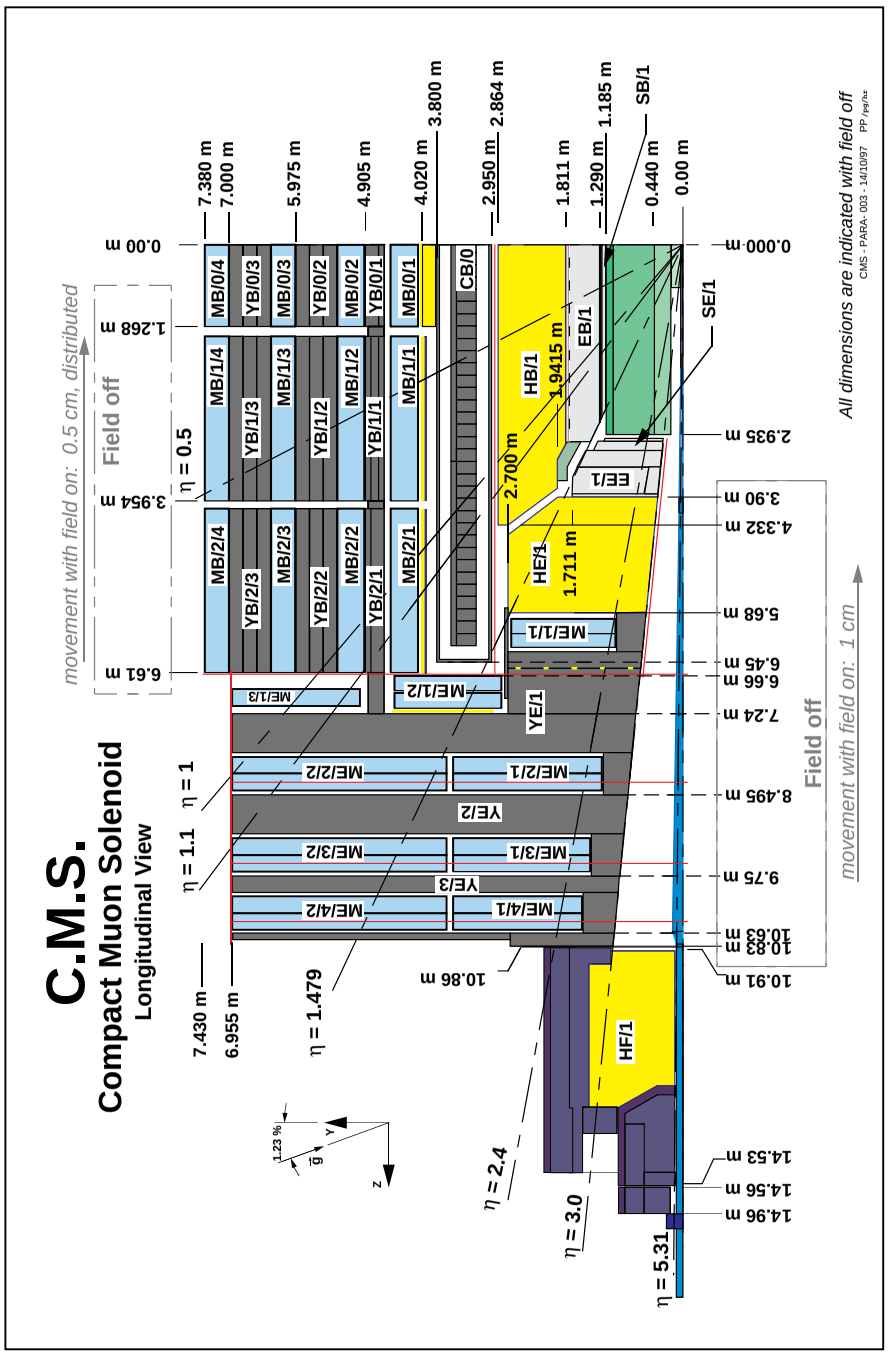

Figure 2.3: Longitudinal schematization of a quarter of the CMS detector. Two letter codes indicate the main detectors. The firs letter refer to the subdetector (S: Silicon tracker; E: Electromagnetic calorimeter; H: hadron calorimeter; M: muon chambers; C: magnet coil; Y: magnet return yoke) while the second one refer to the position (B: barrel; E: endcaps; F: forward region).

ter which will be the focus of the following chapters of this thesis.

2.2.1 Magnet

The choice of a compact design for the CMS detector imposes a strong solenoidal magnetic field in order to achieve the needed resolution on the muon momentum measure.
The magnet system (CMS Collaboration, 1997d) provides a uniform magnetic field of 4 T using a 13 m long superconducting coil with a diameter of 5.9 m. The magnetic flux is returned via a 1.8 m thick saturated iron yoke. The solenoid is composed by the winding (divided in four parts) with its structural support, the thermal radiation shields and the vacuum tank.
The conductor consists of three concentric parts: the central flat superconducting cable (Rutherford type, NbTi) with high purity aluminum stabilizer and two external aluminum-alloy reinforcing slabs.
The cooling system was chosen to be extremely reliable to protect against sudden power failure, since a complete re-cooling from a non-superconducting state needs twelve days.
Being the largest element of the CMS detector, the magnet is also providing the principal support structure for all the barrel detector components (tracking and calorimetry inside the coil, muons stations outside).
The magnet system includes the cryogenic system, power supply, quench protection vacuum pumping and control system.

2.2.2 Tracker

The tracker is the CMS sub-detector closest to the interaction point and is devoted to the reconstruction of charged tracks and vertices ((CMS Collaboration, 1998), (CMS Collaboration, 2000a)).
The design goal of the central tracking system is the reconstruction of isolated p_T leptons with an efficiency better than 95% and of high p_T tracks within jets with an efficiency better than 90% over the pseudorapidity range $|\eta| < 2.5$. A momentum resolution of $\Delta p_T/p_T \sim 0.1 p_T$ (p_T in TeV/c) is needed to allow the measurement of the lepton charge up to transverse momenta of 2 TeV/c.
Moreover, the accurate vertex identification and measurement will be crucial for many physical purposes, from the Higgs discovery to physics of the

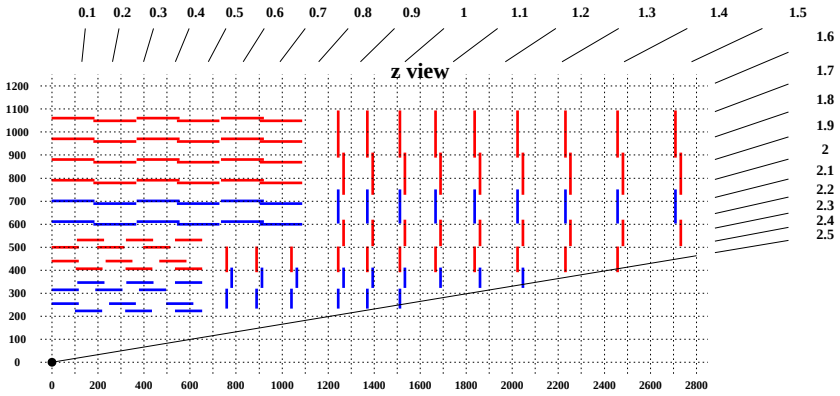

(a)

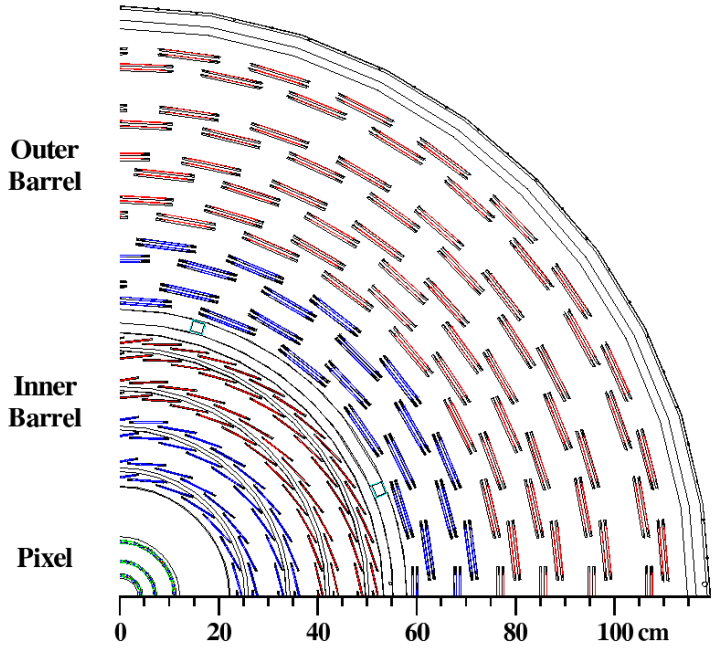

(b)

Figure 2.4: Schematic longitudinal (a) and transverse (b) view of a quarter of the tracker layout. Red lines represent single modules, blue lines double modules.

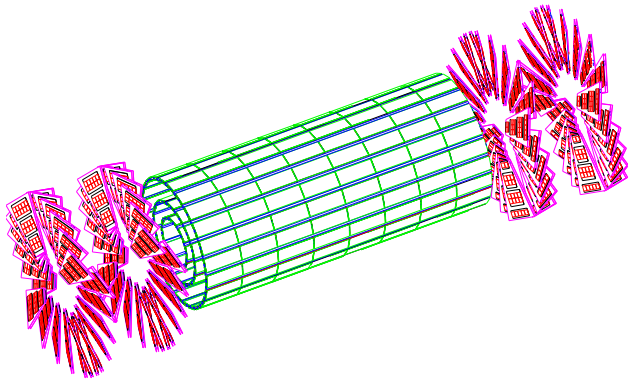

Figure 2.5: Three dimensional view of the silicon pixel detector of the CMS tracker.

b quark and of new massive (supersymmetric?) particles.

A high granularity is needed to reduce the detector occupancy and so to distinguish tracks and provide a good precision in the extrapolation of the primary vertex in the conditions of LHC. The tracker is entirely based on semiconductor devices and is composed of three parts (figure 2.4).

The innermost part is made of three layers of silicon pixel detectors (fig. 2.5), covering a pseudorapidity range up to $|\eta| = 2.4$. It is surrounded by an intermediate and outer part made of silicon microstrips of different design and thickness which provide an efficient pattern recognition together with a precise momentum measurement and a good matching with the outer detectors.

One of the major constraints on the design of a tracking system is to reduce as much as possible the amount of material distribution in front of the subsequent calorimeters. For the CMS tracking the material budget is shown in figure 2.6 and constitutes the main source of error in accurate calorimetric measurements of photons (which convert into electron-positron couples) and

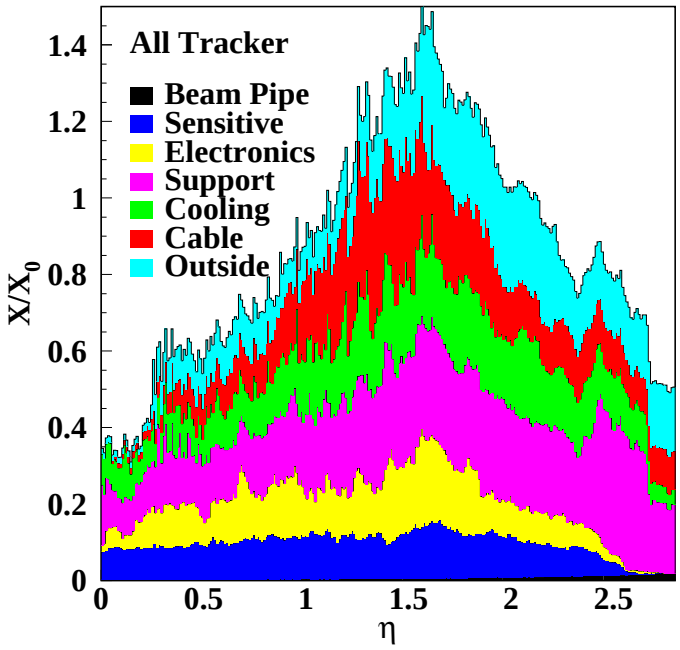

Figure 2.6: Material budget distribution for the CMS Tracker.

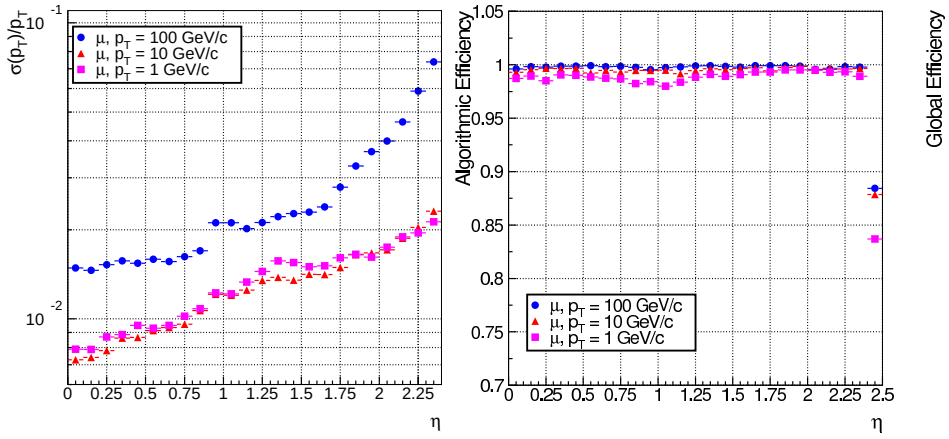

(a) (b)

Figure 2.7: (a) Transverse momentum resolution as a function of the pseudorapidity of the track. (b) Global track reconstruction efficiency for the CMS tracker detector for single muons of different transverse momenta.

electrons (which emit a large fraction of their energy by bremsstrahlung). Such errors are for example directly affecting the detector resolution in the search for the Higgs in the golden channel $H \to \gamma\gamma$ and are affecting also all the channels with electrons in the final state, in particular $H \to ZZ^{(*)} \to 4e$. Detailed studies on electrons to evaluate all these effects are presented in the following chapters.
The general tracking performance is here summarized (figure 2.7):

- the p_T resolution is better than $\Delta p_T/p_T \sim (15 p_T \oplus 0.5)\%$ (p_T in TeV/c) in the pseudorapidity range $|\eta| < 0.7$, slightly worse in the forward region (figure 2.7(a));

- the efficiency for single muons reconstruction is greater than 98% over the whole η coverage (figure 2.7(b)) and for single electrons reconstruction around 95% in the central region;

- the efficiency for the reconstruction of hadrons inside jets is around 80% for $p_T > 1$ GeV/c and around 95% for $p_T > 10$ GeV/c;

- the resolution in the transverse impact parameter for the reconstructed tracks is about 20 μm for 10 GeV/c particles.

Furthermore, the possibility to read a single region of the tracker allows both to lower the time needed to perform the reconstruction and the use of the tracker detector in a very early stage of the trigger system.

2.2.3 Electromagnetic Calorimetry

The CMS Electromagnetic Calorimeter (ECAL) (CMS Collaboration, 1997a) is the fundamental subdetector of CMS to search for the Higgs boson in the channel $H \to \gamma\gamma$, which is considered the golden channel for low Higgs masses. Moreover, the detection of final states containing electrons and photons plays a fundamental role in the investigation of the scenario beyond the Standard Model. In the absence of the Higgs boson particle, such a detection will allow the inference of symmetry breaking hypothesis from the accurate study of WW, WZ and ZZ final states, which should reveal new physics at energies around the TeV/c^2 scale.

Thus the physics benchmark against which the electromagnetic calorimeter performance is measured is the di-photon mass resolution, which is de-

pendent on both energy and angular resolution:

$$\frac{\sigma_M}{M} = \frac{1}{2}\left(\frac{\sigma_{E_1}}{E_1} \oplus \frac{\sigma_{E_2}}{E_2} \oplus \frac{\sigma_\vartheta}{\tan\frac{\vartheta}{2}}\right), \tag{2.2}$$

where $E_{1,2}$ are the energies (measured in GeV) of the two photons, ϑ is the photon angular separation and $\oplus$ denotes a quadratic sum.
The energy resolution σ_E/E is usually parametrized as

$$\frac{\sigma_E}{E} = \frac{a}{\sqrt{E}} \oplus \frac{b}{E} \oplus c, \tag{2.3}$$

where a, b, c are respectively the stochastic, noise and constant term and will be discussed in details later in this section.
In order to maximize the performance, high granularity and good energy measurement need to be achieved at the same time. CMS has opted for an homogeneous calorimeter of $PbWO_4$ scintillating crystals slightly off-pointing with respect to the nominal interaction vertex. This choice offers the best performance for energy resolution, since most of the energy is deposited within the homogeneous crystal volume. The $PbWO_4$ material has high density ($X_0 = 0.89$ cm) and small Molière radius ($\varrho_M = 2.2$ cm), thus allowing a fine granularity for the calorimeter, with the additional advantage of reducing the pileup by minimizing the spread area of the energy. Furthermore, $PbWO_4$ has a short scintillation decay time constant (80% of the light is emitted within 20 ns), resists well to the hard radiation environment of LHC and is relatively easy to produce from readily available raw material. The main drawback of a low light yield with respect to other scintillator materials is well overcome by appropriate readout devices, as described in the following section.

$PbWO_4$ crystals

Some of the properties of this scintillating material have already been mentioned. A summary of the main characteristics of the $PbWO_4$ compared to other crystals typically used for electromagnetic calorimetry is shown in table 2.2.
The optimization of the scintillation light spectrum has led to a Gaussian-shaped distribution with 140 nm of FWHM peaking at about 420 nm with a range from 360 nm to 570 nm at 10% of the maximum.

	$PBWO_4$	NaI(Tl)	BGO
Density [g cm^{-3}]	8.28	3.67	7.13
Radiation length [cm]	0.89	2.59	1.12
Molière radius [cm]	2.2	4.5	2.4
Emission peak [nm]	440	410	480
$1/LY \times dLY/dT$ @ $T = 20$ °C [%/°C]	-2	~ 0	-1.6
LY relative to NaI(Tl)	$1.3 \cdot 10^{-2}$	1	0.15
Scintillation light decay time [ns]	5-15	250	300

Table 2.2: Main properties of the $PBWO_4$ compared to other crystal typically used for electromagnetic calorimetry.

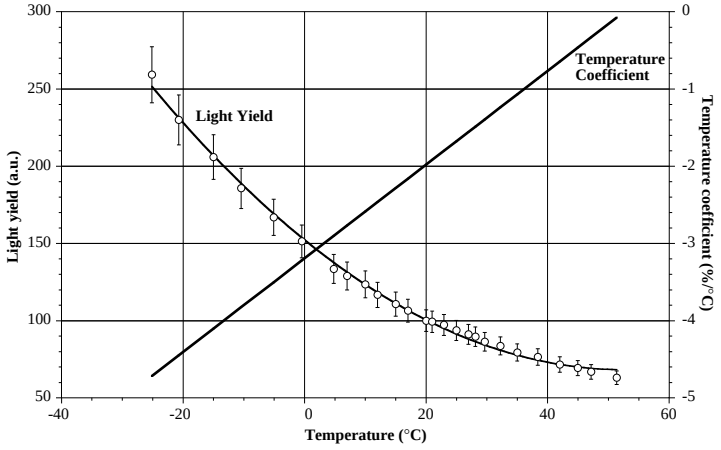

Figure 2.8: Temperature dependence of the $PBWO_4$ Light Yield.

The scintillation decay time is $\sim$ 10 ns. The unusual fast scintillation time with respect to the crystals of the tungstate family can be explained to a large extent by the high-temperature charge transfer process and thermal decomposition of excited state. This thermal quenching of the scintillation process leads to a rather strong temperature dependence of the light emission, with typical variations of $-2\%/°\mathrm{C}$ at room temperature. The temperature dependence of the light yield is shown in figure 2.8. It is then fundamental the detector cooling system, which must stabilize the crystals temperature to 0.05 $°C$.

Lead tungstate is intrinsically radiation hard. Non ideal crystals nevertheless suffer from radiation damage. It has been established during the R&D phase that the damage can be attributed solely to electromagnetic interaction, since no specific neutron damage has been observed. The crystal irradiation does not affect the scintillation mechanism (at least in the dose rate estimated for LHC). Only the lead tungstate transparency is altered within a few percent by crystal irradiation, through the formation of colour centers related to defects in the crystals introduced by mismatched stoichiometry and creation of oxygen vacancies. The loss in the transmission efficiency can thus be monitored by a light injection system in the calorimeter, as briefly described later.
The irradiation does not change the uniformity of the light collection along the crystal, provided an initial light attenuation length long enough and a small damage. The loss in the light yield, stabilizes at a level depending on the radiation dose rate, as expected from the colour center model. The damage recovery in the LHC environment is not expected to be less than a few hours.

Mechanical Design

The CMS electromagnetic calorimeter consists of a barrel part and of two endcaps (fig. 2.9). The main design considerations are strongly related to the requirements imposed by physics of accurate measurements on electron, photons and missing energy. The engineering design should in particular minimize the material in front of the calorimeter, optimize the interface with the tracking system, ensure the best possible hermeticity by minimizing the gaps between crystals and the barrel/endcaps transition region, minimize the space and the material in front of the Hadron Calorimeter to ensure the

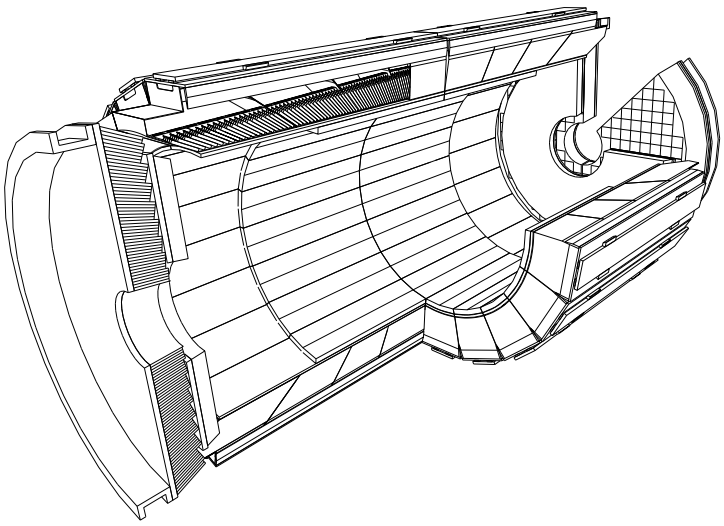

Figure 2.9: Three dimensional representation of the CMS electromagnetic calorimeter. The barrel part and the two endcaps are visible.

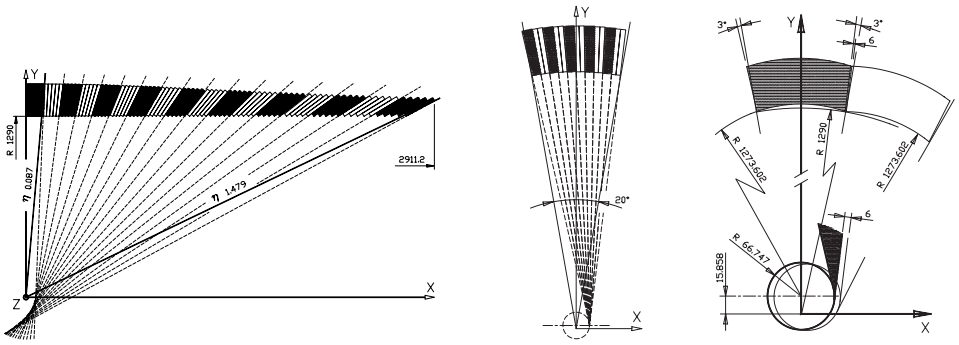

Figure 2.10: *Left*: crystal tilt in η. *Right*: crystal tilt in ϕ.

best possible measurements for jets and missing transverse energy, stabilize the crystal temperature within a tenth of a degree.

The barrel region covers a pseudorapidity range up to $|\eta| < 1.479$ (fig. 2.11). One half-barrel is composed of 18 supermodules subtending each 20° in ϕ. Each supermodule contains four modules along the beam axis, grouping the 500 crystals from the first module and the 400 crystals from each of the remaining three for a total of 85 crystals in η times 20 crystals in ϕ. The truncated pyramid-shaped crystals have a front face covering an

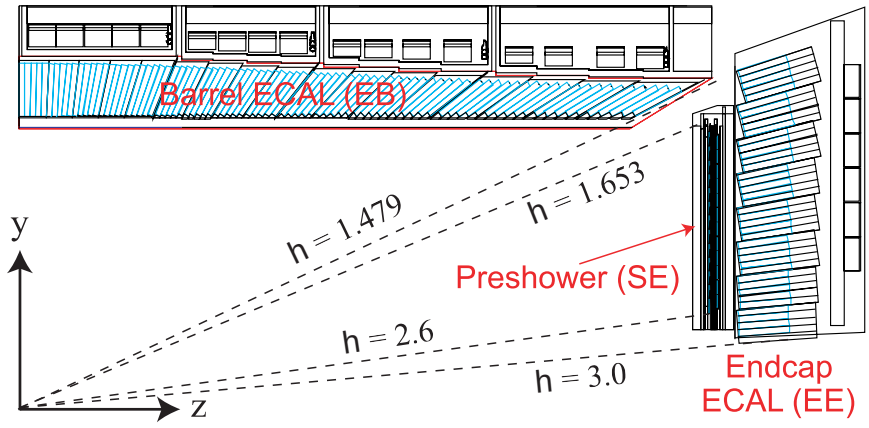

Figure 2.11: Pseudorapidity coverage of a quarter of the CMS electromagnetic calorimeter.

area of about 2.2×2.2 cm^2 and a length of 23 cm, corresponding to ~ 26 radiation length. The barrel granularity is of $\Delta\eta \times \Delta\phi = 0.0175 \times 0.0175$. Seventeen types of crystals are mounted in a geometry which is off-pointing with respect to the nominal position of the interaction point, with a 3° tilt in both η and ϕ (fig. 2.10).
All supermodules are equipped with a cooling system providing a stability of the crystal array and readout devices within a tight spread of 0.05 °C.

The endcaps of the calorimeter provides accurate energy measurement in the pseudorapidity range from $|\eta| > 1.48$ to $|\eta| < 2.6$ (fig. 2.11). In order to increase the information for energy-flow measurements, crystals will be installed up to $|\eta| < 3$. The endcaps realize an off-pointing pseudo-projective geometry grouping crystals of the same shape and dimension ($2.6 \times 2.6 \times 22$ cm^3) in 5×5 arrays called supercrystals. The shorter size of the crystals is due to the presence of a $3X_0$ thick preshower detector in front of the calorimeter.

Readout System

Due the relatively low light yield of lead tungstate, the readout devices used to extract the crystal signal become very important. They in particular need to provide a first amplification stage for the signal before the injection in the electronic readout chain. The requirement of radiation hardness and the presence of a strong magnetic field lead to the choice of Avalanche Photo-

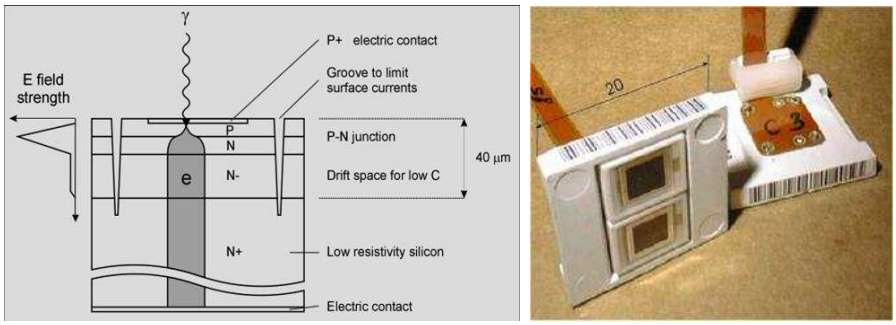

Figure 2.12: *Left*: principle of operation of an Avalanche PhotoDiode. *Right*: pair of APD detector to be installed on a crystal rear face.

Diodes (APDs) for the barrel region and of Vacuum PhotoTriodes (VPTs) in the endcaps.

Avalanche PhotoDiodes (APDs)

The use of avalanche photodiodes for the crystal readout presents several advantages: they are fast detectors ($\sim$ 2 ns of rise time), they have a very good quantum efficiency of 70-80% around $\lambda = 420$ nm and they are highly insensitive to magnetic fields. Furthermore, they present good compactness (overall thickness of 2 mm) and can be manufactured in large quantities with a small spread in the performance parameters. Since their area of 25 mm^2 is small compared to the crystal rear face, two of them are used to detect the scintillation light from each crystal.

Optimized for the detection of the lead tungstate light spectrum, their basic structure is shown in figure 2.12: the light enters via the p^+ layer and is absorbed in the p layer behind, where electron-hole pairs are generated. A drift in the p-n transition region is followed by an amplification stage in the n volume (gain tunable between 50 and more than 10^3) and by an intrinsic drift region before the charge is collected by the cathode. In the APDs with this reverse structure, the response to ionizing radiation is to the first order proportional to the thickness of the p^+ layer, which is only 4-5 μm: this results in a response typically between 2-4% compared to a standard PIN photodiode.

Radiation damage to which APDs are exposed occurs through two mechanisms: surface damage, that causes defects in the front layers, and bulk damage, due to the displacement of atoms from their lattice sites. While the first has the effects of increasing the surface current and reduces the

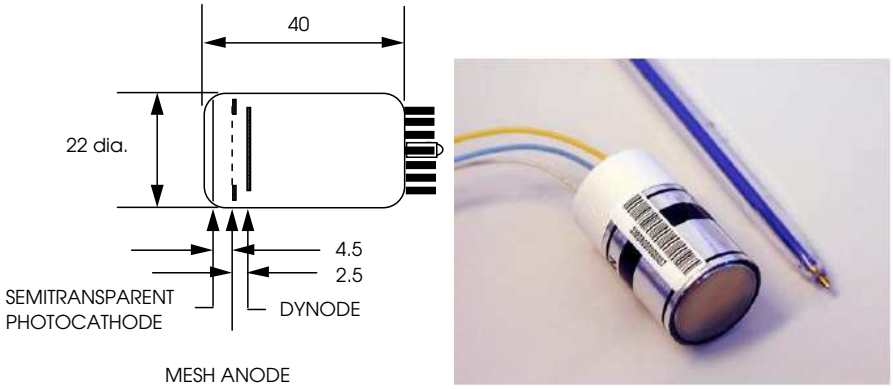

Figure 2.13: *Left*: principle of operation of a Vacuum PhotoTriode. *Right*: picture of a VPT detector.

quantum efficiency, the latter can change the bulk current and consequently the gain. Results on dedicated tests have shown no effects of gain change while an increase in the dark current of a factor 2 is expected after 10 years of running of LHC.
For operating the APD with the CMS front-end electronics, the optimum gain sits in a broad minimum between 50 and 100 and is has been decided to operate at gain 50. As for all APDs, the gain is temperature dependent: for the CMS APD the variation is $-2.2\%/°C$, which is of the same magnitude and of the same sign as the variation of the light transmission of the crystal: the temperature stability of the detector will be crucial.

Vacuum PhotoTriodes (VPTs)

Although the APDs used in the barrel have a very good performance, they are insufficiently radiation-hard to be used over the whole rapidity range of the calorimeter: in the endcap regions vacuum phototriodes will be employed.
A schema of the VPT as well as a picture of a prototype is given in figure 2.13. Photoelectrons are produced by the lead tungstate scintillation light impinging on a planar semitransparent photocathode made of radiation-hard glass. They are then accelerated by an ultra fine mesh (100 wires/mm) and impact on a dynode, producing secondary electrons with an emission factor up to 20. The secondary electrons are attracted back to the anode mesh where a substantial fraction is captured, leading a total effective gain for the VPT greater than 8 in a magnetic field of 4 T.

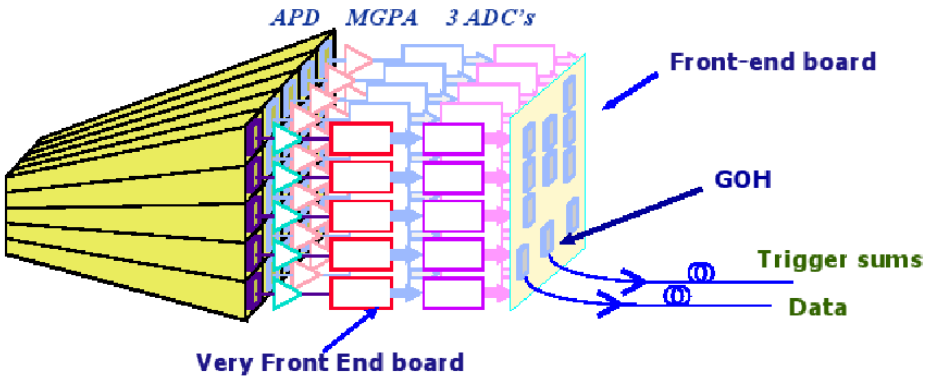

Figure 2.14: Schematic representation of the electronic readout for a group of 5×5 crystals of the CMS electromagnetic calorimeter.

The lower quantum efficiency with respect to the APD is compensated in the CMS ECAL design by a larger active area ($\sim$ 280 mm^2), so that the total detector response is almost the same for barrel and endcap regions.
The radiation hardness for the VPT's is such that the loss in the window transmission is kept below 4% after ten years of LHC running, provided that UV glass is used for the window.
The temperature dependence on the photocathode response is expected to be well below 1%/ °C.

Readout Electronics

The electronics readout of the CMS Electromagnetic Calorimeter need to be very fast, in order to match the bunch crossing time of 25 ns, and to provide very precise energy measurements over a wide dynamic range, from 30 MeV/c^2 up to 1.5 TeV/c^2. Considering the additional requirement of radiation hardness and large amount of channels, this led to a custom-designed choice of the electronic circuits.
As it is schematically represented in figure 2.14, the readout electronics on the detector is composed of group of eight Printed Circuit Boards (PCB) reading an array of 5×5 crystals. This corresponds to reading a trigger tower in the barrel region and a supercrystal in the endcap regions. Each group is composed of five Very Front-End electronics cards (VFE) and one Front-End electronics card (FE). One Low Voltage Regulator card (LVR) is also used to distribute regulated voltage to the VFE cards and a mother-board card filters and distributes high voltage to the photodetectors.

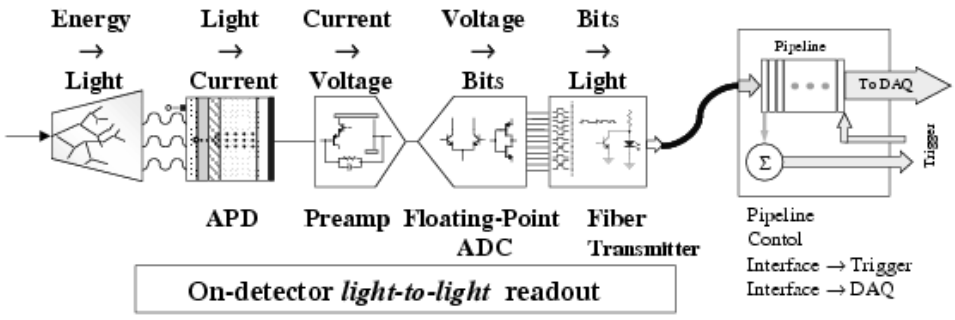

Figure 2.15: Schema of the ECAL readout chain.

As shown in figure 2.15, the signals from the two APD's are pre-amplified and shaped by a trans-impedance amplifier with internal shaping, followed by a three-range amplification stage where a Multi-Gain Pre-Amplifier (MGPA) provides three analogue output signals at three different gains (1, 6, 12). These three signals are digitized in parallel by a four-channel, 12-bit, 40 MHz ADC with an integrated digital gain switching logic. Both the MGPA and the four-channel ADC chips are realized using a radiation-hard 0.25 μm CMOS technology.
The VFE board has five such readout channels and feeds the digitized outputs to a FE board, which stores and process the data during the Level-1 trigger latency of $\sim$ 3 μs. The trigger data are transmitted to the off-detector electronics through a serial digital data optical link operating at 800 Mbyte/s. On receipt of a L1-trigger, the data stored on the FE card corresponding to the triggered event are transmitted through a second optical link to the off-detector electronics, for further trigger analysis (High-Level Trigger).

Energy Resolution

As already mentioned in the introductory section, the energy resolution of an homogeneous electromagnetic calorimeter can be parametrized as:

$$\frac{\sigma_E}{E} = \frac{a}{\sqrt{E}} \oplus \frac{b}{E} \oplus c, \tag{2.4}$$

where a, b, c are respectively the stochastic, noise and constant term. In this section the different contributions to each term will be analyzed in detail.

Stochastic term

The stochastic term a is a direct consequence of the statistics associated with the electromagnetic shower development in the calorimeter and the successive scintillation light recollection.
This term represents the intrinsic resolution of an ideal calorimeter, that is a calorimeter with infinite size and no response deterioration due to instrumental effects. The original energy E_0 of a particle impinging on the calorimeter is directly proportional to the total track length T_0, defined as the sum of all ionization tracks due to all charged particles in the electromagnetic cascade. Since T_0 is proportional to the number of track segments in the shower and the shower development is a stochastic process, the intrinsic resolution from purely statistical arguments is given by

$$\frac{\sigma(E)}{E} \propto \frac{\sqrt{T_0}}{T_0} \propto \frac{1}{\sqrt{E_0}}. \tag{2.5}$$

For a realistic calorimeter, this term also absorbs the effects related to the shower containment and to statistical fluctuations in the scintillation light recollection due to geometry effects, quantum efficiency of the photodetectors and electron multiplication processes inside the photodetector.
For the CMS ECAL calorimeter, fluctuations on the lateral containment of the shower give a contribution of 1.5% if the energy deposited in a cluster of 5×5 crystals is considered. All the contribution due to the photostatistics are kept below 2.3% if more than 4000 photoelectrons per GeV are produced by the photodetectors. In the endcap regions, where a preshower is installed in front of the calorimeter, an additional contribution of about 5% related to the fluctuations on the energy deposited in the absorber needs to be considered: this is the dominant contribution to the stochastic term for the energy resolution in the endcaps.

Noise term

The noise term is strongly related to the detector technique and to the features of the readout circuit (detector capacitance, cables, devices etc.). In the CMS electromagnetic calorimeter, photodetectors contribute via their intrinsic capacitance and via leakage currents. In the latter case, the contribution is proportional to the radiation absorbed and, in the barrel, is expected to be 8 MeV per channel after one year of operation at low luminosity and 30 MeV at the end of the first year of operation at high luminosity. The noise introduced by the pre-amplifier stage of the electronic readout is

expected to be around 30-40 MeV in the barrel and 150 MeV in the endcaps. The noise introduced in the digitization step is negligible with respect to the other contributions.
A final contribution to the noise term comes from pileup events: in a cluster of 5×5 crystals and during the low luminosity phase of LHC, the contribution is expected to be of ~ 30 MeV in the barrel region and of ~ 175 MeV in the endcaps, thus compatible with total electronic noise.

Constant term

The constant term c is particularly important, being the asymptotic value of the energy resolution at high energies.
All the systematics defects connected to the detector construction and assembly enters in this term as well as all the instability of temperature, voltage etc. during its operation. Here is a summary of the main contributions.

- Non-uniformity of the longitudinal light collection: because of the truncated pyramid-shape of the crystal and the high refractive index ($n = 2.16$), a strong focusing effects on the scintillation light cause non-uniformity in the light-yield. In order to avoid this effect, one of the lateral faces of the crystals is depolished during the production process. An appropriate depolishing procedure allows to keep this contribution below 0.3%.

- Longitudinal shower containment and uncorrected or imperfectly corrected geometrical effects: test beam studies and an accurate simulation have shown that the constant term contribution due to these effects is lower than 0.2%.

- Crystal-to-crystal intercalibration errors. Since a typical electromagnetic shower is not entirely contained inside a single crystal, the relative crystal calibration can introduce systematic errors on the energy measurement.

- Temperature stability. As we have seen, both the emission of scintillation light and the APD gain are temperature dependent. To keep the contribution to the constant term below 0.1%, a temperature stability within 0.05 °C need to be achieved over the full detector volume. Temperature measurements during test beams have shown that this limit can be reached.

Contribution	Barrel ($\eta = 0$)	Endcap ($\eta = 2$)
Stochastic term	$2.7\%/\sqrt{E}$	$5.7\%/\sqrt{E}$
Shower containment	$1.5\%/\sqrt{E}$	$1.5\%/\sqrt{E}$
Photostatistics	$2.3\%/\sqrt{E}$	$2.3\%/\sqrt{E}$
Preshower sampling	-	$5\%/\sqrt{E}$
Electronic noise low (high) $\mathcal{L}$	155(210) MeV	770(915) MeV
Preamplifier low (high) $\mathcal{L}$	150(150) MeV	750(750) MeV
Leakage current low (high) $\mathcal{L}$	30(110) MeV	–
Pileup low (high) $\mathcal{L}$	30(95) MeV	175(525) MeV
Constant term	0.55%	0.55%
Shower containment	$< 0.2\%$	$< 0.2\%$
Longitudinal non-uniformity	0.3%	0.3%
Calibration	0.4%	0.4%

Table 2.3: Contribution to the energy resolution in barrel and endcap for an array of 5×5 crystals. The values reported are the design goal for the calorimeter.

- High voltage stability. The APD gain strongly depends on the bias voltage: in order to keep the constant term contribution below 0.1% the stability on the high voltage has to be better than 30 mV. Test beam studies have shown that the high voltage system fulfill the requirements.

In table 2.3 the different contributions are reported, assuming the energy measured in a 5×5 crystals array during a the low luminosity phase of LHC.

Calibration

In order to reach a constant term contribution of 0.5% in the energy resolution, a major effort has to be made to achieve the best possible calibration of the calorimeter. In the following we will make the distinction between intercalibration and absolute calibration of the crystals, which involve different problematics and strategies.

The intercalibration procedure relies on several steps, having the goal to achieve a final precision of 0.5%. A summary of the different intercalibration strategies before the installation of the calorimeter in CMS is given in the following.

- Laboratory measurements of the crystal light yield: they allow the a precision of 4.5% on the whole calorimeter;
- Electron beam intercalibration: performed at CERN on the H4 beam line it will allow precision below 0.5% on a restricted number of supermodules (due to time constraints). The calibration constant determined with this method are expected to be valid in the final CMS setup within 2%.
- Cosmic rays intercalibration: it will be performed on all supermodules and will reach a precision of about 3%.

The final precision below 0.5% will be reached *in situ* using physics events. In particular, the most important strategies already studied are the following.

- Intercalibration of ring of crystals in ϕ. It assumes that the crystal activity will have an azimuthal symmetry and will be possible very quickly after the start-up.
- Intercalibration using $Z \to e^+e^-$ events. The relatively high rate of Z production and the clear signature of the decay in an electron-positron couple will assure sufficient data for a nearly continuous intercalibration which will not depend on any other CMS sub-detector. The strong correlation between the two electrons will allow to intercalibrate small regions in η-ϕ as well as ϕ rings of crystals already calibrated in the previous point. A cross-calibration of the endcaps with respect to the barrel events will be possible using events with one electron in the barrel and the other in the endcaps.
- Intercalibration of regions of crystals using the tracker momentum. The use of isolated electrons from W and Z decays to calibrate the calorimeter using the ratio E/p where the tracker gives the measure of the momentum has been extensively studied.

In addition to these methods, it will be crucial to fix the absolute energy scale of the calorimeter. This can be done using physics events in which a particle (namely a Z boson) decays into an electron-positron couple (but also the decay of π^0, η^0 etc. into two photons can be used). The kinematical constraint given by the invariant mass of the particle will give the absolute calibration of the calorimeter.

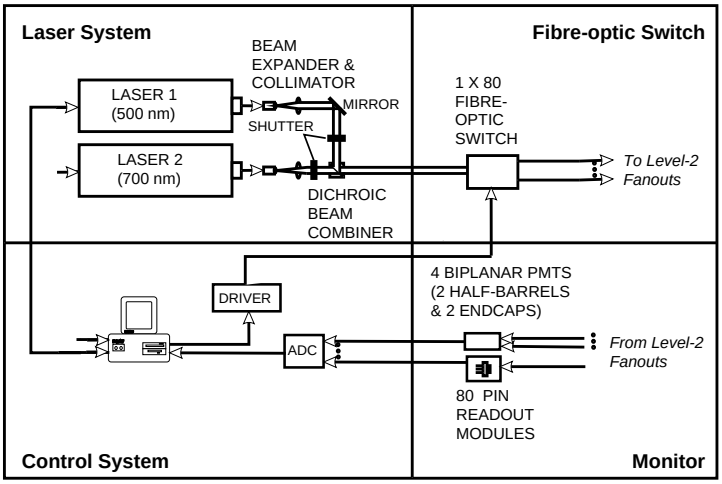

Figure 2.16: Schema of the light source and distribution system for the CMS ECAL monitoring.

It has to be mentioned here that the absolute calibration as well as some intercalibration methods involving the tracker rely on the assumption that the used electrons did not loose energy by bremsstrahlung in the tracker material. However, this is true only for a small fraction of the events. Much care is needed in order to understand the goodness of an electron measurement and to exploit from the different CMS sub-detector as much information as possible to identify the topology of an electron event. It will be crucial, then, to classify the electrons in order to take into account all the systematic effects related to the propagation in the tracker material.
This problem will be largely discussed in the chapter 4 where a detailed analysis on the electron reconstruction inside CMS will be presented.

Monitoring

Although the lead tungstate scintillation mechanism is not affected by charged particles irradiation, the crystal transparency is expected to decrease with the amount of radiation absorbed in the time unit. It is then fundamental to continuously monitor the light transmission of each crystal during the LHC operation.
A laser-based monitoring system, shown schematically in figure 2.16, is designed to inject pulses into each individual crystal to measure the light transmission near the scintillation spectrum peak ($\lambda \approx 440$ nm) and, as

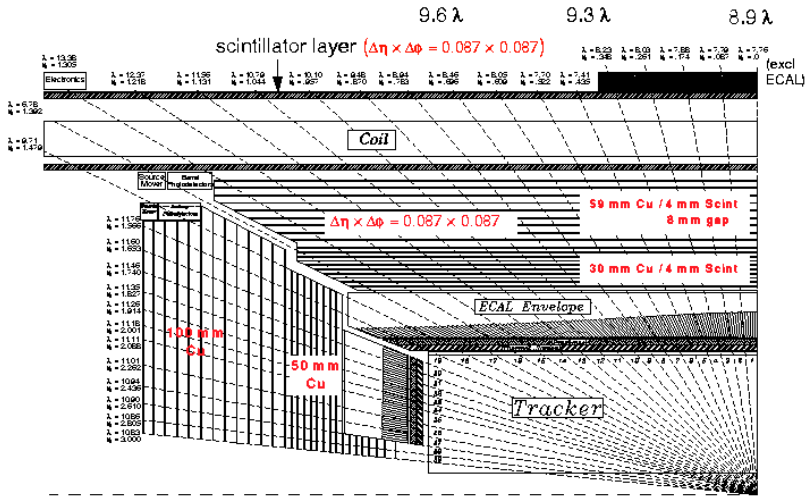

Figure 2.17: Longitudinal representation of the CMS Hadron calorimeter. Dashed lines correspond to a fixed interval of 0.1 in pseudorapidity.

a crosscheck, at a longer wavelength ($\lambda \approx 800$ nm). The intensity of the injected light is monitored by reference PN silicon photodiodes.
Under irradiation, the loss in transparency for the laser light (R) and for the scintillation light (S) are related by a power law (Bonamy, 1998):

$$\frac{S}{S_0} = \left(\frac{R}{R_0}\right)^{\alpha}, \tag{2.6}$$

where R_0 and S_0 are the signal intensity before the irradiation respectively for laser light and scintillation light. It has been shown by specific test beam studies that the coefficient α for the different crystals has the same value within 5%. Since the irradiation damage is small ($< 6\%$) for crystals in the barrel, it is possible to use one single value of α for all the crystals in order to correct the crystal response for the transparency loss. This keeps the contribution to the constant term in the resolution $< 0.3\%$, thus within the design specification.

2.2.4 Hadron Calorimetry

The goal of the hadron calorimeter is to measure the energy and the direction of hadronic jets as well as the missing transverse momentum (CMS Collaboration, 1997b). The detector must therefore fully contain the hadron

shower, have a good transverse granularity and be completely hermetic.
Together with the electromagnetic calorimeter, the hadronic calorimeter also provides help in the identifications of electrons and, being able to detect the passage of a single muon, also assists the muon identification.
The CMS Hadron Calorimeter is a sampling calorimeter with 3.7 mm thick active layers of plastic scintillators alternated with 5 cm thick brass plate absorbers. It consists of two systems (figure 2.17): a central calorimeter (for $|\eta| < 3$), divided into a barrel and two endcaps, and a very forward calorimeter, placed outside the magnet to extend the pseudorapidity coverage to $|\eta| < 5$. The overall thickness varies from 8.9 interaction length in the barrel region up to 10 in the endcaps. A tail catcher composed of scintillators tiles is placed in the barrel region outside the magnet to improve the shower containment.
A lateral granularity of $\Delta\eta \times \Delta\phi = 0.087 \times 0.087$ for $|\eta| < 2$ has been chosen in order to match that of the electromagnetic calorimeter and of the muon chambers, guaranteeing a good di-jet separation and mass resolution.
According to test beam data, the expected energy resolution for single pions interacting in the calorimeter is

$$\frac{\sigma_E}{E} = \frac{94\%}{\sqrt{E}} \oplus 4.5\%, \tag{2.7}$$

and for pions interacting in ECAL and HCAL is

$$\frac{\sigma_E}{E} = \frac{83\%}{\sqrt{E}} \oplus 4.5\%. \tag{2.8}$$

where the energy is measured in GeV. A sizeable degradation of the resolution is expected at $|\eta| = 1.4$, where the presence of services and cables makes higher the inactive material.
The performance of the very forward calorimeter is expected to be

$$\frac{\sigma_E}{E_{\text{hadr}}} = \frac{172\%}{\sqrt{E_{\text{hadr}}}} \oplus 9\% \qquad \frac{\sigma_E}{E_{\text{em}}} = \frac{100\%}{\sqrt{E_{\text{em}}}} \oplus 5\%, \tag{2.9}$$

for hadrons and electrons respectively (the energy is measured in GeV).
After the energy calibration, the energy resolution for jets can be parametrized as

$$\frac{\sigma_E}{E_T} = \frac{1.18(1.56)}{\sqrt{E_T}} + 0.07(0.05), \tag{2.10}$$

where the numbers refer to the high (low) luminosity phase.
The angular resolution on the jet direction is expected to be less than 0.04 for jets with transverse energy greater than 50 GeV.

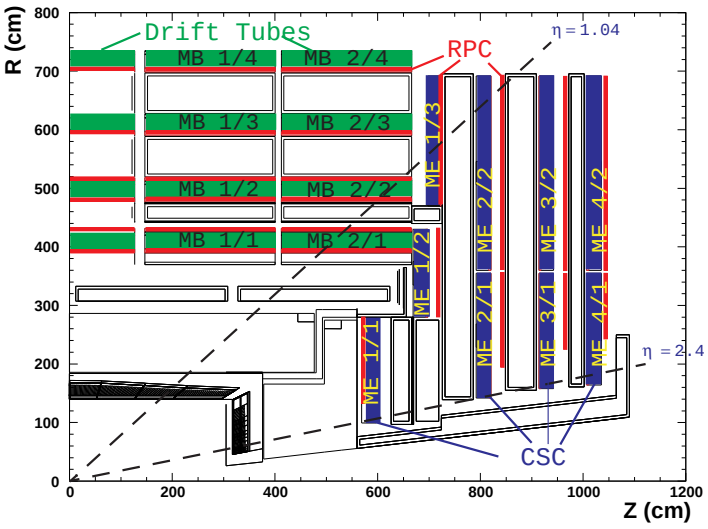

Figure 2.18: Longitudinal representation of a quarter of the CMS muon system. Drift tubes, resistive plate chambers and cathode strip chambers are visible.

2.2.5 Muons System

The muon system at LHC plays a fundamental role, since most of the physics of the Higgs boson, electroweak and top physics, B-physics as well as most of the extensions of the Standard Model present muons in their final state topology.
The muon system is devoted to mainly three tasks: muon identification, trigger and momentum measurement (CMS Collaboration, 1997c).
Divided into barrel and endcaps detectors covering the pseudorapidity range $|\eta| < 2.4$ (fig. 2.18), is located outside the solenoidal magnet integrated with the return yoke of the magnet. Four active detectors layers using different technologies are interleaved with the iron plates of the yoke, which have a total thickness before the last muon station of about 16 interaction lengths.

Each detection unit of the barrel region ($|\eta| < 1.3$), where the particle rate is expected to be < 10 Hz cm^{-2}, consists in 12 layers of drift tubes (DT) providing a precise track measurement in the bending plane. Their maximum drift time is about 400 ns, with a time resolution of 5 ns. The overall spatial resolution in the R-ϕ plane is expected to be of 100 μm (250 μm on the single layer) and of 150 μm in the beam axis direction.

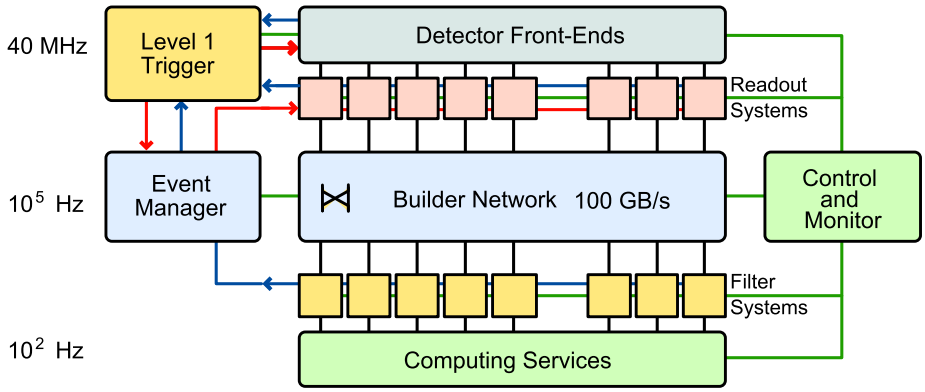

Figure 2.19: Data flow in the CMS trigger and data acquisition system. The time axis goes from upside down.

For the endcaps ($0.9 < |\eta| < 2.4$), cathode strip chambers (CSC) have been adopted, because they can sustain higher particle fluxes (~ 100 kHz cm^{-2}) and stronger and non uniform magnetic field (variations from 1 T to 3 T are expected). With the exception of the first layer, which has three detectors rings, the other layers are made out of an inner disk of 18 detectors and an outer disk of 36 detectors, covering 20° and 10° in ϕ respectively.

In addition, single gap Resistive Plate Chambers (RPC) are used both in the barrel and endcap regions to complement the precision tracking offered by DT's and CSC's with fast detectors with an excellent time resolution (~ 1 ns). They are used both for triggering purposes and for an unambiguous identification of the bunch crossing.

The muon track reconstruction efficiency provided by the stand-alone muon system is higher than 90% for 10 GeV/c muons in the entire pseudorapidity range.
The performance for momentum measurements strongly depends on the pseudorapidity, since for $|\eta| > 1.5$ the tracks exit the solenoid and are hence less bent. For 10 GeV/c muons the resolution varies from 7% in the barrel to 24% at $|\eta| = 2.4$. For very high tranverse momenta (~ 1 TeV/c) this range shifts to 20%-40%. Combining the muon system measurement with the tracker information, the global momentum resolution improves to 1%-1.5% for 10 GeV/c muons and to 6%-17% for 1 TeV/c tracks.

Trigger	Threshold [GeV]	Rate [Hz]	Cumul. Rate [Hz]
$1e$, $2e$	26, 14.5	34	34
1γ, 2γ	80, $40 \oplus 25$	9	43
1μ, 2μ	19, 7	29	72
1τ, 2τ	86, 59	4	76
jet $\oplus$ E_T^{miss}	$180 \oplus 123$	5	81
1-, 3-, 4-jets	657, 247, 113	9	90
$\ell \oplus$ jet	$19 \oplus 52$	1	90
incl. b-jet	237	5	95
Calibration/other	-	10	105

Table 2.4: Example of a HLT trigger table assuming low luminosity running conditions for LHC. The total output rate is ~ 100 Hz.

2.2.6 The Trigger and Data Acquisition System

At the LHC nominal luminosity of 10^{34} cm^{-2} s^{-1}, an average number of ~ 20 interactions per bunch crossing is expected every 25 ns, leading to a total event rate of 10^9 Hz. The full data streaming of the CMS detector ($\mathcal{O}(10^8)$ channels) is estimated to be 1 Mbyte per zero-suppressed event, resulting in 100 Tbyte of data per second. The challenge of the CMS trigger system ((CMS Collaboration, 2000b), (CMS Collaboration, 2002)) is to preserve the most interesting physics signals while reducing the event rate down to ~ 100 Hz equivalent to ~ 100 Mbyte/s, or the maximum acceptable limit of the Data Acquisition System (DAQ). This reduction of 7 order of magnitude is achieved in two steps (figure 2.19).

A First Level trigger (or Level-1 trigger, L1) is accomplished with a custom-designed electronic system which reduces the event rate to 100 kHz by means of a pipelined system with latency time of 3.2 μs. It is composed of a Calorimeter Trigger, collecting information from ECAL and HCAL, and a Muon Trigger, collecting information from the Muon System, combined in a Global Trigger. The Level-1 trigger tables are focused on the detection of high energy leptons as well as high transverse energy jets and of large missing energy in the event.

The L1-accepted events are transferred to a computer farm based on commercial processors and performing as High-Level-Trigger (HLT). The HLT complete several steps of filtering in a fully software way, by running fast

versions of the off-line reconstruction algorithms which impose progressively more severe requirements on the reconstructed objects. The total HLT latency time of 1 s is achieved using a single processor farm with standard CPU's (about 1000). The reduction rate of three order of magnitude by the HLT is foreseen.
Table 2.4 shows the applied thresholds for the L1 and HLT trigger assuming a low luminosity scenario for LHC.

Bibliography

Bonamy, P., *et al.*. (1998), *The ECAL Calibration: Use of the Light Monitoring System*, CMS NOTE 1998/013.

CMS Collaboration (1997a), *CMS ECAL Technical Design Report*, CERN/LHCC 97-33.

CMS Collaboration (1997b), *CMS: The Hadron Calorimeter Project Technical Design Report*, CERN/LHCC 97-31.

CMS Collaboration (1997c), *CMS: The Muon Project Technical Design Report*, CERN/LHCC 97-32.

CMS Collaboration (1997d), *The Magnet Project: Technical Design Report*, CERN/LHCC 97-10.

CMS Collaboration (1998), *CMS: The Tracker Project Technical Design Report*, CERN/LHCC 98-06.

CMS Collaboration (2000a), *Addendum to the CMS Tracker TDR*, CERN/LHCC 2000-016.

CMS Collaboration (2000b), *CMS: The Trigger and Data Acquisition Project, Volume I: The Level-1 Trigger Technical Design Report*, CERN/LHCC 2000-38.

CMS Collaboration (2002), *CMS: The Trigger and Data Acquisition Project, Volume II: Data Acquisition and High-Level Trigger Technical Design Report*, CERN/LHCC 2002-26.

Eidelman, S., Hayes, K. *et al.* (2004), *Review of Particle Physics*, Physics Letters B, **vol. 592**, pp. 1+, URL `http://pdg.lbl.gov`.

Chapter 3

ECAL: Test Beam Studies

During the last three years some modules and one complete supermodule of the CMS ECAL barrel calorimeter have been exposed to a test beam in the North Area of the SPS at CERN. The main motivations were in particular:

- the validation of both physics performance and technical aspects (e.g. cooling system, high and low voltage system) of the largest "self-consistent" unit of the detector, the supermodule;
- the test of the intercalibration procedure over a large amount of crystals;
- the test of the detector radiation damage and recovering when subjected to LHC-like environmental conditions;
- the optimization of the energy resolution through the pulse shape reconstruction and the study of the electronic noise;
- the collection of a reliable set of data to fine-tune the ECAL response in the CMS full Monte Carlo simulation.

In order to investigate all the aspects, the ECAL supermodules have been exposed to electrons and pions of different energies (from $\mathcal{O}(1$ GeV) to $\mathcal{O}(10^2$ GeV)), constantly monitoring the detector response with a laser monitoring system.
In the following the emphasis will be put on the major aspects where a personal contribution has been brought.

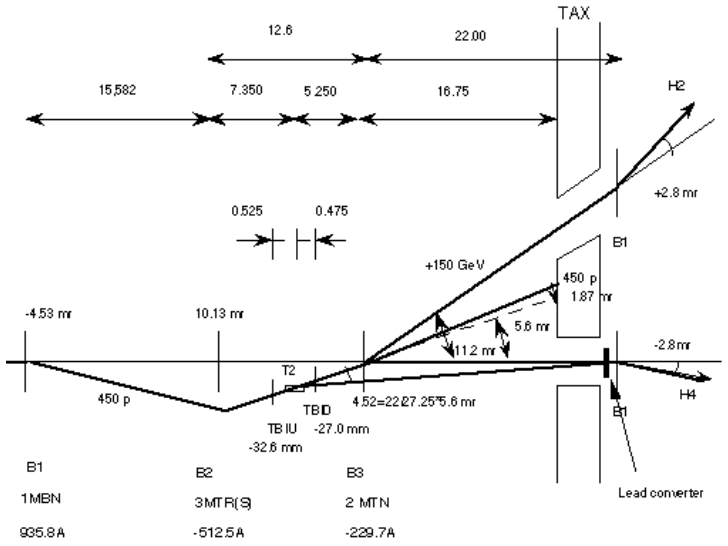

(a)

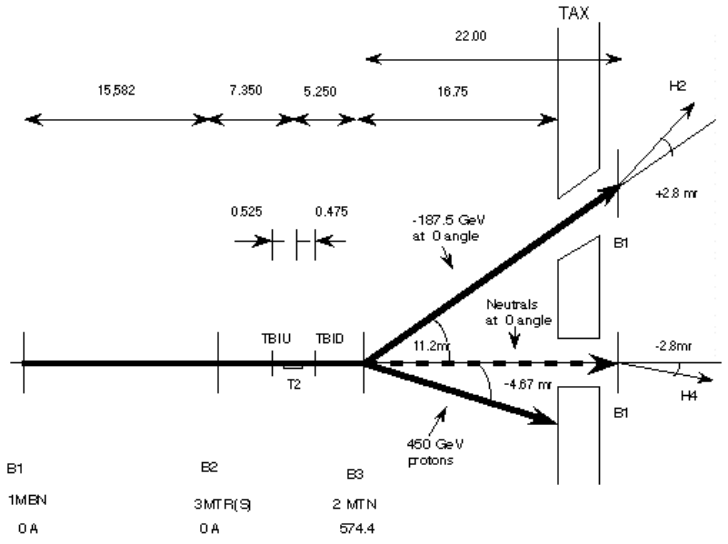

(b)

Figure 3.1: H4 extraction line configuration. Photons from neutral pions decay in the target are taken at a production angle of -4.52 mr and converted to electrons or positrons in a lead converter placed in between the TAX and B1 of the beam line. In (a) the basic configuration to obtain electrons in H4 is shown while in (b) a variant to obtain high fluxes and electrons at high energies ($280 - 300$ GeV) is displayed.

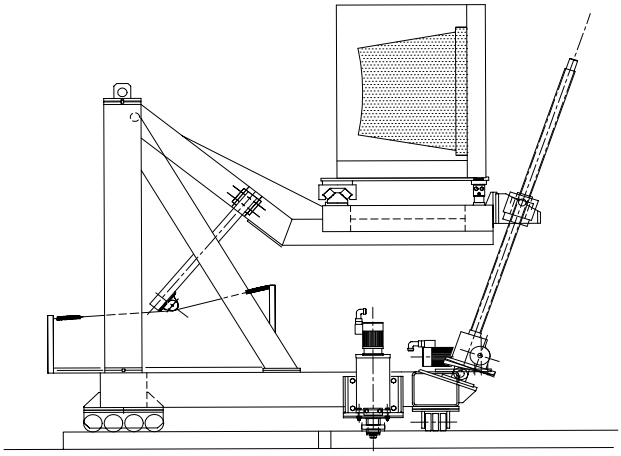

Figure 3.2: ECAL test beam rotating table.

3.1 Experimental Setup

The test beam area is located along the H4 extraction line of the SPS accelerator. A primary proton beam with maximum energy of 450 GeV and intensity of 10^{12} particles per bunch is used to produce secondary and tertiary beams via interactions on fixed targets. Different configurations of the interaction region (figure 3.1) allow to produce and select electrons with fixed momentum between 20 and ~ 300 GeV/c, with a momentum bite defined by the collimator slits of 0.02% (0.24%) for electrons with momentum of 100 GeV/c (280 GeV/c).

The ECAL supermodules are mounted on a rotating table that can be displaced along both the η and ϕ directions, to place each of the crystals on the beam line reproducing the final CMS geometry with respect to the interaction point (fig. 3.2).
Since the 2003 test beam, the beam position is measured by mean of a hodoscope system with a resolution of 150 μm in the x-y coordinates of the plain perpendicular to the beam axis. This allows the extrapolation of the beam impact point to the crystals surface.
The trigger to the data acquisition is provided by six scintillator plates placed along the beam line. Since the trigger is asynchronous with respect to the clock distributed to the electronics readout, the time shift between the trigger and the electronic clock is also recorded, using TDC with around 1 ns of precision.

The supermodules are equipped with the final designed cooling system, which stabilizes the crystals temperature within 0.05 °C, and are placed in a 18 °C termalized environment reproducing the final CMS thermal conditions.
In order to constantly monitor the light transmission of the crystals, which is dependent on the radiation dose rate absorbed by a crystal and on its temperature, an optical monitoring system is used. In its final setup it consists of two laser sources operating at four different wavelengths (440, 495, 706, 796 nm) and of an optical fibre distribution system which injects the light into all crystals. Fluctuations in the laser light intensity are monitored by groups of 200 crystals with PN diodes, each of them guaranteeing a stability within 0.15% in the normalization of the laser pulse.
Four different typologies of runs are taken by the Data Acquisition (DAQ) system:

- *electron beam runs*: around 40 burst of $2 \cdot 10^3$ events triggered inside 20×20 mm^2 centered on the crystal;
- *pedestal runs*: 500 events randomly triggered for each ADC gain of the readout chips;
- *laser runs*: 1500 events taken with different laser wavelength;
- *temperature runs*: 200 events from the temperature probes placed on the rear face of the crystals, one each 10 crystals

In addition, in order to study the crystal behaviour after irradiation, 10 h with dose rates from 0.2 to 0.4 Gy/h (larger than the upper limit expected in the barrel at high luminosity) are taken followed by a comparable recovery period. Regarding to the test beam, it should be noticed that the final CMS setup will be different in the following points:

- presence of the 4 T magnetic field;
- presence of the tracking material in front of the calorimeter;
- synchronous trigger (given by the beam crossing) for the electronic readout with respect to the signal development.

In the final CMS setup, therefore, the electron reconstruction will be more complicated. Firstly non negligible effects (such as bremsstrahlung radiation) due to the material in front of the calorimeter will take place. Then the strong magnetic field will imply additional difficulties in the complete

recollection of the electron energy. On the other hand, the trigger stability will avoid electronic effects related to the jitter of the signal sampling start with respect to the signal shape.

3.2 Test Beam Results

The results obtained by the test beams and not discussed in the rest of the chapter can be shortly summarized as follows (see for example (CMS ECAL Collaboration, 2005)).

Cooling System

The behaviour of the crystals has been studied while the temperature of the setup was changing from 18 to 19 °C. The relative variation of the response of the crystals (due to variation both in the light yield collection and in the gain of the APD) has been measured to be $(-3.82 \pm 0.08)\%/°C$, where the error represents the systematic uncertainty, while the spread among the channels has been found to be $0.4\%/°C$.
By monitoring the crystal response to the laser light it is possible to measure the variation of the APD gain only, since the temperature do not affect the transparency of the crystals. The relative variation have been measured to be $(-2.06 \pm 0.04)\%/°C$, where the error represents the systematic uncertainty, while the spread among the channels has been found to be $0.07\%/°C$.
Additional tests have been performed to measure the temperature variation of the setup due to the electronics power dissipation. It has been possible to put an upper limit of 0.056 °C on the increase of the temperature expected when the electronics is on.
On the basis of this conservative upper limit and on the measured effects of temperature variation on the response it is possible to conclude that the contribution to the constant term of the energy resolution of the calorimeter due to thermal fluctuations is negligible (below 0.2%) even without temperature corrections.

High Voltage Stability and Low Voltage Regulation

The gain M of the APD shows a dependence on the bias voltage of $1/MdM/dV = 3.2\%/V$ at the nominal APD gain ($M = 50$). This implies that a stability in the power supply system better than 30 mV has to be achieved in order to give a constant term to the resolution of the calorimeter smaller than 0.1%. The test beam setup was such to permanently monitor

the high voltage supply of the 200 APDs. The stability of the voltage bias has been measured to be within 20 mV, fulfilling the requirements.

The supply voltage of the readout electronics is 2.5 V and is provided by a custom-made electronic card. Due to the change in the electronics to adopt the 0.25 μm CMOS rad-hard technology, the card developed for the previous version of the electronics was modified and successfully employed to power the new readout electronics.

Monitoring System

The variation of light transmission of the crystals due to the crystals irradiation has been monitored with a laser monitoring system. The relation between the variation of the response to the laser light (R/R_0) and to electrons (S/S_0) can be modeled by the power law $S/S_0 = (R/R_0)^{\alpha}$ (see section 2.2.3). All the crystals exposed to radiation tests ($\mathcal{O}(50)$) have shown a value for α consistent with 1.6. The dispersion of the values is about 6.1%. This means that a single α value could be used for all the crystals, allowing to correct the calibration coefficients with a precision of 0.4%.

Intercalibration

In order to intercalibrate the calorimeter *in situ* to obtain the designed energy resolution, a preliminary set of intercalibration coefficient for the crystals must be determined. The optimal way to intercalibrate the crystals is measuring their response to an electron beam: the intercalibration constant is given by the peak of the energy distribution normalized to a reference crystal (precision $< 1\%$). Due to time constraints on the detector commissioning, this method cannot be applied to all the crystals of the calorimeter. However, a different set of intercalibration constants can be determined from laboratory measurements of the crystal light yields with a ^{60}Co source. In this case the coefficients are obtained normalizing the light yield of each crystal to a reference one (precision $< 4\%$).
During the test beams, the intercalibration procedure with electrons has been made robust and checked against possible bias and systematic uncertainties. Moreover, the comparison between the electron and light yield methods has shown that the last one can provide a set of intercalibration constants which have a sufficient precision to be used as a starting point for intercalibration *in situ*.

3.3 Studies on the Amplitude Reconstruction

3.3.1 Noise Monitoring

In order for the calorimeter to have the energy resolution required by the $H \to \gamma\gamma$ physics benchmark channel, the noise contribution must be kept below 180 MeV. Accurate noise studies of the full electronic readout chain are thus needed.
During the 2003 test beam the old designed Floating Point Pre-Amplifier (FPPA) chip in the electronic chain was replaced with a new conceived Multi-Gain Pre-Amplifier (MGPA) 0.25 μm CMOS chip, offering a better performance with a large reduction of the power consumption and production costs. Data taken with the two different electronic chips have been analyzed.
The studies have been performed mainly with the aim of developing a tool able to identify and promptly point out possible noise problems during the data taking. For the first time in 2003 the test beam online monitoring has been enriched with a Data Validation architecture ((Organtini *et al.*, 2005)) capable of processing the raw data just after their acquisition, identify potential problems and immediately notify run coordinators and shifters. The flexibility of this architecture is guaranteed by separating the data validation in different tasks accordingly to the so called Mediator-Observer Pattern provided by an object oriented programming language: a *Mediator* is able to detect *Events* coming from different *Sensors* (each of them is a validation task) and to dispatch them to *Solutions* in order to take the appropriate action once a problem is detected.

The noise analysis is based on a decomposition of the electronic signals in the Fourier domain. The Maximum Entropy Method (MEM) has been applied to have the best estimate of the power spectral density of a signal. This approach is justified by the Parseval's theorem, stating that the total power of a signal is the same whether it is computed in the time domain ($h \equiv h(t)$) or in the frequency domain ($H \equiv H(f)$):

$$\mathcal{P} \equiv \int_{-\infty}^{+\infty} dt\ |h(t)|^2 = \int_{-\infty}^{+\infty} df\ |H(f)|^2. \tag{3.1}$$

Here the interest is on the power spectral density of a signal, that is the power contained in the frequency interval between f and $f + df$, and it will be evaluated considering the signal $H(f)$ in the frequency domain.

It can be shown (see for example (Press *et al.*, 1992)) that $H(f)$ can be approximate with a Laurent expansion in the complex plain so that its power spectral density is given by

$$\mathcal{P}(f) \approx \frac{a_0}{\left|1 + \sum_{k=1}^{M} a_k z^k\right|^2} \quad , \quad z \equiv e^{2\pi i f \Delta}, \tag{3.2}$$

where Δ is the sampling interval and the coefficients a_i can be determined using the Fast Fourier Transform (FFT) algorithm.
The advantage of this technique compared to the estimate of $\mathcal{P}(f)$ directly from the FFT is the continuous approximation of the power spectrum, which can be evaluated for each value of f, independently of the function digitization (which only determine the quality of the approximation). The form of the approximation 3.2 is naturally sensitive to peaks in the frequency spectrum, which are well represented by poles in the denominator (from which the alternative name "all-poles" for the method).

An example of power spectrum obtained on a pedestal run (with FPPA electronics) is shown in figure 3.3 for each of the different electronic gains. We can see a large contribution to the spectrum coming from noise at low frequencies. During the data taking the source of this noise was found to be a non perfect Faraday shielding of the electronics and corrected.

To have an empirical estimation of the sensitivity of the method a coherent noise with a frequency of 6 MHz has been artificially added to the pedestal runs, as it is shown in figure 3.4(a). The resulting power spectrum is shown by the left curve of figure 3.4(b), where a clear peak is visible at the expected frequency.

3.3.2 Amplitude Reconstruction in the Time Domain

The amplitude reconstruction method from the individual samples of the digitized signals is based on a digital filtering technique which is optimal in presence of white noise. The best estimate $\mathcal{A}$ of the signal amplitude

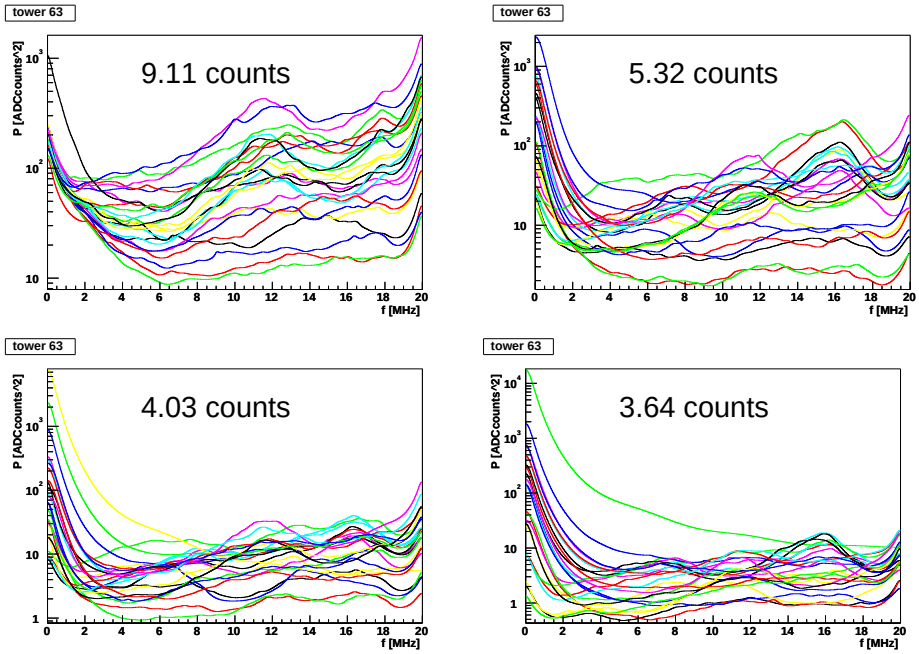

Figure 3.3: Power spectral densities for the crystals of the tower 63 computed from a pedestal run after baseline subtraction. The four plots corresponds to the four gain of the FPPA chip. A substantial contribution to the total noise coming from low frequencies is present.

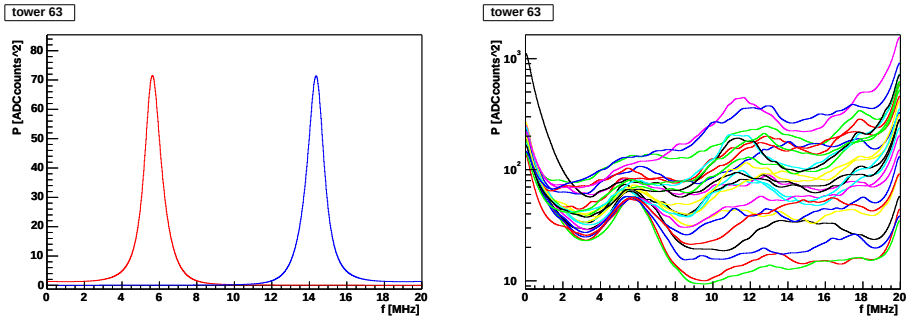

(a) (b)

Figure 3.4: Example of detection of artificial noise using the MEM algorithm. A noise with frequency of 6 MHz (left curve of the plot on the left) has been added to a pedestal run: the noise is clearly detected at the correct frequency and with the correct power (right plot).

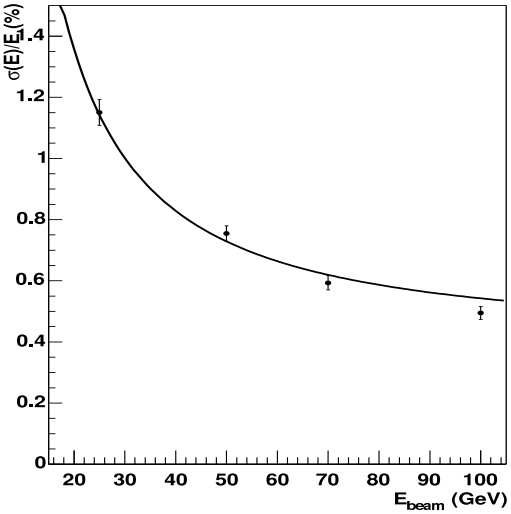

Figure 3.5: Resolution obtained by the weigths method applied to the sum of the energy in an array of 5×5 crystals centered on the beam impact point.

is extracted using a linear weighting of the individual samples, each one carrying information on the amplitude:

$$\mathcal{A} = \sum_i w_i S_i, \tag{3.3}$$

where the S_i are the digitized samples. In general the single i-th sample can be modeled by

$$S_i = A f_i + b_i + p, \tag{3.4}$$

where A is the true amplitude, f_i the expected pulse height for the sample, b_i the background coming from the electronic noise and p a constant baseline or pedestal. The requirement for $\mathcal{A}$ to be an unbiased estimate is ensured imposing the constraints

$$\sum_i w_i f_i = 1 \quad , \quad \sum_i w_i = 0, \tag{3.5}$$

where in particular the latter automatically subtract the baseline from the samples event-by-event.

The set of optimal weights is obtained by minimizing the variance of the reconstructed amplitude. Under the assumption that the time of the maximum response is stable for a given channel, as foreseen in CMS, one set of weights is enough for each single crystal. With the additional assumption that a set of channels has similar properties, the same set of weights can be used for all these channels.
The expected pulse heights f_i are computed using an analytic function to describe the signal:

$$f(t) = \begin{cases} \left(\frac{t-(t_{\max}-t_{\text{rise}})}{t}\right)^{\alpha} \cdot e^{-\alpha\frac{t-t_{\max}}{t_{\text{rise}}}} & , \quad t > t_{\max}-t_{\text{rise}} \\ 0 & , \quad \text{otherwise.} \end{cases} \tag{3.6}$$

While other approaches to evaluate f_i are possible, namely the use of mean reference pulses empirically estimated, the analytic function has the advantage of being simple and not involving a large set of histograms.

The energy resolution obtained by this method is shown in figure 3.5 (Dewhirst and Bruneliere, 2004) as a function of the beam energy. The energy is reconstructed summing up a cluster of 3×3 crystals centered on the one with maximum energy. The events are triggered inside a 4×4 mm^2 area centered on the point of maximum response in the hit crystal. The calibration to convert the ADC counts information in GeV has already been determined. The resolution is obtained as a Gaussian fit between $\pm 2\sigma$ of the mean and the momentum spread $\sigma(p)/p$ is subtracted from this value.

3.3.3 Amplitude Reconstruction in Case of Saturated Signals

The front-end electronics readout for ECAL uses Multiple Gain Pre-Amplifier (MGPA) chip feeding a multi-channel ADC chip to extract the signal. The MGPA consists of a low-noise pre-amplifier stage followed by three gain amplifiers (with nominal gains 1, 6, 12) and feeds a custom designed 12-bit/40MHz ADC that selects the optimal gain (i.e. the highest non-saturated one) by integrated digital selection logic.

The MGPA dynamic range saturates for signals corresponding to $\sim$ 1.67 TeV (3.5 TeV), given the dynamic range of the MGPA corresponding to a charge of 60pC for the barrel and 16pC for the endcaps, an average

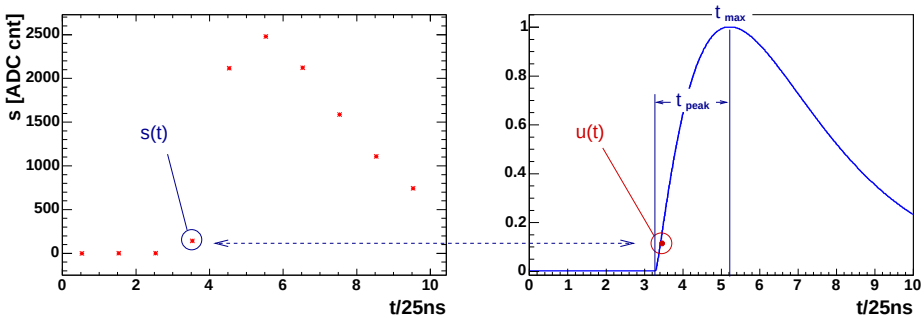

Figure 3.6: Example of signal digitization (on the left) and known shape of the MGPA (on the right). The ratio $s(t)/u(t)$ gives an estimation of the signal amplitude.

crystal light-yield of 4.5 photo-electrons/MeV and the nominal APD (VPT) gain.

This effect concerns for example physics beyond the Standard Model, where resonant states can decay into very high energetic photons or electrons which deposit in a single crystal of the calorimeter an amount of energy greater than the saturation threshold.

In analogy with the standard amplitude reconstruction method that uses a weighted sum to estimate the signal amplitude, it is possible to use one sample $s(t)$ on the signal rise before the saturation occurs to estimate the amplitude, thus using only one single weight w.
To determine w it is not recommended to use the analytic description of the pulse shape, as it is done in the standard reconstruction case, since it gives only an approximate description of the signal rise. An empirical approach has been adopted, estimating a normalized mean pulse shape $u(t)$ from unsaturated signals: w is then given by the reciprocal of $u(t)$ evaluated at the time t at which the sample $s(t)$ was taken. It follows that the amplitude $\mathcal{A}$ is obtained as

$$\mathcal{A} = w \cdot s(t) = \frac{s(t)}{u(t)}. \tag{3.7}$$

If the sample $s(t)$ falls in proximity of an electron gain switch, problems related to instability or non linearity in the electronics can arise. In order to avoid this, it is enough to fix the phase between trigger and data acquisition in such a way that the signal is always sampled just above 1/6 of its

amplitude. Using this sagacity, in case of saturation the used sample could not be taken at any gain different from 1, thus never falling in a gain switch region.
The precision of this method is mainly affected by the systematic uncertainties related to the estimation of $u(t)$ and by the jitter δt on the sampling start time, which directly causes an indetermination on the sampling time t. The latter, in particular, is expected to give a contribution σ_j to the method precision proportional to the derivative of the signal shape:

$$\sigma_j = \left| \mathcal{A} \frac{\partial s(t)}{\partial t} \right| \delta t = \left| \mathcal{A} u'(t) \right| \delta t. \tag{3.8}$$

Taking the analytic form of the signal shape as

$$f(t) = \mathcal{A} \left(\frac{t - (t_{\max} - t_{\text{peak}})}{t_{\text{peak}}} \right)^{\alpha} \cdot e^{-\alpha \frac{t - t\max}{t_{\text{peak}}}}, \tag{3.9}$$

where $t_{\max}$ is the time at which $f(t)$ is maximum and t_{peak} is the signal rise time (figure 3.6), one obtains

$$\frac{\sigma_j(t)}{\mathcal{A}} = \left(\frac{\alpha t_{\text{peak}}}{t - (t_{\max} - t_{\text{peak}})} - \frac{\alpha}{t_{\text{peak}}} \right) \delta t. \tag{3.10}$$

To study the performances of the method, unsaturated signals from 2005 test beam data have been used. The signal amplitude has been assumed exactly known event-by-event from the official reconstruction method.
We remind that in the test beam setup the signal development is asynchronous with respect to the ADC clock, the time shift for each event being recorded with a TDC of around 1 ns precision: this is the largely dominant effect entering in σ_j and affecting the method precision.

Figure 3.7 shows the precision of the method in the amplitude determination when samples falling in different time frames are used. The saturation energy for the sample $s(t)$ is shown in figure 3.8 for different time frames.

A fit of the precision curve considering the contribution σ_j of equation 3.8 and a constant term σ_s corresponding to systematics in the reference shape determination gives as results for δt a value of ~ 2 ns, in qualitative agreement with what is expected, and a value for σ_s of $\sim 1\%$.

Further checks have been carried out to investigate the existence of a bias in the amplitude estimation or a dependence from the beam energy: as shown in figures 3.9 and 3.10, systematic effects on the amplitude estimation are within the method precision and no energy dependence is visible.

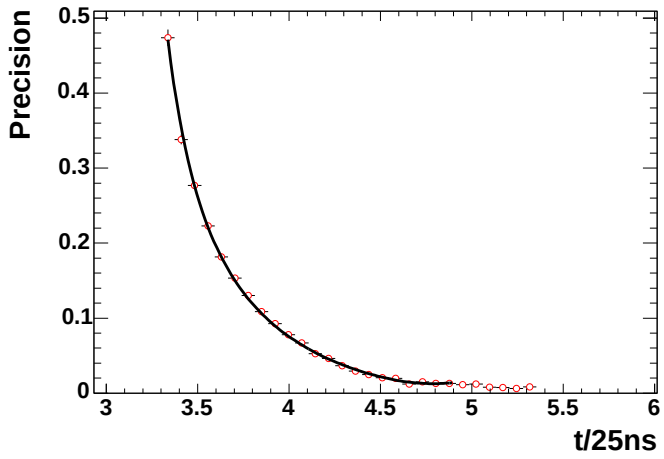

Figure 3.7: Precision of the method as a function of the time frame used in the amplitude estimation. The curve is fitted with the precision predicted assuming a jitter on the sampling time and a constant systematic coming from the knowledge of the reference shape. The grey curve is the signal shape, to guide the eye in viewing which time frame of the signal rise was used for the amplitude determination.

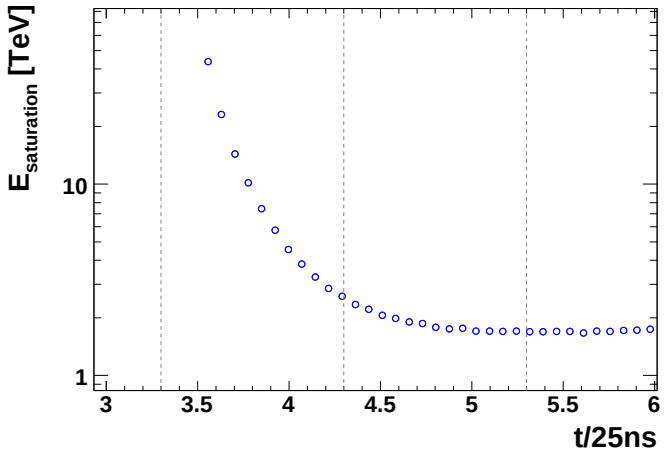

Figure 3.8: Saturation energy for samples falling in different time frames.

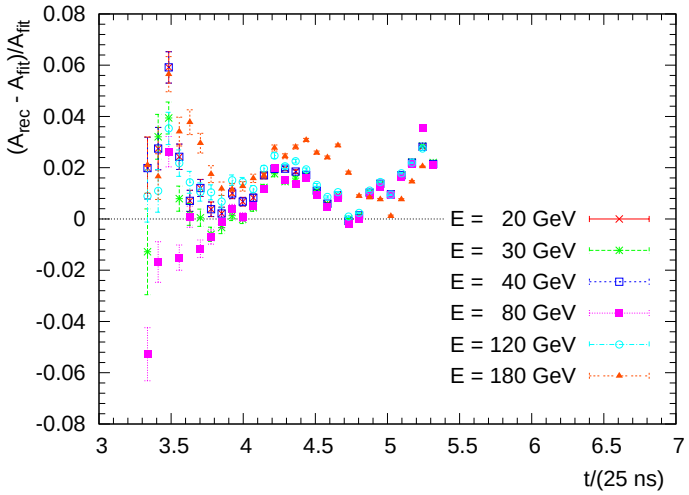

Figure 3.9: Mean of the method resolution. The systematic related to the reference pulse shape is kept within the method precision.

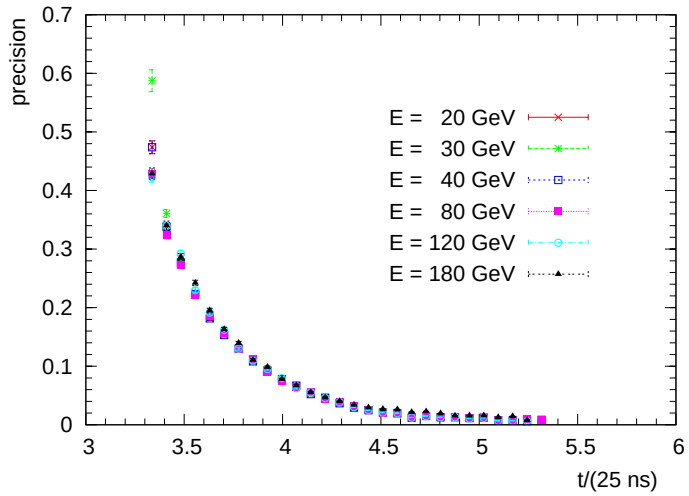

Figure 3.10: Method precision evaluated using pulses from electron beams at different energies. No energy dependence on the results is visible.

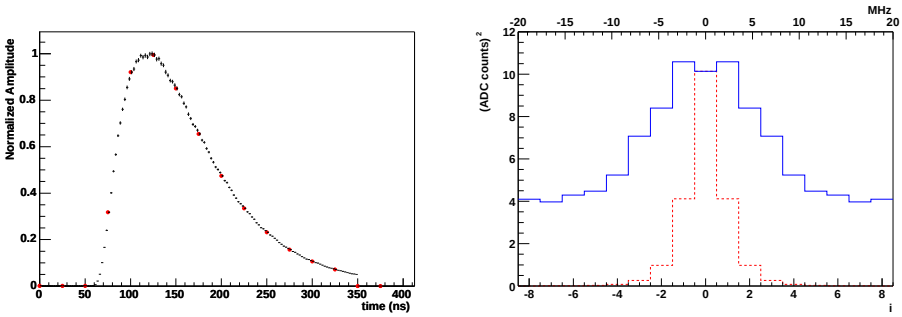

Figure 3.11: *Left*: Average pulse shape as defined in the text. The sampler at small t_{TDC} shift are marked with a red dot. *Right*: Estimated spectral power density with MGPA electronics (continuous line). The spectral power density of the average signal normalized to $i = 0$ is shown for comparison (dashed line). The index i labels the discrete frequencies defined as $f_i = 2f_c i/N$, where f_c is the Nyquist frequency and N the total number of samples.

3.3.4 Amplitude Reconstruction in the Frequency Domain

An alternative approach to the amplitude reconstruction was attempted in the analysis of 2003 test beam data, motivated by the observation of a substantial non white noise in the data. The noise problem was later cured with a more careful grounding and shielding of the new electronics cards based on the 0.25 μm CMOS technology (MGPA chip). An account of the method is given here just for the record.

Using the theory of matched filters (Papoulis, 1962) in presence of a noise spectral power density $\mathcal{N}(\omega)$, an optimal estimate of the signal amplitude can be obtained as:

$$\mathcal{A} = \sum_i \frac{u^*(\omega_i) S(\omega_i)}{\mathcal{N}(\omega_i)} e^{-i\omega_i t_{TDC}}, \tag{3.11}$$

where the sum is over the frequency bins, $u(\omega_i)$ represents the Discrete Fourier Transform (DFT) of an average pulse of unit amplitude, $S(\omega_i)$ is the DFT of the signal recorded. The last term accounts for the phase shift between $u(\omega_i)$, which has been defined with a null offset with respect to the ADC clock and $S(\omega_i)$ which is sampled with an offset t_{TDC}, measuring the delay between the ADC clock and the actual trigger signal. Here both the signal and the reference pulse are always intended after pedestal subtraction.

An empirical approach has been adopted to estimate the weights $u^*(\omega_i)/\mathcal{N}(\omega_i)$. The spectral power density of the noise has been obtained from a pedestal run. For the sake of simplicity, in the amplitude estimates the spectral power density has been assumed to be independent of the channel and of the channel gain. Both these assumptions are only approximately true. The average signal $u(t)$ has been obtained using 100 GeV electron events in one reference crystal and selecting only events in a small acceptance window of 2 mm in x and y around the point where the maximum deposition of energy in that crystal was observed. Only the events with $t_{TDC} < 2.5$ ns, i.e. with little shift with respect to the ADC clock, have been selected, thus giving a good estimate of the average pulse shape for $t_{TDC} = 0$. The results of these two operations are summarized in figure 3.11.

At a somewhat more technical level, the method has been implemented by adopting a Fast Fourier Transform (FFT) algorithm, which requires 2^n samples, where n is a positive integer. The total number of samples has been increased to 16 by numerical extension of the exponential tail of the signal according to

$$s(t_i) = \frac{s^2(t_{i-2})}{s(t_{i-4})} \qquad\qquad i = 15, 16. \tag{3.12}$$

Notwithstanding this sagacity, the baseline level is never fully restored at the end of the sixteenth sample. This brings spurious (high) frequencies into the game, which have been trimmed by multiplying each sample i by an analytic function gently vanishing at the edges of the sampling window:

$$f(i) = \exp\left(-\left(\frac{i-7}{5.5}\right)^{10}\right). \tag{3.13}$$

Pedestal and electron beam run analysis

For the reconstruction of the total energy deposited by high energy electrons in the calorimeter, a matrix of at least 3x3 crystals need to be considered. Indeed, for an electron impinging upon the center of one crystal only about 75% on average of its energy is dissipated whithin the same crystal. In this analysis, the following definition has been adopted:

$$E_{3\times 3} = \sum_{i=-1}^{i=+1} \sum_{j=-1}^{j=+1} a_{ij}\mathcal{A}_{ij} \tag{3.14}$$

where i, j give the relative position of the crystal with reference to the central one, $\mathcal{A}_{ij}$ are the signal amplitudes reconstructed in each individual

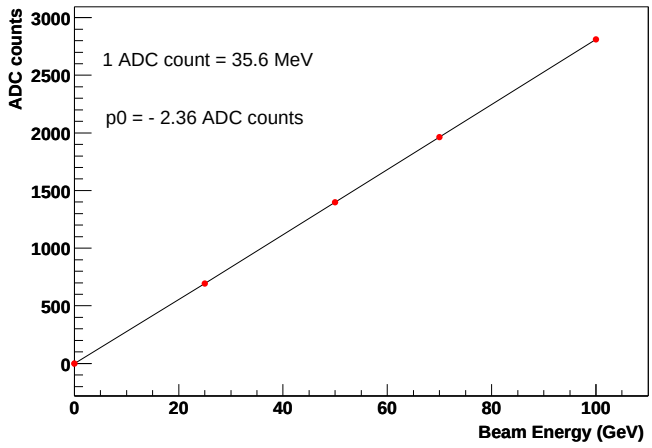

Figure 3.12: ADC channel to energy conversion for a 3x3 matrix of crystals in the ECAL barrel equipped with MGPA electronics.

crystal and a_{ij} are intercalibration coefficients which account for the different response of the channels. The latter coefficients have been taken from the study reported in (Franzoni *et al.*, 2004) based on standard methods for pulse height reconstruction. Events have been retained in the analysis only if the estimated impact point of the electron on the crystal was within ± 5 mm around the point where the maximum response from the central crystal is observed

Figure 3.12 shows the ADC to energy conversion curve for a 3x3 matrix of crystals in the ECAL barrel, including a pedestal run where a null amplitude is correctly reconstructed by the method. The slope of the curve gives a conversion factor of 35.6 MeV/channel.

By applying this channel to energy conversion, the noise level in each single channel can be estimated from the RMS of the amplitude reconstructed in pedestal runs (fig. 3.13-left). This is on average about 50 MeV. In the same figure, the contributions to the amplitude fluctuations of the lowest frequency bin ($\omega_i = 0$) and of all the other bins are also shown separately. Noteworthily, the lowest frequency bin accounts for most of the amplitude fluctuations, its importance being enhanced by the weights of the matched filter. Possible residual baseline fluctuations contribute to this bin. Figure 3.13-right shows the signal amplitude obtained after summation over a 3x3 matrix of crystals. We observe a noise of around 170 MeV, not inconsistent with stochastic noise in the different channels and well in agreement with the target resolution of the ECAL calorimeter.

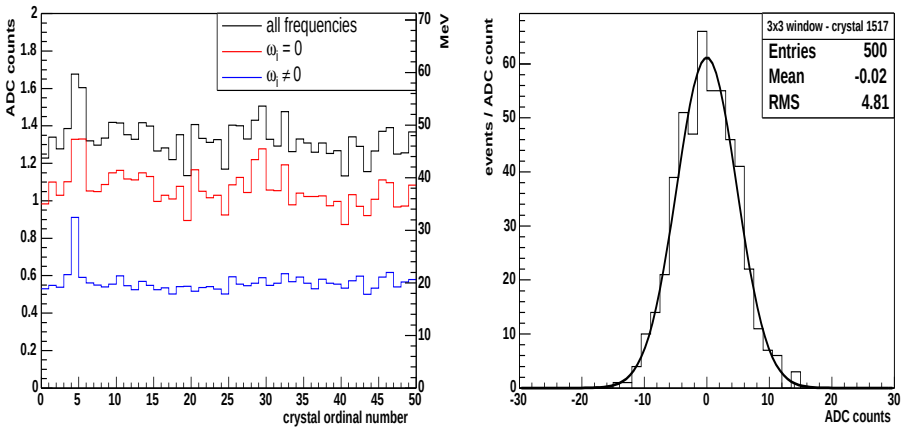

Figure 3.13: *Left:* Single channel RMS of the amplitude reconstructed in a pedestal run for all the crystals of two towers. The total RMS and the separate contributions of the lowest frequency bin ($\omega_i = 0$) and of all the other frequency bins are also displayed. *Right:* Signal amplitude after summation over a 3x3 matrix of crystals in a pedestal run.

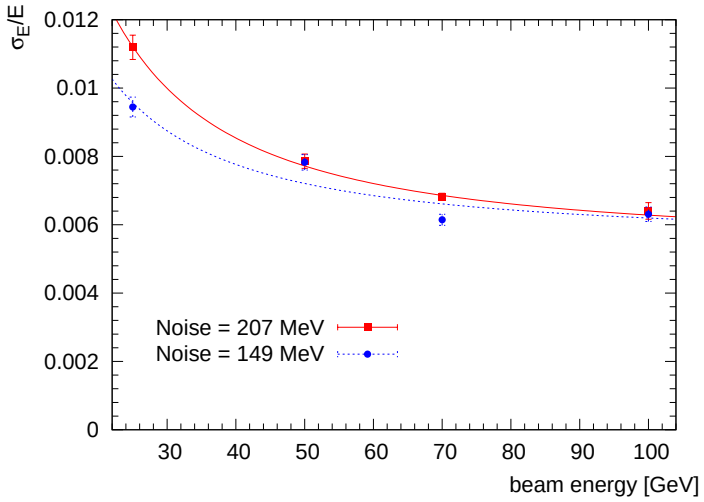

Figure 3.14: Energy resolution σ_E/E as a function of the beam energy for a 3x3 matrix of crystals. The results obtained with the method working in the frequency domain (blue dots) and with the standard amplitude reconstruction method in the time domain (red dots) implemented in the H4ANA package (h4a, 2003) are shown. A predictive curve for the energy resolution dependence on the beam energy (see text) is also displayed.

Finally, figure 3.14 shows the energy resolution σ_E/E as a function of the beam energy for a 3x3 matrix of crystals. A fit to the data point was performed assuming three contributions to the energy resolution: a stochastic term (fixed to 2.5% at 1 GeV), a constant term and a noise term. The latter is found to be consistent with the noise estimate from the pedestal runs. In the same figure, the resolution obtained from the standard amplitude reconstruction method in the time domain (implemented in the H4ANA package (Paganini and van Vulpen, 2004)) is also shown. The comparison between the two curves shows a slightly better performance for the amplitude reconstruction in the frequency domain.

3.4 Conclusions

After an overview of the results achieved with test beam analysis, studies of the electronic noise in the calorimeter readout and of the amplitude reconstruction of the signal acquired from the calorimeter were presented in detail.
For the first aspect, a procedure to evaluate the spectral power density of the signals has been determined using the Maximum Entropy method. This method has the advantage of approximating continuously the noise spectral power density, with respect to other conventional techniques that give only discrete information related to the number of samples of the digitized signal.
The amplitude reconstruction studies have been concentrated on cases where the electronic signals are saturated. The method developed is based on the use of the non-saturated samples on the signal rise, and has shown the possibility to reach precision at the percent level for energies up to several TeV.
An additional method of amplitude reconstruction in case of non-white noise in the electronic readout has also been proposed. The method operates in the frequency domain of the signal and performs comparably to the amplitude reconstruction method by optimal weighting in the time domain. In the limit of white noise the two methods are expected to give the same performance, but the latter enables for dynamical pedestal subtraction in a more natural way and is thus to be preferred.

Bibliography

(2003), *The H4 Analysis Framework*, htpp://cms-project-h4-testbeam-2003.web.cern.ch/cms-project-h4-testbeam-2003.

CMS ECAL Collaboration (2005), *Results of the First Performance Tests of the CMS Electromagnetic Calorimeter*, CMS NOTE 2005/020.

Dewhirst, G. and Bruneliere, R. (2004), *Energy Resolution of the CMS ECAL Barrel Super-Module Using MGPA Electronics*, CMS NOTE 2004/004.

Franzoni, G., Ghezzi, A., Govoni, P. and Rovelli, C. (2004), *Intercalibration for CMS ECAL at 2003 H4 Testbeam*, CMS NOTE 2004/046.

Organtini, G., di Biagio, A. and Maggiori, M. (2005), *Data Validation Software Architecture during the CMS ECAL Test Beam*, CMS NOTE 2003/044.

Paganini, P. and van Vulpen, I. (2004), *Pulse amplitude reconstruction in the CMS ECAL using the Weights Method*, CMS NOTE 2004/025.

Papoulis, A. (1962), *Fourier Integral and Its Applications*, McGraw-Hill Education.

Press, W. H., Teukolsky, S. A., Vetterling, W. T. and Flannery, B. P. (1992), *Numerical Recipes in C – Second Edition*, Cambridge University Press.

Chapter 4

Electron Reconstruction in CMS

The study of the electron reconstruction inside the CMS detector is motivated by the analysis of the Higgs decay channel $H \rightarrow ZZ^{(*)} \rightarrow 4e$, the golden channel for the discovery of a light Higgs boson in addition to $H \rightarrow \gamma\gamma$. The electrons from the two Z decay have a p_T spectrum which varies from $\mathcal{O}(1\ \mathrm{GeV}/c)$ up to $\mathcal{O}(10^2\ \mathrm{GeV}/c)$, depending on the Higgs mass (see chapter 5 for a detailed discussion). In particular, in the low mass region one of the Z is produced off mass shell and the reconstruction efficiency of its two soft electrons becomes crucial. Furthermore, the optimization of the detector resolution exploiting at best tracking and calorimetry measurements is fundamental not only for the Higgs mass peak observation but also for the determination of the Higgs boson properties (e.g. mass, width, CP quantum numbers, couplings to weak bosons and to leptons), which relies on the study of its final decay products. The study and the understanding of the electron behaviour inside the calorimeter is therefore essential to reach the CMS physics goals and obtain the best performance from the detector.

The studies presented here are performed using the full simulation of the CMS detector (ORCA, 2004). They make use of Monte Carlo quantities as well as physical observables, in order to fully address the issue of electrons reconstruction and measurement and identifying the strategies that can be adopted to extract the best measurement for electrons. Motivated by the study of the Higgs decay channel $H \rightarrow ZZ^{(*)} \rightarrow 4e$, the focus will be on electrons in the low p_T range.

Dealing with bremsstrahlung is the hardest challenge to face in CMS. A classification of the electron's "quality", from the "golden" case to the most

problematic one is proposed and class-specific procedures to fix the scale of the electron energy measurement are outlined.
The combination of tracking and calorimetry information is then analyzed to define the best estimator for the electron quadri-momentum at the interaction point.

The complete detector description takes into account active volumes as well as mechanical support structures, electronics (readout and cables) and cooling systems. Technical details related to the CMS detector simulation and reconstruction framework can be found in (ORCA, 2004).
Back-to-back electrons of different energies (between 5 and 100 GeV) with flat distribution in $\eta \in (-2.7, 2.7)$ and $\varphi \in (0, 2\pi)$ have been simulated without additional pile-up events.
The collision point is simulated by adding a Gaussian smearing to the ideal vertex position with a sigma of $\sigma_z = 53$ mm along the z coordinate, coincident with the beam axis, and $\sigma_x = \sigma_y = 15$ μm in the transverse x-y plane, as expected from the LHC beam stability.

4.1 Electron Propagation towards the Calorimeter

The considerable amount of material budget in front of the electromagnetic calorimeter makes the bremsstrahlung the most important effect by which propagating electrons are affected.

As shown in figures 4.1, the probability for an electron to loose all of its energy by bremsstrahlung emission is almost equal to the probability of reaching integrally the calorimeter (neglecting losses below the Monte Carlo threshold of 30 MeV for bremsstrahlung emission). The cumulative distributions show that $\sim 25\%$ of electrons have already lost more than 70% of their energy at the half way point of their path towards ECAL. This fraction grows to 35% at the end of their trajectories. From the point of view of the reconstruction algorithms, the recollection of this energy is a key issue.

As a crosscheck, the X/X_0 traversed by the electrons is estimated by assuming that all the energy loss is due to bremsstrahlung emission and that the tracker is a uniform medium. From the formula

$$E(x) = E_0 e^{-x/X_0}, \tag{4.1}$$

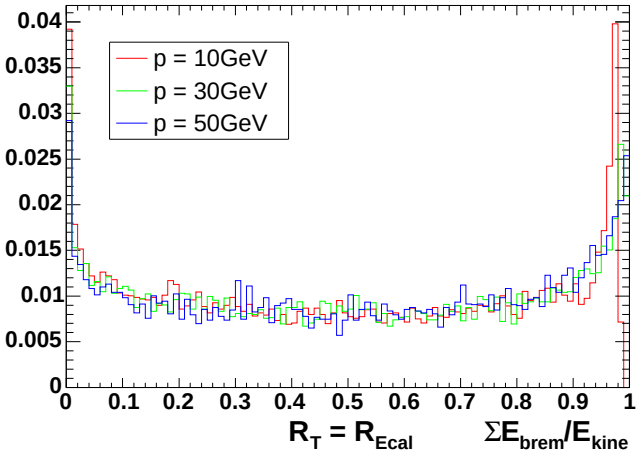

Figure 4.1: Fraction of energy emitted by bremsstrahlung as a function of $\sum E_{\text{brem}}/E_{\text{kine}}$ of their initial energy E_{kine}. The emission inside a transverse radius equal to the calorimeter radius is considered. The curve is computed for electrons with different fixed momentum. The probability of no bremsstrahlung emission above the Monte Carlo threshold (30 MeV) is the same as the probability of emission of all the initial energy.

where E_0 is the initial energy, for a given $\overline{x}$ it is possible to compute x/X_0 by evaluating

$$\frac{\overline{x}}{X_0} \approx -\log \frac{\langle E(\overline{x})\rangle}{E_0}, \tag{4.2}$$

where $\langle E(\overline{x})\rangle$ is the mean energy after a length $\overline{x}$ is traversed.
The results are shown in figure 4.2 and follow the material budget distribution, as expected.

In order to better investigate the energy loss and to disentangle the different effects involved in the energy measurement (due, for example, to reconstruction problems and true energy losses), a modification has been implemented in the Monte Carlo simulation. This modification allows to keep track of the true amount of energy reaching the calorimeter and to have the possibility of comparing the ECAL measurement to what it can actually measure. The modification consists in recording energy, position and particle type of all of the particles impinging on the ECAL crystals, taking care to avoid double counting of energy deposition (due e.g. to particle generation inside a crystal, particle crossing more than one crystal etc.) and to consider only

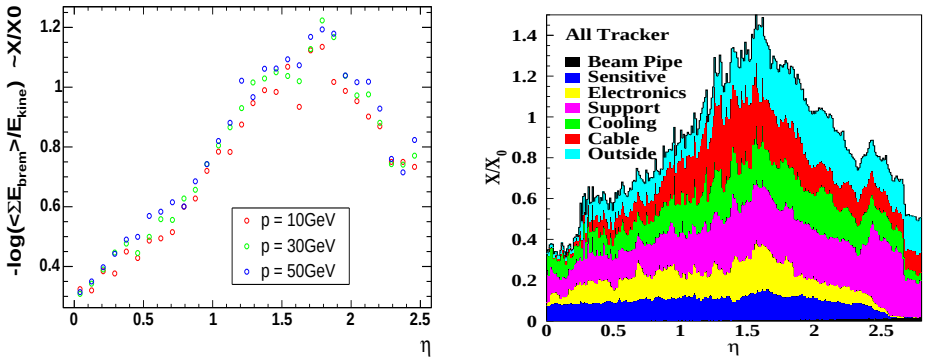

Figure 4.2: Material budget distribution computed using bremsstrahlung emission as an approximation of the total energy loss. The good agreement between the estimated (*left*) and true (*right*) X/X_0 is remarkable.

the ECAL active volume. The assumption is made that a particle impinging on the calorimeter deposits there all its energy. This is a satisfactory approximation of the particles behaviour in this context.

An example of the impact points on the barrel calorimeter exhibiting the shape of the front face of the crystals as a result of the impact points distribution is shown in figure 4.3. The modified Monte Carlo is the only tool in CMS providing an information on the energy flux at the ECAL front face. This information also provide the possibility to perform detailed studies of the effect of dead regions between modules ("cracks") in the calorimeter with the full detector simulation.
A typical energy deposition for an electron in the different crystals with the contributions from the different particles impinging on the crystals is also shown (figure 4.4).
By examining the true energy reaching ECAL for electrons in the barrel (figure 4.5), it emerges that a substantial amount of energy is lost in front of the calorimeter, up to 7% in the region of high η, where the material budget distribution becomes maximal.

It is important at this stage to look at the energy loss by the electrons along their trajectory towards the calorimeter. The processes characterizing

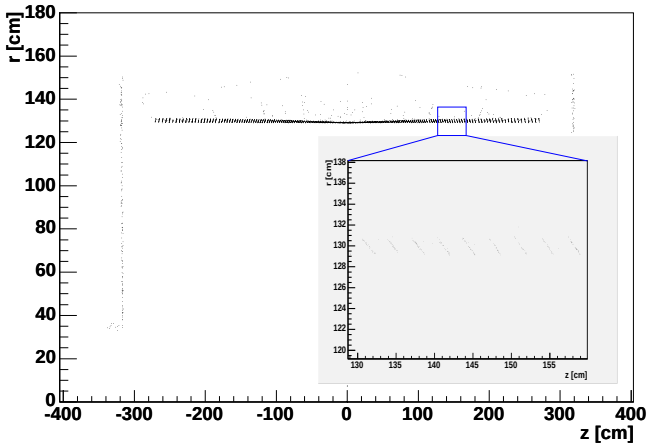

(a)

Figure 4.3: Longitudinal view of the electron impact points on the crystals of the calorimeter (barrel and endcap regions). The distribution has been obtained with the modified Monte Carlo simulation. In the magnified region, the shape of the crystal front faces emerges as the results of the impact point distribution. Impact point of particles traversing the crystals after being in a crack are also evident.

the energy loss are, in different proportions, the dE/dx in the tracker material, the bremsstrahlung emission and the synchrotron emission. However, while the energy lost in dE/dx and synchrotron radiation is totally lost, the bremsstrahlung radiation can be partly recollected if the photons reach ECAL and the reconstruction algorithms perform well. Bremsstrahlung can contribute to energy completely lost if, for example, the emitted photons convert in the tracker material and the electron-positron couple remain trapped in the magnetic field. Recovering the largest possible part of the energy loss is a challenge for the ECAL reconstruction algorithms, which have to extract all the possible information from the energy deposition in the calorimeter. Indeed, the energy lost can be evaluated only from "indirect" observables, mainly involving the tracker detector, where all the effects take place.

The a priori assumption that bremsstrahlung emission can be associated with a greater amount of energy lost is then not motivated, since, in case of a complete energy recollection, hard emitted photons can lead to very good measurements of the initial electrons energy. However, due to the stochastic nature of the bremsstrahlung effect, large fluctuations in the quality of the

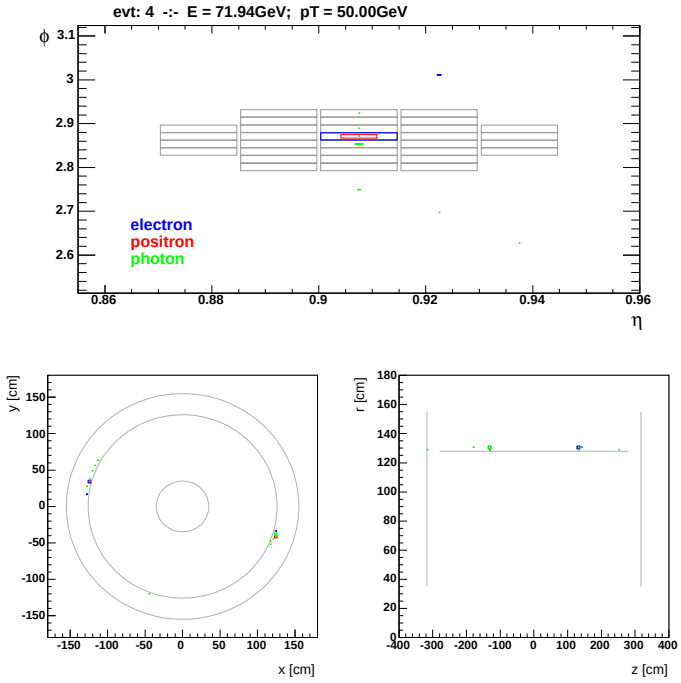

(a)

Figure 4.4: Example of particles impact point on the calorimeter in a η-φ plane for a back-to-back pair of electrons of $p_T = 50$ GeV/c. In the top figure the coloured box represents the different particles impinging on the crystals and the box size is proportional to the particle energy. The grey box corresponds to the clusterization of the energy obtained by the Hybrid algorithm, which is described in section 4.2. The bottom figures represent respectively the transverse and longitudinal view of the detector.

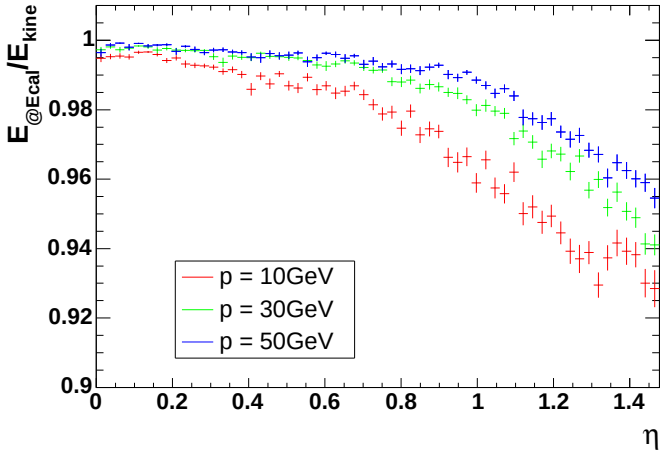

Figure 4.5: Distribution of the true energy reaching the calorimeter normalized to the initial electron energy, for different electron momenta. Losses up to 7% of the original momentum at vertex are observed.

energy measurement are introduced.

This section is concluded by showing the correlation existing between the energy lost and the total length of charged tracks. The latter quantity has been defined by looking at the Monte Carlo truth as the sum of the track length of all the charged tracks belonging to the original electron, that is the sum of the track length of the considered electron and of all the electrons from the conversion of bremsstrahlung photons emitted along the tracks.
The distribution of the average of this quantity versus the pseudorapidity is shown in figure 4.6-left for electrons with transverse momentum between 5 and 50 GeV/c and uniformly distributed in η and φ. In figure 4.6-right the distribution of track length of the charged tracks is shown as a function of the difference between the energy at the calorimeter and the Monte Carlo initial energy. The superimposed red profile clearly shows a direct correlation between these two quantities. The population on the left part of the histogram with a charged track length less than the ECAL radius (130 cm) corresponds to electrons that loose all their energy in bremsstrahlung photons which do not convert in the tracker material. In this case almost no energy is lost and only a very small path is traversed by charged particles. These events will be lost as electron candidate and could be eventually recovered looking for photon candidates in the event.
The correlation between the energy lost and the total tracks length (from

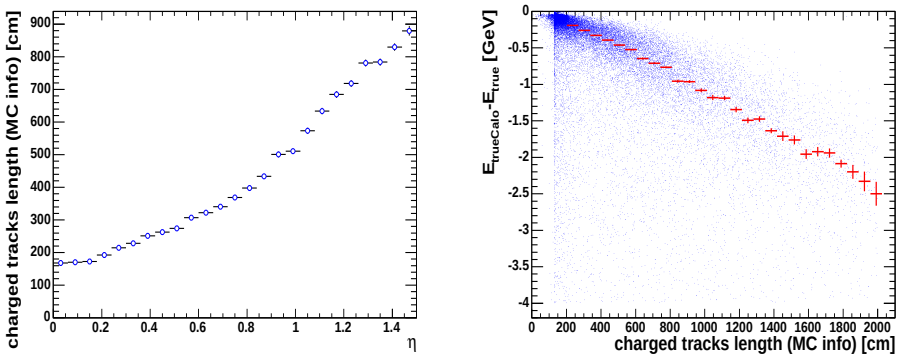

Figure 4.6: *Left*: mean value for the total length of charged tracks defined in the text as a function of the pseudorapidity. *Right*: correlation between the energy lost before reaching ECAL and the total length of charged tracks. The red points on the histogram represent the profile of the distribution.

the Monte Carlo truth) strongly suggests that the tracker could bring very useful information about the electrons' "history" of the propagation towards ECAL.

Since the tracker has the typical X/X_0 of a presampler (but unfortunately is a discrete and low density medium in a high magnetic field), a digital information on the energy loss by electrons can be extracted, by for example counting the number of hits in a cone around the electron track. The result obtained is shown in figure 4.7 for back-to-back electrons with momentum of 30 GeV/c. The number of hits has been computed subtracting from the total number of hits in a cone with $\Delta r \equiv \sqrt{\Delta\varphi^2 + \Delta\eta^2} < 0.15$ the hits recognized to be part of the electron track, applying this way a sort of normalization with respect to the different tracker geometry in η. While it is not possible to apply this simple approach to a full physics event, since hits in the tracker have many different sources, it should be considered as a starting point for more accurate studies involving more advanced searches for secondary tracks and hits. A possibility would be, for example, to look for secondary electron tracks compatible with the hypothesis of the conversion of a photon emitted by the primary electron track.
Further investigation of possible algorithms will clarify the extent to which this unusual way of looking at the tracker as presampler could bring to the improvement of the electron energy measurements. Great care should be paid to the risk of double counting.

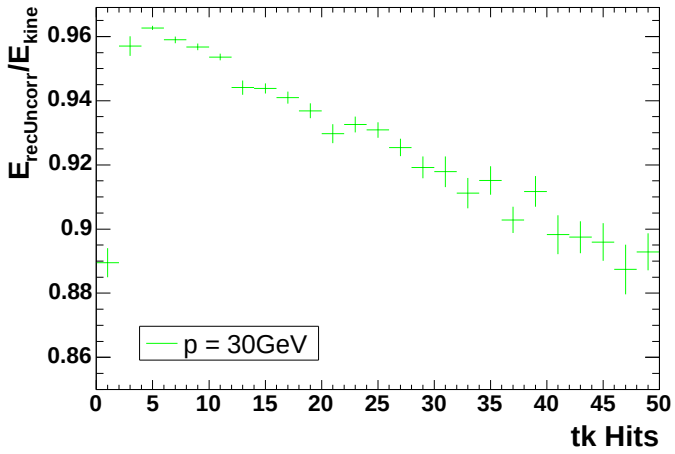

Figure 4.7: Profile histogram showing the dependence of the ratio between the raw reconstructed energy and the true energy from the number of hits in the tracker inside a cone of $\Delta R = 0.15$ around the electron track direction.

4.2 Electron Candidates

The definition of an electron candidate in CMS involve the tracker and the electromagnetic calorimeter at the same time and follow a step procedure similar to the strategy used for the High Level Trigger algorithm. In particular, as represented in figure 4.8, the clustering of the energy deposited in the calorimeter drives the search for pixel hits, which constitute the seed for the reconstruction of an electron track.
In the following a short overview of the different algorithms for the electron reconstruction will be given. For a more detailed description see for example (CMS Collaboration, 2002) and (Adam *et al.*, 2005).

4.2.1 Calorimetric Reconstruction

The energy recollection in the electromagnetic calorimeter can be considered as a pattern recognition procedure applied to the spacial array of the crystal energy deposits. The starting point is the search for local maxima (called seeds) by looking at each single crystal. The seeds are then extended to include the largest possible fraction of the original shower energy, avoiding to collect energy deposited by nearby particles and noise. Two are the method developed for such purpose: the Hybrid algorithm and the Island

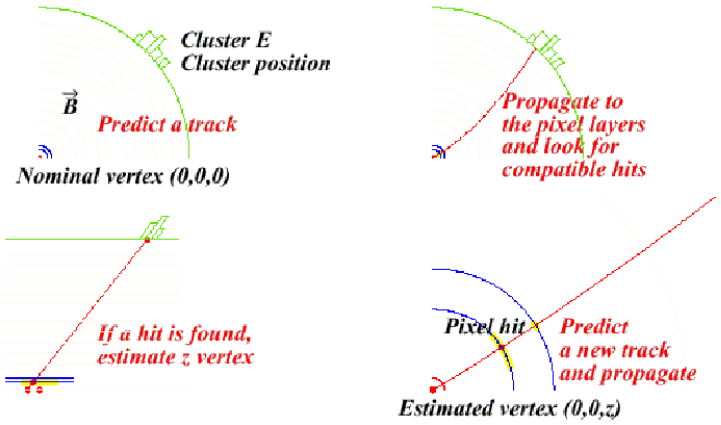

Figure 4.8: Schema of the electron candidate definition, as described in the text.

algorithm.

The Hybrid Algorithm

As shown in figure 4.9(a), the Hybrid algorithm starts from a seed crystal by subsequently adding fixed dominos of three or five crystals (according to an energy threshold on the central crystal of a domino) in η. The collection search for dominos in a window of 10 crystal in ϕ. If any energy deposits above a threshold is found, it is associated to the primary cluster. In this sense the Hybrid algorithm recollects in a single step also the bremsstrahlung clusters.

The Island Algorithm

As sketched in figure 4.9(b), the Island algorithm starts by collecting crystals from the seed crystal, moving in both directions in ϕ until a rise in the energy is found. The algorithm then moves a step in η and performs another search in ϕ. The search in the η direction is stopped when a rise in the energy is found. The algorithm comes back to the original seed position and starts a search in the opposite direction along η.
Once all the clusters have been collected, a step to recover clusters due to the emission of bremsstrahlung photons by the original electron is performed. This consists in associating together two (or more) clusters with the same η and with the same ϕ within a given window to form a so-called supercluster.

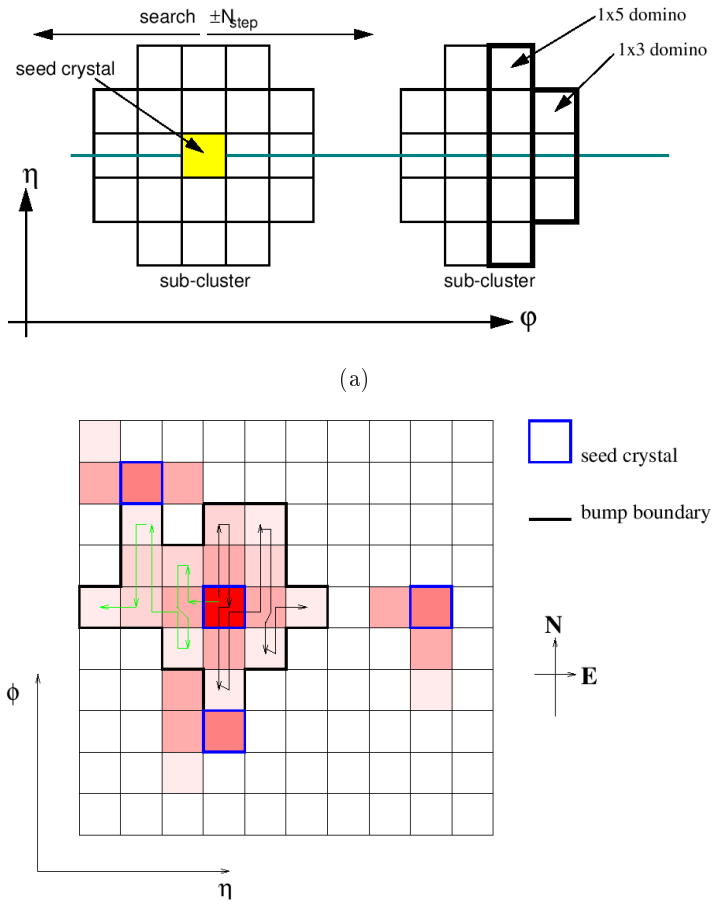

Figure 4.9: Schema of the superclustering algorithms for the electromagnetic calorimeter: (a) hybrid (the default in the barrel) and (b) island (the default in the endcaps).

The Island is the default algorithm for the energy reconstruction in the endcaps.

Optimization for Off-line Reconstruction

A re-tuning of the supercluster building parameters has been performed for the hybrid algorithm to better reconstruct low p_T electrons. The minimal E_T threshold for the basic seed cluster of a supercluster has been lowered from the previous default of $E_T^{\text{seed}} = 4$ GeV down to $E_T^{\text{seed}} = 1$ GeV. This leads to a considerable improvement of the efficiency for reconstructing a supercluster: integrating over the acceptance in η, this efficiency for back-to-back electrons is now greater than 99% for $p_T^e = 7$ GeV/c and $E_T^{\text{seed}} = 1$ GeV, compared to an original efficiency for $E_T^{\text{seed}} = 4$ GeV varying from about 65% for $p_T^e = 7$ GeV/c to about 93% for $p_T^e = 10$ GeV/c.
To better recollect clusters corresponding to bremsstrahlung photons, the value of the ϕ road for the recovering has been increased from 10 to 17 crystals (Baffioni, 2005).

Default Energy Scale Correction

The energy measurement of a supercluster is obtained by simple addition of the deposits measured in the crystals. Even in the areas not covered by the preshower detector, the energy containment of the crystals is not complete. A default re-scaling of the energy is thus applied in the barrel using a parametrization of the energy dependence by the number of crystals in a supercluster. However, this default correction is no longer valid, due to changes both in the material budget description and in the ECAL readout algorithm, and a new method to correct the energy measurement will be largely discussed in the following sections.

4.2.2 Electron GSF Track Reconstruction

Starting from a supercluster in the calorimeter, a prediction on the region where to look for hits in the tracker pixel detector is made, propagating an hypothetical electron (and positron) trajectory with the same transverse momentum as the one measured by ECAL from the supercluster position back to the nominal interaction point. If two consecutive hits in the pixel detector are found, a new seed for an electron (or positron) trajectory is defined.

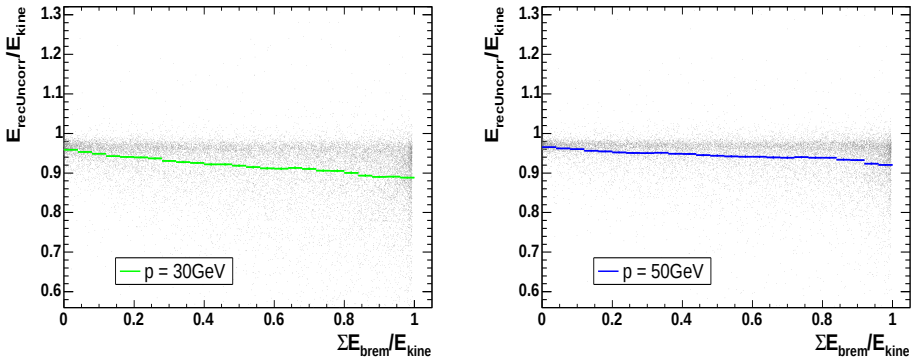

Figure 4.10: Distribution of the raw clusterized energy normalized to the true energy as a function of the fraction of energy emitted by bremsstrahlung. The more the bremsstrahlung effect is important, the more fluctuations in the measurement are introduced. A substantial amount of well measured electrons is still present: the mean of these distributions (continuous coloured curve) is not meaningful.

Starting from the seed, the electron track is built by means of the Gaussian Sum Filter algorithm (GSF). For a detailed description of the method see (Charlot *et al.*, 2005).

The GSF algorithm is based on the search for hit in the tracker under the hypothesis that the track can irradiate bremsstrahlung photons and thus that its curvature radius can vary along the trajectory. The basic principle is to model the bremsstrahlung energy loss distribution due to the particle interaction on the tracker silicon layers by a Gaussian mixture rather than a single Gaussian (as it is instead done by standard Kalman-Filter methods). This allows to follow the track up to the calorimeter and to have a momentum measurement at the beginning and at the end of the electron trajectory, with the possibility of better exploiting the combination of calorimetry and tracking measurements. Standard methods, instead, typically stop the fit of the electron track when a hard bremsstrahlung photon has been emitted and the electron trajectory has suddenly started to bend with a different curvature radius.

4.3 Energy Measurements and Electron Classification

The previous discussion on the bremsstrahlung (4.1) points out that the topology of an electron inside CMS is largely varying because of the large intrinsic fluctuations of the bremsstrahlung effect.
The classification of electrons according to their topology would then be very useful in understanding the quality of their measurements, in trying to distinguish cases in which the energy measurement from the calorimeter is reliable and to separate the tail in the distribution of $E_{\mathrm{recUncorr}}/E_{\mathrm{true}}$ from the bulk of the accurately measured electrons.
The possibility of distinguishing the "goodness" of an electron and to consequently associate an error to its energy measurement will allow to optimally combine calorimetry and tracking information to have the best estimator of the electron quadri-momentum at the interaction point.
To evaluate the quality of the ECAL energy measurement, a criterion based on a continuous estimator is very difficult to find due to the high discontinuity of the main process affecting the electron propagation, the bremsstrahlung radiation. The approach used here has been to divide electrons in a restricted number of classes by applying a set of criteria that follows a precise decision tree. In this section, after some considerations on the energy measurement, the electron classification will be discussed in details.

In the analysis of the quality of energy measurements, effects coming from bremsstrahlung photon emissions and (subsequent) energy lost play a fundamental role. However, as already suggested above, higher bremsstrahlung emission does not imply worse energy measurements. Indeed, electrons loosing almost all of their energy in few bremsstrahlung photons emit very hard photons which can be completely recollected by the clustering algorithms. This is clearly shown in figure 4.10 where the ratio of the reconstructed energy over the true energy at vertex ($E_{\mathrm{recUncorr}}/E_{\mathrm{kine}}$) is plotted as a function of the true fraction of energy emitted by bremsstrahlung. Large fluctuations are introduced in the measurement when the fraction of energy loss is approximately 1, nevertheless a significant population of events for which the ratio $E_{\mathrm{recUncorr}}/E_{\mathrm{kine}}$ is almost 1 is still present.
By examining more closely the energy deposited in the calorimeter, it is possible to separate electrons whose supercluster has only the seed cluster from the cases where also other subclusters (due to bremsstrahlung

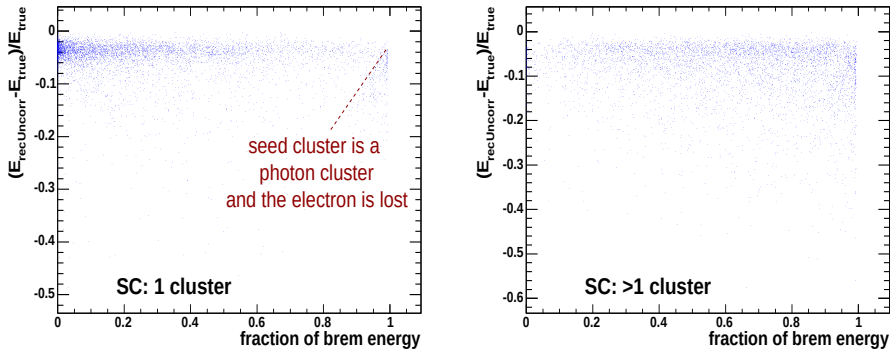

(a) (b)

Figure 4.11: Distribution of the normalized difference between reconstructed and initial electron energy as function of the fraction of energy emitted by bremsstrahlung for electrons with momentum of 30 GeV/c. Electrons with only the seed cluster in the supercluster are shown in (a), events where additional subcluster in the supercluster are shown in (b). This selection can be fruitfully used to detect bremsstrahlung emission using the calorimeter.

photons) are present. This provides an "ECAL-driven" criterion to detect bremsstrahlung photons. The results are in good agreement with the true fraction of emitted energy, as shown in figure 4.11 which refers to electrons with momentum of 30 GeV/c. The left figure shows that it is possible to select electrons with a small fraction of their energy emitted by bremsstrahlung ($\sum E_{\rm brem}/E_{\rm true} \to 0$) by requiring only one cluster in the supercluster. On the other hand, if more than one cluster is found in the supercluster (figure 4.11(b)) the electrons populate the region with higher bremsstrahlung emission. It can also be noticed on figure 4.11(a) a small fraction of events on the right side of the plot. These are examples of cases in which the electron emits a very hard photon (which is well clusterized) at the beginning of its track and either gets lost into the tracker or is too far from the photon cluster to be properly recollected.

Electrons with a momentum of 10 GeV/c exhibit the same effects, with an additional bremsstrahlung recovery problem, clearly demonstrated both by the correlated region in figure 4.12(a) and by the small number of events at high fraction of emitted energy, where the incomplete energy recollection causes a loss in the reconstruction efficiency.

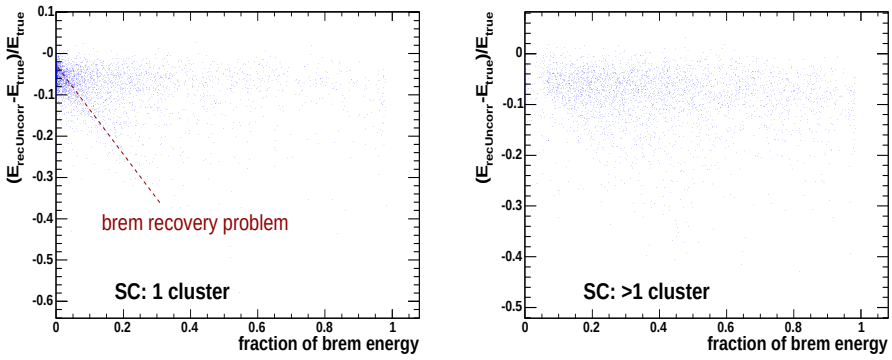

(a) (b)

Figure 4.12: Same distributions as for figure 4.11 but for electrons with a lower momentum ($p = 10$ GeV/c). The linear correlation between the missing energy and the fraction of energy emitted by bremsstrahlung clearly indicates a bremsstrahlung recovery problem.

As demonstrated also by the tail on the left in figure 4.13 this behaviour is typical of low p_T electrons whose bremsstrahlung photons are not hard enough to be clusterized or are too far in φ, due to the total binding of the electron in the magnetic field, to be properly recollected by the algorithms.

Apart from the obvious geometrical criteria (barrel-endcaps separation and fiducial volume), the classification requirements give rise to the following categories:

- "golden" electrons, the closest to the ideal case (negligible bremsstrahlung and almost all the energy reaching ECAL);
- "big brem punch thru", i.e. cases in which the electron radiates almost all of its energy with the emission of typically one very hard bremsstrahlung photon;
- "narrow" electrons, that is neither "golden" nor "big brem punch thru" electrons which still don't show anything but the seed cluster in the supercluster;
- "showering" electrons, the worst ones, where the energy measurement is affected by the emission of several bremsstrahlung photons that possibly convert into electron-positron couples indicating that an early electromagnetic shower has started in the tracker material.

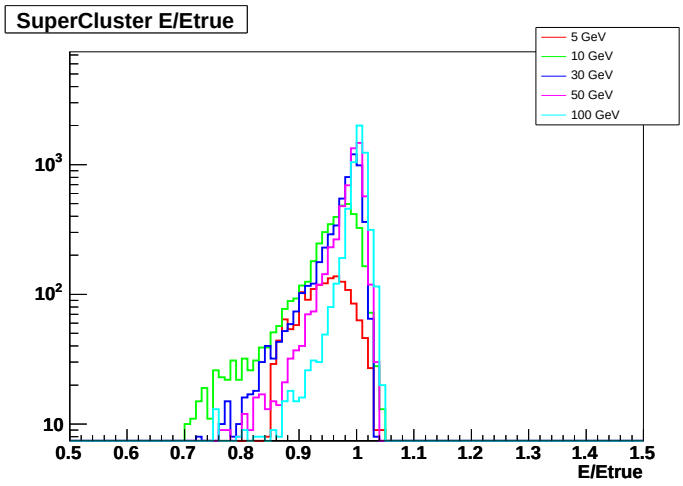

Figure 4.13: Distribution of the supercluster energy normalized to the true energy at vertex for different electron momenta. The energy is rescaled according to the default corrections described in 4.2.

An example of events with electrons belonging to different classes along with a schematic representation of the detector are shown in figure 4.14.

At a more technical level, the decision tree is outlined below. If a criterion is not satisfied, the next one is tried, until every requirements is fulfilled or the last class is reached.

- "golden":
  - a supercluster without identified bremsstrahlung subclusters (i.e. only constituted by the seed cluster only);
  - a GSF track with a bremsstrahlung fraction lower than 0.2, where the bremsstrahlung fraction is defined as the difference between the momentum at vertex and the momentum at last point normalizes to the momentum at vertex;
  - a matching in φ between the supercluster position and the position from the track extrapolated to the calorimeter within 0.15 rad;
  - a ratio between the energy measured with the calorimeter and the momentum measured with the tracker greater than 0.9;
- "big brem punch thru":
  - a supercluster without identified bremsstrahlung subclusters (i.e. constituted by the seed cluster only);

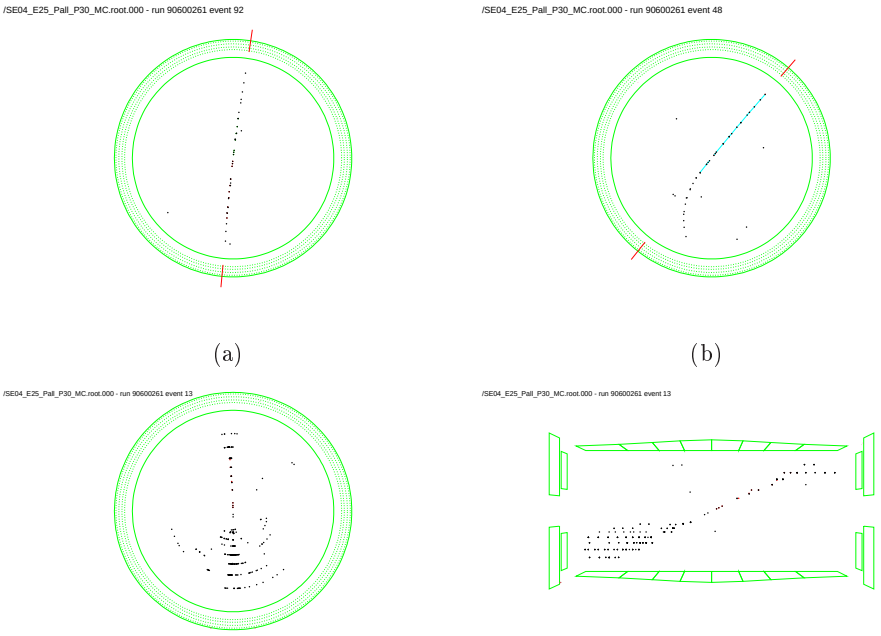

Figure 4.14: Example of events for back-to-back electrons with momentum of 30 GeV/c: a "golden" case with no bremsstrahlung emission and very good calorimetry measurement (a), a case with a very hard emitted photon and no cluster associated to the electrons (which is lost before reaching ECAL) (b), an extreme case with an electrons starting an early shower in the tracker (transverse view (c) and longitudinal view (d)).

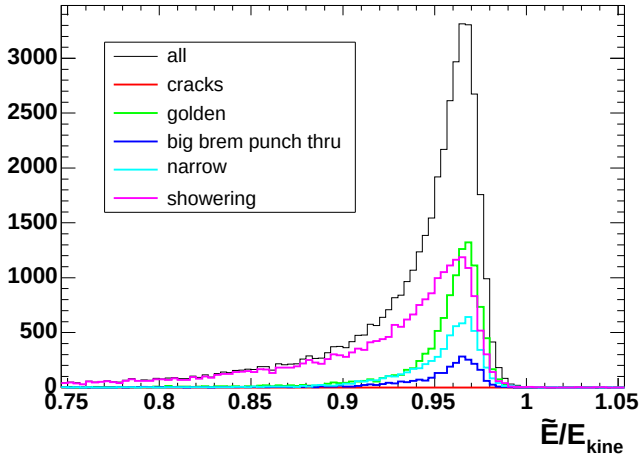

Figure 4.15: Distribution of the raw clusterized energy normalized to the initial energy for electrons of momentum between 5 and 100 GeV/c. As expected the distribution does not peaks at 1 because no correction on the measurement have already been applied at this level.

  - a GSF track with a bremsstrahlung fraction greater than 0.5;
  - a ratio between the energy measured with the calorimeter and the momentum measured with the tracker equal to 1 within 0.1;

- "narrow":
  - a supercluster without identified bremsstrahlung subclusters (i.e. constituted by the seed cluster only);
  - a ratio between the energy measured with the calorimeter and the momentum measured with the tracker equal to 1 within 0.1;

- "showering":
  - electrons that do not fulfil the previous criteria.

The distribution of the ratio between measured energy and true energy is shown in figure 4.15 for the different classes. It is clearly visible that the first three classes are well contained in the bulk of the distribution while the tail falls almost completely in the "showering" electrons category, which will then have a larger error associated to a less precise measurement.

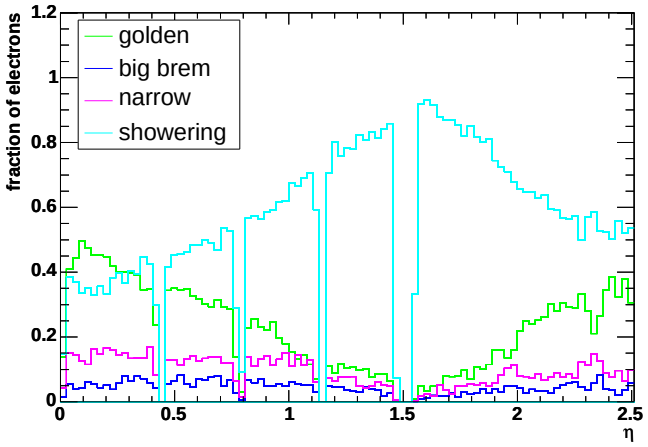

Figure 4.16: Distribution along η of the fraction of electrons falling in the different classes. The shape of (golden) showering electrons is clearly (anti-)correlated to the material budget in front of ECAL.

The η distributions of the fraction of electrons falling in the different classes are shown in figure 4.16. It is clearly visible that the fraction of (golden) showering electrons (inversely) reproduce the distribution of the material budget, having its maximum in the transition region between barrel and endcaps and decreasing at larger η. Big brem punch thru and narrow electrons are nearly constant over the first three modules, with a substantial decrease in the fourth modules and a growth in the endcaps.

To associate an error to the energy measurement, the resolution as a function of the initial electron energy is presented in figure 4.17. As expected the golden electrons show the best resolution, similar to the curve of big brem punch thru and narrow electrons. On the other hand, the large fluctuations affecting showering electrons give bigger contributions for constant and stochastic terms, resulting in a worse energy resolution with respect to the other classes.

4.4 Energy Scale Correction

The standard strategy described in section 4.2 to correct the energy measurements of electrons needs to be revisited, due to the more accurate description of the tracking material (which directly influence the amount bremsstrahlung

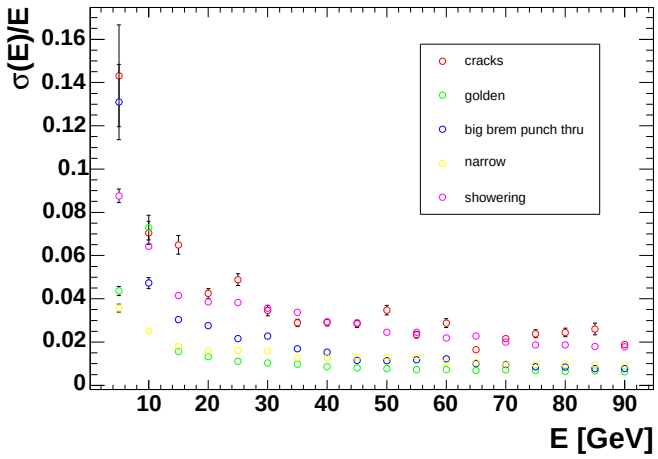

Figure 4.17: Energy resolution for the different electron classes. "Golden", "bib brem" and "narrow" electrons are measured almost with the same resolution, while for "showering" electrons the constant and stochastic terms give a bigger contribution due to larger fluctuations in the energy deposition and recollection.

radiation) and to the changes in the selective readout algorithms of the calorimeter.
In particular, the material budget in front of ECAL has been consistently increased, making the energy measurements at large values of the pseudorapidity much more difficult. Moreover, some of the assumptions made with the previous detector description are no longer valid and need to be reconsidered.

Firstly, the present readout of the crystals in a supercluster takes into account all the channels, while previously only the crystals with a good signal to noise ratio were selected, using a threshold at twice the mean noise level.

An immediate consequence for the default reconstruction algorithm in the ECAL barrel is that the dependence of the quantity $E/E_{\text{true}} - 1$ from the number of crystals N_{cry} in a supercluster is not even continuous anymore (figure 4.18). The discontinuities are due to the discrete nature of the Hybrid clustering, which increases the supercluster dimension either by 2 or 3 crystals at each step, thereby making the energy dependence of N_{cry} much less evident.

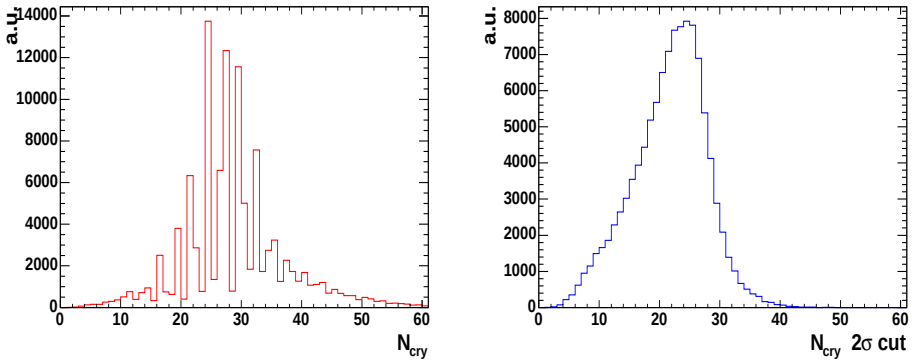

(a) (b)

Figure 4.18: Distribution of the number of crystals in a supercluster for electrons with momentum uniformly distributed between 5 and 100 GeV/c. The patterns related to the clustering algorithm visible in the total number of crystals (a) disappear if a threshold of 2σ on the mean noise level is applied when counting the crystals.

Secondly, even after applying a cutoff to the noise level to count the number of crystals, the relation between $E/E_{\text{true}} - 1$ and N_{cry} is not universal. It indeed shows a clear p_T dependence (figure 4.19(a)) due to the different bremsstrahlung photons recollection at different p_T of the electrons.
However, the dependence of the reconstructed energy on the number of crystals in the seed cluster only is universal, since the seed cluster is not affected by bremsstrahlung recovery effects. Figure 4.19(b) also shows this dependence for different electron energies which will give a reliable way to correct the energy measured in the calorimeter.

Figure 4.20 shows also that the number of crystals in a supercluster is not directly correlated to the amount of irradiated bremsstrahlung, since the photon irradiation makes the cluster topology much more complicated. Depending on the emission point of the photon and of its energy, electron and photon clusters can be either well separated or mostly overlapped or can show intermediate cases. The net result on the average is a flat dependence on the number of crystals.

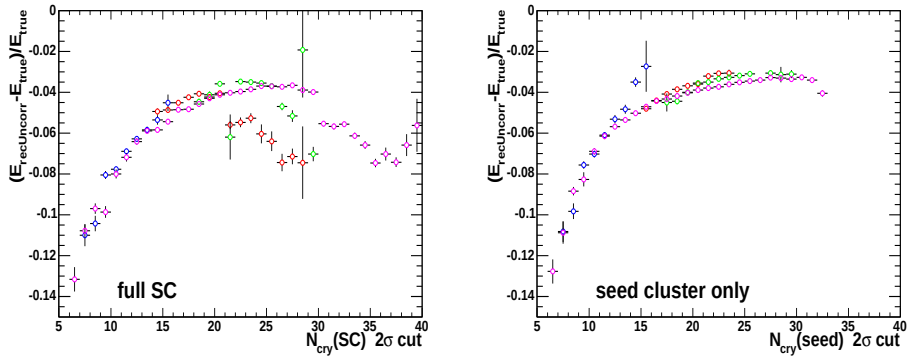

Figure 4.19: Normalized difference between raw reconstructed energy and true energy as a function of the number of crystals in the supercluster (a) and in the seed cluster only (b). Curves corresponding to different electron energies are showed on the same plot and demonstrate a dependence of the number of crystals in a supercluster from the electron energy.

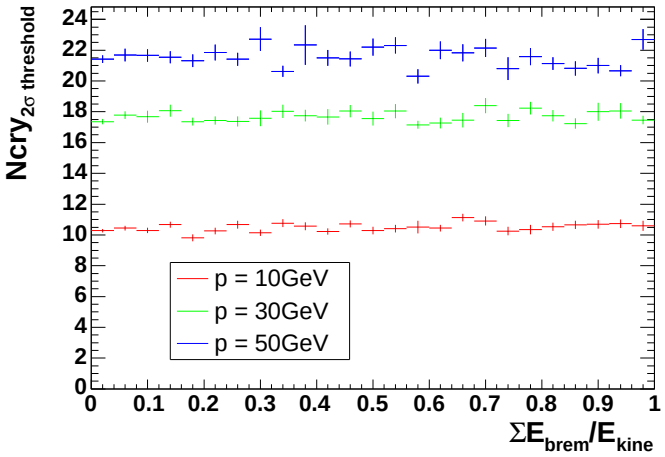

Figure 4.20: Number of crystals in a supercluster as a function of the amount of the electron energy loss by bremsstrahlung.

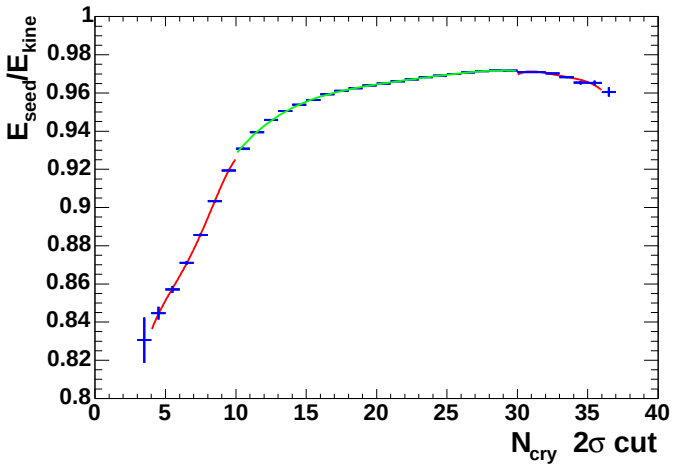

Figure 4.21: Function used to parametrize the raw energy dependence on the number of crystals for electrons in the barrel with momentum between 5 and 100 GeV/c.

These considerations suggest that the following strategy to properly scale the electron energy measurements in the barrel can be adopted.

For electrons belonging to the first three classes (those that have just the seed cluster in the supercluster) a rescaling based on N_{cry} (figure 4.21) leads to a very good correction along η except for the fourth module, where recollection problems and larger fractions of energy lost cause a reduced capability of bremsstrahlung detection by the ECAL alone and imply a deterioration in the measurement of 2% (figure 4.22(a)). This residual η dependence can be parametrized and corrected for.
For showering electrons, on the contrary, the correction based on N_{cry} is applied only on the seed cluster energy, under the hypothesis that bremsstrahlung photons are well measured by the calorimeter (if recollected). The rescaling of the electrons corresponding to regions at low pseudorapidity is very good, as demonstrated in figure 4.22(b) by the green curve. On the other hand, the correction based only on N_{cry} is not sufficient when the underlying hypothesis of good bremsstrahlung recovery is no longer valid and when the fraction of energy lost in front of ECAL becomes non-negligible, as can be seen by considering large η values in figure 4.22(b).

An estimate of all these effects is then needed and can be expressed by a

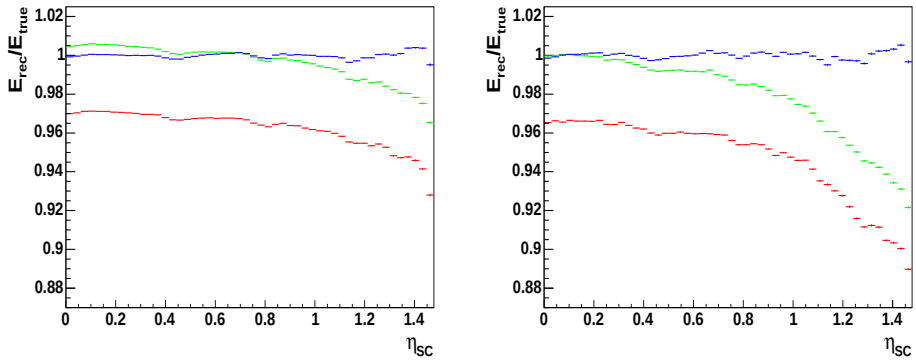

(a) (b)

Figure 4.22: Effects of the energy scale corrections as a function of the pseudorapidity for electrons with momentum in the range from 5 to 100 GeV/c. Golden, narrow and big brem classes are subjected to the same corrections and grouped in (a), showering are shown in (b). The red curve corresponds to the uncorrected energy, the green shows the effect of the $f(N_{\mathrm{cry}})$ correction and the blue curve of all the corrections.

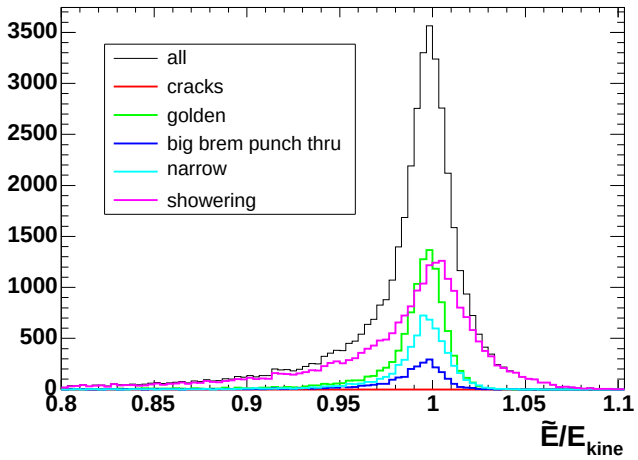

Figure 4.23: Distribution of the corrected energy normalized to the initial energy for electrons of momentum between 5 and 100 GeV/c.

Electron Class	% of electrons	Mean	Sigma
Barrel			
Golden	27.0	0.9978	$1.01 \cdot 10^{-2}$
Big Brem	5.7	0.9962	$8.75 \cdot 10^{-3}$
Narrow	12.0	0.9964	$1.07 \cdot 10^{-2}$
Showering	55.3	1.0010	$1.96 \cdot 10^{-2}$
Endcaps			
Golden	17.5	1.0077	$2.57 \cdot 10^{-2}$
Big Brem	3.3	1.0011	$2.30 \cdot 10^{-2}$
Narrow	6.7	1.0078	$2.34 \cdot 10^{-2}$
Showering	72.5	1.0078	$3.75 \cdot 10^{-2}$

Table 4.1: Relative percentage of electrons falling in the different classes for barrel and endcap regions. The results of a Gaussian fit on the peak of the distributions are also shown.

parametrization of the observed η dependence. The results of applying this subsequent correction are represented by the blue curve.

The distribution of the ratio between the measured energy and the true energy after the application of the corrections to electrons in the barrel with momentum between 5 and 100 GeV/c is shown in figure 4.23. Contributions of the different classes are also reported. The global distribution is clearly narrower and more Gaussian than the uncorrected one (figure 4.15). In table 4.1 the results of a Gaussian fit on the peak of the distribution is shown along with the relative percentage of electrons falling in the different classes.

A different treatment of these effects is needed for electrons reaching the ECAL endcaps. Since the standard reconstruction algorithm is different and the preshower is involved in the measurement, a detailed study involving both subdetectors is needed but not discussed here. The adopted strategy is a correction with a parametrization of the η dependence shown by the energy estimated combining crystals and preshower information.

4.5 Energy-Momentum Combination

In order to have the best estimator of the quadri-momentum at vertex of an electron, the information collected from tracking and calorimetry need to

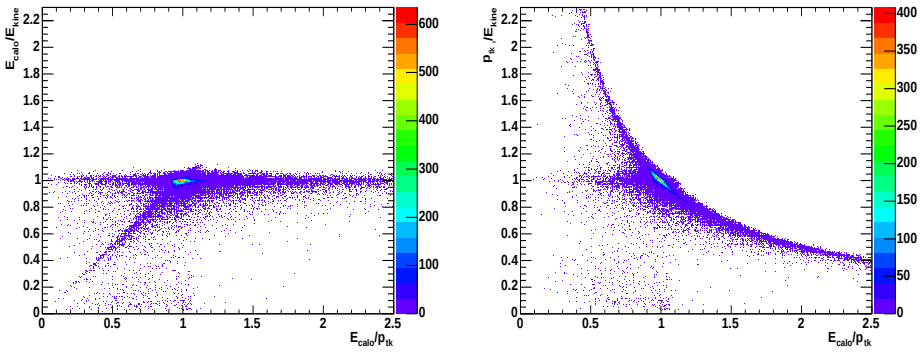

(a) (b)

Figure 4.24: Correlations between the quantities $E_{\mathrm{recUncorr}}/E_{\mathrm{true}}$ (a) and $p_{\mathrm{rec}}/E_{\mathrm{true}}$ (b) and the ratio $E_{\mathrm{recUncorr}}/p_{\mathrm{rec}}$ (see the text for a detailed explanation).

be combined. While the calorimeter is most suited for the absolute value of the momentum, the tracker can provide a very accurate measurement of the electron direction at the interaction point. The standard method to obtain the three components of the electron momentum consists in taking the angles from the tracker measurement and the absolute value of the momentum from the calorimeter.
However, while the tracker and the calorimeter do not have comparable resolutions for angular measurements (the former, not being limited by the uncertainty on the position of the interaction vertex, has a much better resolution) they become competitive for low energy measurements. An optimized estimator for the electron momentum at vertex would then combine calorimetry and tracking measurements to estimate the absolute value of the momentum.

In order to distinguish the cases in which the calorimeter and the tracker give the most accurate measurement, it is interesting to look at and compare the correlations between the quantities $E_{\mathrm{recUncorr}}/E_{\mathrm{true}}$ and $p_{\mathrm{rec}}/E_{\mathrm{true}}$ and the ratio $E_{\mathrm{recUncorr}}/p_{\mathrm{rec}}$. Figure 4.24(a) is showing that the energy measurement is generally good, even when the ratio $E/p \neq 1$: this is demonstrated by the ratio $E_{\mathrm{recUncorr}}/E_{\mathrm{true}}$ constantly around 1 for each value of the abscissa. The lower region on the left part corresponds to event under-estimating $E_{\mathrm{recUncorr}}$, since for those events the ratio $E_{\mathrm{recUncorr}}/E_{\mathrm{true}}$ is lower than 1.

Moreover, since for those events $E_{\text{recUncorr}}/E_{\text{true}} \approx E_{\text{recUncorr}}/p_{\text{rec}}$, as it can be deduced from the direct correlation between these two quantities, it follows that $p_{\text{rec}} \approx E_{\text{true}}$, thereby the momentum is well measured.
Analogous considerations can be made for the plot 4.24(b). In particular, the shape of the distribution of the events with $E_{\text{recUncorr}}/p_{\text{rec}}$ is of the form $1/p$, demonstrating that for those events the energy is well measured and the problems come from the momentum estimate. It is interesting to look at the left region of the plots, in which the electrons have $p_{\text{rec}}/E_{\text{true}} \sim 1$ and have then a good momentum measurement: since $E_{\text{recUncorr}}/p_{\text{rec}}$ is lower than one, the energy is under-estimated.
It is then possible to summarize the previous considerations with the following statements:

- there are no cases in which both energy and momentum are wrong, under- or over-estimating the true electron energy, since when E/p approximately equal 1 both are in good agreement with the Monte Carlo truth;
- cases with $E/p > 1$ are always due to a momentum underestimation, since in that region the energy is always well measured;
- cases with $E/p < 1$ are more complicated and can be due either to wrong energy measurement or to wrong momentum estimate.

The adopted strategy to combine energy and momentum translate these considerations in a practical procedure, assigning to calorimetry and tracking measurements proper weights to form the best estimator $\widetilde{E}$ as

$$\widetilde{E} = \frac{w_E E + w_p p}{w_E + w_p}. \tag{4.3}$$

For the energy measurements, there is an estimate of the associated error from the parametrization of the energy resolution, which differs for the different kind of electrons (figure 4.17): the weight for the energy is then $w_E = \sigma_E^{-2}$.

For tracking measurements the track fit error could give the precision on the momentum determination, and being an event-by-event quantity give more information than a simple parametrization of the tracker resolution as a function of the momentum and the pseudorapidity 4.25. However, the

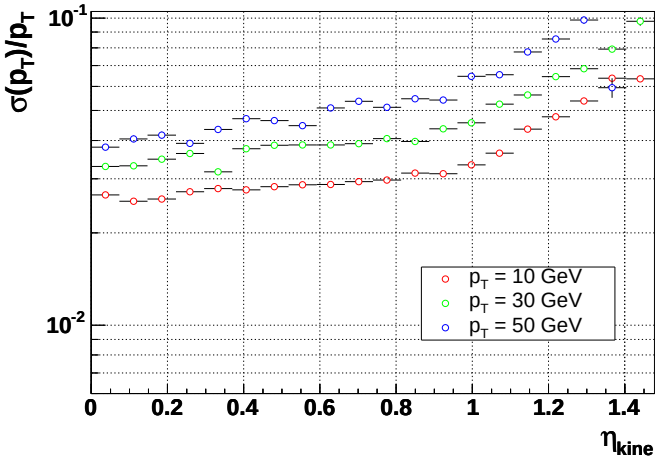

Figure 4.25: Tracker transverse momentum resolution as a function of the pseudorapidity for electrons of different initial p_T.

`GSF` algorithm provide error estimates only by taking the mean value of the p.d.f. associated to each of the fit parameters, while we are estimating them using the mode of their p.d.f.. An empirical approach, in which the error is defined as half of the smallest interval containing the mode value and such that the p.d.f. integral over that interval is 0.68, has been adopted.

A typical pull distribution obtained using this estimator for σ_p is shown in figure 4.26(a). Figure 4.26(b) plots the result of the Gaussian fit around the peak for pull distributions at different energies: a systematic overestimation of the errors is affecting the obtained values. In order to correct for this effect, which is indeed observed also for pull distributions computed with the mean `GSF` estimator and its standard error, an appropriate rescaling of σ_p has been applied. This rescaling brings the sigma of the pull distributions back to 1.

The results of the combination are plotted in figure 4.27(a), where the resolution of the combined estimator $\widetilde{E}$ is computed at different energies. The improvement with respect to single estimator from calorimetry or tracking is evident. The relatively small improvement in the region around 25 GeV/c where energy and momentum have compatible uncertainties is probably due to common systematic effects affecting both the measurements (namely bremsstrahlung emission). However, a big difference can be

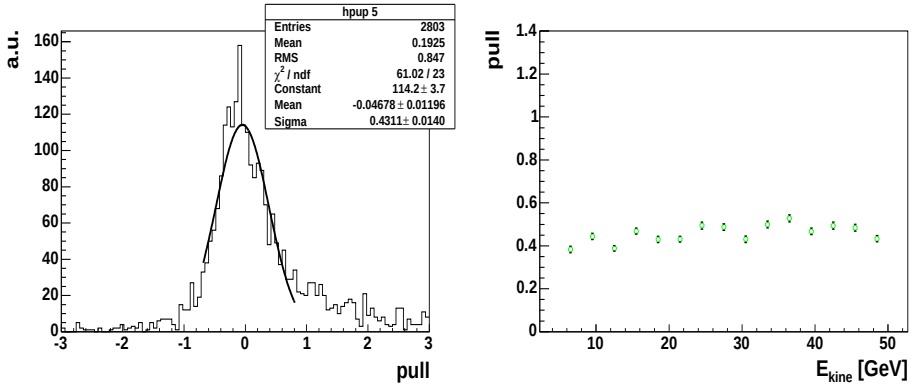

(a) (b)

Figure 4.26: *Left*: example pull distribution for electrons with momentum of 15 GeV/c. *Right*: pull values obtained for electrons with different initial energy.

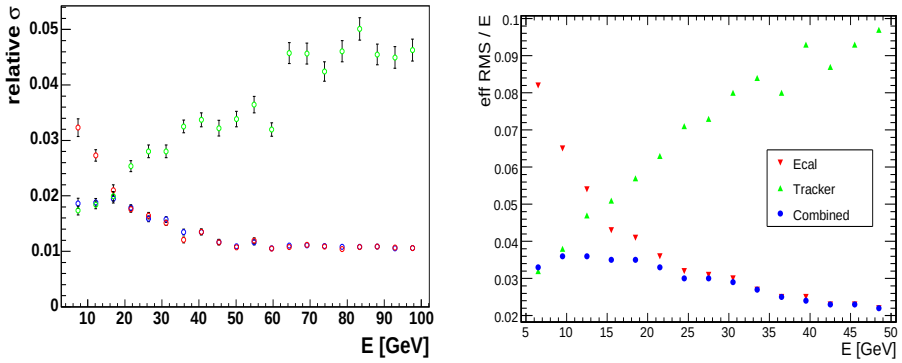

(a) (b)

Figure 4.27: Results of the combination of energy measurement from the calorimeter and momentum measurement from the tracker. The resolution $(\sigma(\widetilde{E})/E)$ on the best estimate of the electron four momentum at the initial vertex is shown in (a) as a function of the electron energy. In (b) the effective RMS of the distribution $\widetilde{E}/E$ is shown.

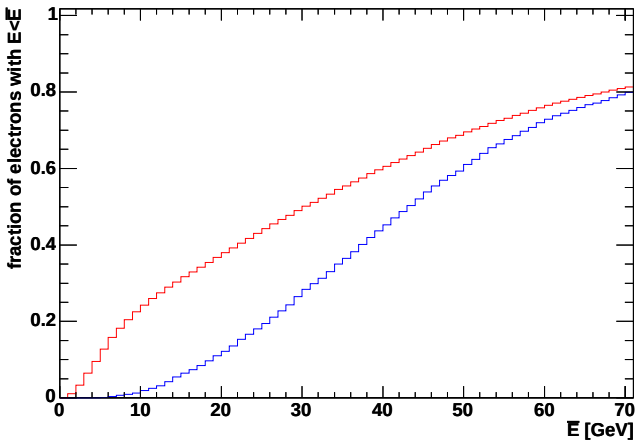

Figure 4.28: Fraction of electrons in $H \to ZZ^{(*)}$ events with an energy E lower than $\overline{E}$. The red curve shows the distribution before any selection while the blue curve shows the same distribution after basic standard selections on the electron p_T, on isolation, and on Z, $Z^{(*)}$ and four electrons invariant mass are applied (see chapter 5 for more details on the selection strategies).

seen looking at the effective RMS of the corresponding distributions 4.27(b), which are much narrower for the combined estimator $\widetilde{E}$ than either p or E.

4.6 Effects on the $H \to ZZ^{(*)} \to 4e$ physics

Details on electron reconstruction and selection in a full physics simulated event will be given in chapter 5. The assumption made here is that the electron candidates 4.2 in a $H \to ZZ^{(*)} \to 4e$ event have been built and properly selected. The interest is on the effect of the corrections on the most important physical observables of the event for a typical Higgs mass case of $m_H = 150$ GeV/c^2.

As a preliminary observation, the fraction of electrons with energy below 25 GeV, the range in momentum with the biggest improvement from the energy-momentum combination, is around 40% for a low Higgs mass point, while it decreases for higher masses (see as an example the distribution for $m_H = 150$ GeV/c^2 in figure 4.28). It is also interesting to notice the effect of the HLT trigger on the electron population: as expected, the fraction of

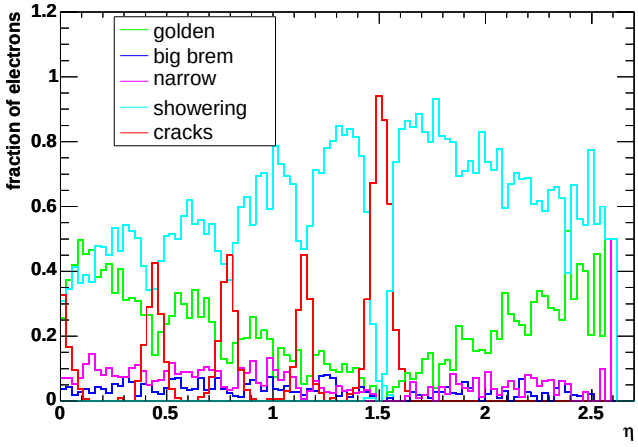

Figure 4.29: Fraction of electrons in $H \to ZZ^{(*)}$ events belonging to the different classes as a function of the electron pseudorapidity.

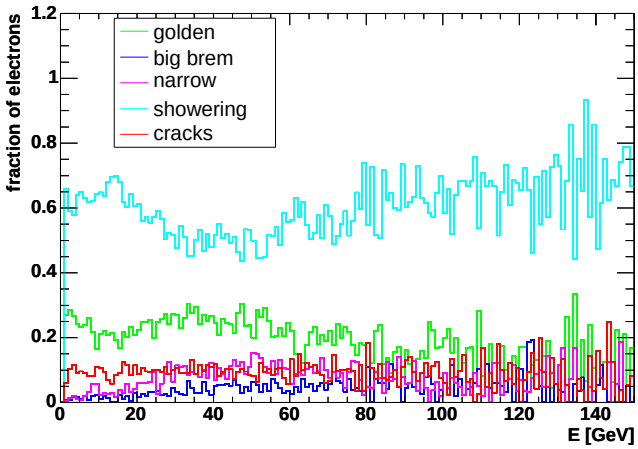

Figure 4.30: Fraction of electrons in $H \to ZZ^{(*)}$ events belonging to the different classes as a function of the electron energy.

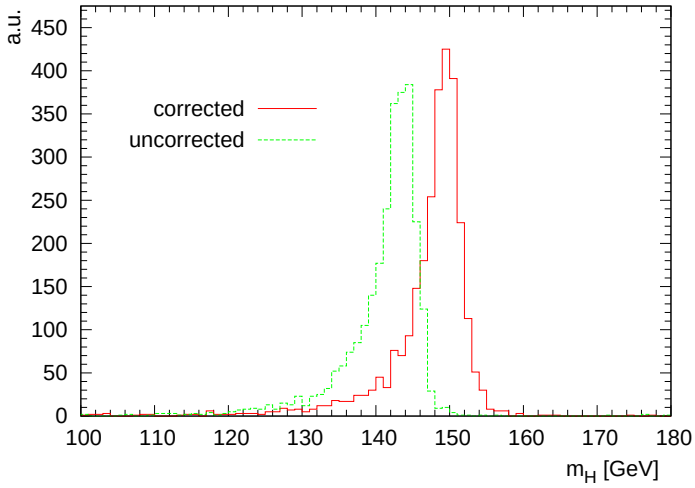

Figure 4.31: Effects of the corrections on the Higgs invariant mass, for a Higgs mass hypothesis of $m_H = 150$ GeV/c^2.

events containing more low p_T electrons has less probability of being triggered.
The distribution of electrons in the different classes is shown as a function of the pseudorapidity (figure 4.29) and of the electron energy (figure 4.30). In particular, the first distribution follows the material budget profile and the second exhibit a more problematic behaviour for soft electrons, consistently to what expected. The effect of the energy scale correction and of the energy-momentum combination on the Higgs invariant mass is shown in figure 4.31. The peak is correctly shifted on the generated Higgs mass value and the distribution is clearly narrower.

The same effects are observable on the Z mass plot, as shown if figure 4.32(a). The effect of the corrections for the virtual Z mass distribution, which is very important because it can be used to discriminate among different hypothesis for the Higgs spin and CP quantum numbers, is shown in figure 4.32(b).

4.7 Conclusions

The chapter presents detailed studies of the electron reconstruction inside CMS which have been carried out in order to analyze the main effects which affect the measurements of the electron energy using the electromagnetic

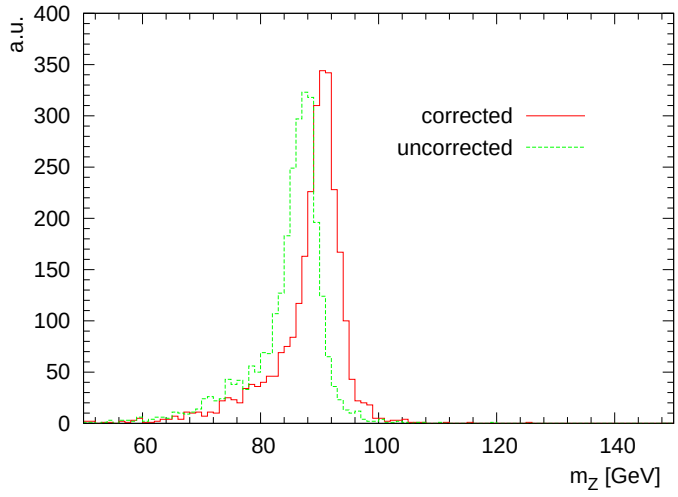

(a)

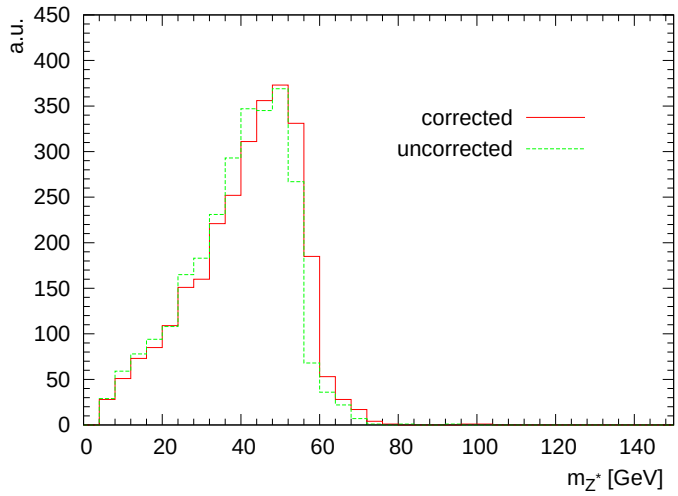

(b)

Figure 4.32: Effects of the corrections on the Z (a) and Z^* (b) invariant mass, for a Higgs mass hypothesis of $m_H = 150$ GeV/c^2.

calorimeter.
In particular the bremsstrahlung effect, which is due to the tracking material in front of the calorimeter, is the main problem to be faced, since it causes non-negligible losses of the electron energy which are often irrecoverable by the reconstruction algorithms. In order to determine the quality of the electron energy measurement, a classification of the electron based on tracking and calorimetry observables has been proposed. According to this classification, a scaling of the measured energy has been computed in order to bring the energy of an electron as close as possible to its initial value. A parametrization of the energy resolution for the different classes has allowed to attribute an error to the energy measurement. This, together with the tracking momentum measurement and its error, can be used in order to optimally combine the information from the calorimeter and the tracker to have the best estimate of the electron four momentum at the interaction point.
Particular care has been given to electrons with low transverse momentum, which constitute a good fraction of the total number of the electrons coming from the Higgs boson decay $H \to ZZ^{(*)} \to 4e$. Using the final estimate of the electron momentum, the Higgs mass peak is correctly found around the expected value and the resolution on the Higgs mass is clearly improved.

Bibliography

Adam, W., Frühwirth, R., Strandlie, A. and Todorov, T. (2005), *Reconstruction of Electrons with the Gaussian-Sum Filter in the CMS Tracker at the LHC*, CMS NOTE 2005/001.

Baffioni, S., *et al.*. (2005), *Electron reconstruction: e Classes, E scale Corrections and E-p combination*, CMS AN, Note in preparation.

Charlot, C., Rovelli, C. and Sirois, Y. (2005), *Reconstruction of Electrons at Low PT Using Gaussian Sum Filter Tracks*, CMS AN 2005/011, Note in preparation.

CMS Collaboration (2002), *CMS: The Trigger and Data Acquisition Project, Volume II: Data Acquisition and High-Level Trigger Technical Design Report*, CERN/LHCC 2002-26.

ORCA (2004), *Object-oriented Reconstruction for CMS Analysis*, http://cmsdoc.cern.ch/orca/.

Chapter 5

The $H \rightarrow ZZ^{(*)} \rightarrow 4e$ channel

The Higgs mechanism is the current best model for the electroweak symmetry breaking in the Standard Model (SM) of elementary particle physics. However, the existence of the massive scalar particle associated to the symmetry breakdown, the Higgs boson, has not yet been proven and remains the most important objective of the LHC physics program.
Within the possible decay modes of the Higgs bosons, the channel $H \rightarrow ZZ^{(*)}$ is the second golden channel after $H \rightarrow \gamma\gamma$ for Higgs masses below twice the Z mass (section 1.2.5). Despite the fact that its branching ratio is lower than the corresponding $H \rightarrow WW^{(*)}$ channel, it provides a clean experimental signature for the detection of the signal events over the background and allows a direct measure of the Higgs boson mass and width. Furthermore, it is the best channel for characterizing the Higgs spin and CP quantum numbers from the angular correlations of the $ZZ^{(*)}$ decay products (typically only the leptons are considered). Used in conjunction with the information from the decay $H \rightarrow WW^{(*)}$, it also allows for the measurement of the Higgs couplings to the weak gauge bosons.

In this chapter, a detailed analysis of the channel $H \rightarrow ZZ^{(*)}$ when the two Z bosons decay into two electron and positron pairs[1] is presented. The existing results ((Puljak, 2000),(Meridiani, 2003)) are thereby updated and the way to possible new strategies to be adopted in order to improve the significance for the Higgs boson discovery is also presented.
This channel presents several experimental challenges, which are mainly re-

[1] $4e$ in the following, where the charge conjugate states e^+ and e^- are referred to as electrons, unless specifically mentioned.

lated to the extraction of an electron signal from a very difficult environment. Indeed, the considerable amount of radiation emitted by bremsstrahlung can affect both the electron reconstruction efficiency and the measurement of their energy. In order to optimally cover the wide momentum range (from $\mathcal{O}(1$ GeV$/c)$ to $\mathcal{O}(10^2$ GeV$/c)$) of the four electrons a combination of tracking and calorimetry information is needed to provide the best possible estimate of the electron quadri-momentum at the interaction point (chapter 4).

In order to distinguish events coming from a Higgs decay from the background, two main strategies have been adopted.
The first one is based on the selection of the signal events according to selection criteria on the most significant kinematic and topological variables of the events. A study of these characteristics will thus be presented below to illustrate and motivate the choices.
The second approach has been to use all the significant variables together to classify the events by means of a Neural Network. It has been long demonstrated (Prosper, 1993) that Neural Networks can be used to estimate the *a priori* probability of an event to be signal or background, thus allowing an analysis based on the standard statistical tools, such as, for example, maximum likelihood ratio tests. In section 5.7.3, a demonstration of this statement will be provided. Furthermore, the application of Neural Networks to the events selection in some of the major physics analysis in the past both for trigger and analysis techniques has successfully shown the efficiency of this technique in event selection and pattern identification.
A deep understanding of the event characteristics is however a necessary condition for the fruitful use of Neural Networks and the evaluation of the systematics uncertainties related to the classification. This also constitutes a solid basis for more evolved analysis.

In the following sections, signal and backgrounds for the $H \to ZZ^{(*)} \to 4e$ channel will be introduced, the adopted strategies to select the events will be illustrated and the obtained results for the significance of the Higgs boson discovery using the CMS detector at LHC will finally be presented.

5.1 Signal and Background Definition

The signal considered in this analysis is characterized by the presence of four electrons in the final state. The background is thus constituted by all the processes with at least four final state electrons, either prompt or

from hadron misidentification. The most important contributions to the background come from:

- $ZZ^{(*)}$ events, with the Z decaying into an electron-positron pair;
- $Zb\overline{b}$, where the two b quarks decay semileptonically into electrons;
- $t\overline{t}$, where the top quark decays with branching ratio ~ 1 into Wb and electrons in the final state may come from the decay $W \to e\nu_e$ and from semileptonic decays into electrons in the b decay chain (e.g. b).

Having two Z in the intermediate state, the $ZZ^{(*)}$ background is called "irreducible", since it has many kinematical characteristics similar to the signal. The two remaining backgrounds constitute the so-called "reducible" background.

Before explaining in detail the analysis strategies for the event reconstruction with the full CMS detector simulation, it can be useful to look at general properties of signal and background.

The most important feature of the signal is that the four electrons come from the decay chain of a single particle, the Higgs boson. This implies that their invariant mass peaks at the Higgs mass, while for the other backgrounds a flat distribution is anticipated. The Higgs boson search would then consists in looking for the appearance of a peak in the four electron invariant mass distribution.

Signal events are also identifiable for the presence of two Z bosons in the intermediate state. Depending on the hypothesis for the Higgs mass, the two bosons could be either real or off the mass shell (virtual), the fraction of virtual Z decreasing with the increase of the Higgs mass.
Moreover, assuming that the Standard Model Higgs is a CP-even scalar particle, the two Z bosons from the Higgs decay are mainly longitudinally polarized. This implies that the shape of the differential cross-sections on the angle ϑ between one lepton in the Z rest frame and the direction of its parent in the Higgs rest frame, is of the form $\frac{d\sigma}{d\cos\vartheta} \sim \sin^2\vartheta$. It can be demonstrated (Choi *et al.*, 2003) that for the $ZZ^{(*)}$ background, which also has two Z as intermediate state, the bosons are mainly transversely polarized. This polarization implies a differential cross-section of the form $\frac{d\sigma}{d\cos\vartheta} \sim \cos^2\vartheta$, which could be in principle exploited to enhance the background rejection.

Reversing the argument, it is possible, in principle, to identify the Higgs spin and CP quantum numbers from the angular distribution of its decay products. The channel $H \to ZZ^{(*)} \to 4e$ is optimal for this purpose, since the final state can be completely reconstructed. Also the shape of the mass spectrum of the virtual Z boson could be used to discriminate different spin-CP hypothesis for the Higgs particle. For an example of these studies on the Higgs quantum numbers determination, see (Godinović, 2003).

The analysis of the transverse momentum distribution of the four final state electrons would lead to the consideration that there are substantial differences for signal and background, especially for the two softest p_T electrons. Furthermore, the presence of neutrinos in the decay chain of both b and t quarks imply a greater missing energy for the reducible backgrounds with respect to signal events. Finally, the four electrons from the Higgs decay are compatible with a single vertex hypothesis, while, for the $Zb\overline{b}$ and $t\overline{t}$ backgrounds, the electrons from the b and t decay tree come from secondary vertices.

5.2 Signal and Background: Generation and Simulation

In order to simulate the signal and background for the $H \to ZZ^{(*)} \to 4e$ channel, the CMS full simulation chain and the standard CMS reconstruction tools have been used in the analysis (ORCA, 2004).
Leading-Order generators (mainly PYTHIA (Sjostrand *et al.*, 2001), CompHEP (Pukhov *et al.*, 1999) in one background case) have been used to generate signal and background processes. As discussed in section 1.2.5, these are inadequate to describe the production at the LHC. For this reason, an *a posteriori* normalization to Next-to-Leading-Order cross section values using p_T dependent scale factors with the p_T spectrum, computed using the MC@NLO Monte Carlo tool (Frixione and Webber, 2004), has been introduced.
To simulate final state QED radiation, the PHOTOS package has also been used (Barberio and Was, 1994).
In order to accelerate the event production without biasing the sample for the analysis, a preselection at the generator level has been applied. This permits to fully trace in the detector only the events with four final state electrons within the CMS angular acceptance for electrons ($|\eta| < 2.7$) and

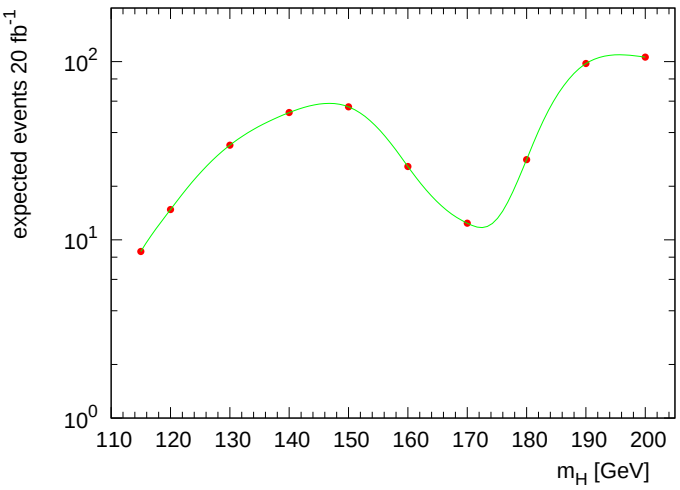

Figure 5.1: Expected number of signal events after one year of LHC running at an integrated luminosity of 20 fb^{-1}.

with a transverse momentum sufficiently high ($p_T > 5$ GeV/c) to allow a good efficiency in the electron detection.
The low luminosity scenario ($\mathcal{L} = 2 \cdot 10^{33}$ cm^{-2}s^{-1}) for the LHC has been considered, and 3.5 pile-up events have been added to each signal and background event before the detector digitization step of the simulation.

5.2.1 Signal

The signal has been generated with PYTHIA 6.223 (using the CTEQ5L set of parton distribution functions) for a wide set of Higgs masses, 10^4 events for each mass point. For $m_H < 2m_Z$, Higgs masses from 120 GeV/c^2 to 180 GeV/c^2 have been generated, with an additional point at 115 GeV/c^2, the lowest mass non excluded by LEP2 results. Events where the four electrons in the final state come from the decay $Z^{(*)} \to \tau$ with the τ forced to decay into an electron have been excluded from the analysis, since, due to the presence of neutrinos in the final state, they contribute to the tail of the $4e$ invariant mass distribution rather than to the peak.

The expected number of events in one year of the LHC running at an integrated luminosity $\mathcal{L} = 20$ fb^{-1} is shown in figure 5.1 and the relevant

m_H [GeV/c^2]	$\sigma(gg \to H)$ [pb]	$\sigma(qq \to Hqq)$ [pb]	$\sigma(q\overline{q} \to WH)$ [pb]	$\sigma(q\overline{q} \to ZH)$ [pb]	$\sigma(q\overline{q}, gg \to ttH)$ [pb]	σ_{tot} [pb]	B.R.$(H \to ZZ^{(*)})$	ε_{kin}	$\sigma_{\text{tot}} \times$ B.R.$(H \to ZZ^{(*)} \to 4e)$ [fb]	$\sigma_{\text{tot}} \times$ B.R.$(H \to ZZ^{(*)} \to 4e) \times \varepsilon_{\text{kin}}$ [fb]
115	39.3	4.65	1.98	1.05	0.75	47.73	0.008	0.54	0.43	0.23
120	36.5	4.47	1.74	0.92	0.67	44.30	0.015	0.56	0.74	0.41
130	31.7	4.14	1.35	0.72	0.53	38.44	0.039	0.61	1.70	1.04
140	27.8	3.83	1.06	0.57	0.43	33.69	0.068	0.65	2.59	1.68
150	24.6	3.56	0.84	0.45	0.35	29.80	0.083	0.67	2.79	1.87
160	21.9	3.32	0.68	0.37	0.29	26.50	0.043	0.69	1.29	0.89
170	19.7	3.09	0.55	0.30	0.24	23.88	0.023	0.71	0.62	0.44
180	17.8	2.88	0.46	0.25	0.20	21.59	0.058	0.73	1.41	1.03
190	16.2	2.71	0.38	0.21	0.17	19.67	0.219	0.74	4.88	3.61
200	14.8	2.53	0.32	0.17	0.15	17.97	0.261	0.74	5.30	3.92

Table 5.1: Cross-section for the Higgs boson production, branching ratio into $ZZ^{(*)}$ and preselection efficiency for different Higgs mass hypothesis. The cross section values are obtained from (Spira, 2005), the branching ratio from (Djouadi *et al.*, 1998). A mass of 175 GeV/c^2 for the top quark has been assumed.

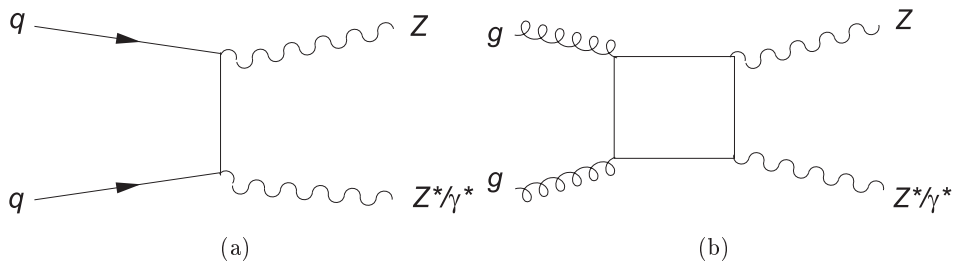

Figure 5.2: Leading order processes for the s-channel $ZZ^{(*)}$ production in hadronic collisions.

cross-sections, branching ratios and preselection efficiencies are reported in table 5.1 for the different Higgs masses.

5.2.2 Backgrounds

As already mentioned in 5.1, the sources of background for the $H \to ZZ^{(*)} \to 4e$ channel are events with four high-p_T electrons in the final state, coming from the production of $ZZ^{(*)}$, $Zb\overline{b}$, and $t\overline{t}$. Other sources of backgrounds consisting of events where jets can be misidentified as electrons (namely $Z+$jets events) are reduced to a negligible level by the adopted strategies to enhance the signal to $4e$ background ratio ((Puljak, 2000), (Meridiani, 2003)) and have not been analyzed in detail.

Irreducible background: $ZZ^{(*)}$

The leading order processes for gauge bosons pair production in hadronic interactions is the $q\overline{q}$ annihilation, shown in figure 5.2(a). An additional contribution, corresponding to 20% of the $q\overline{q} \to ZZ^{(*)}$ process, comes from $gg \to ZZ^{(*)}$. Indeed, the lower amplitude of the $gg \to ZZ^{(*)}$, which is a higher order process in α_s since it involves a quark box diagram (figure 5.2(b)), is balanced by the higher gluon luminosity with respect to the quark-antiquark one when the partons carry a low fraction of the total momentum.

NLO corrections are available only for the first process and predict a correction (K factor) of 1.33. The total production cross-section, branching ratio and preselection efficiency are reported in table 5.2.
Events were generated with PYTHIA 6.223, which only implements the $q\overline{q}$ annihilation. The number of expected events has been rescaled to the total

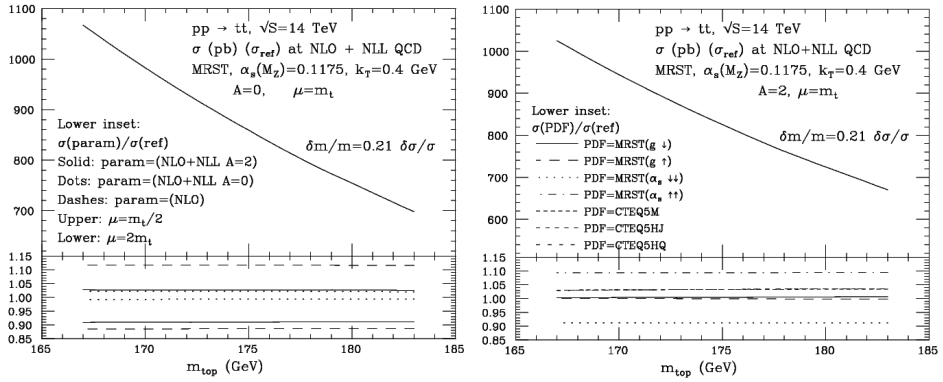

Figure 5.3: $t\bar{t}$ production rates. *Left*: scale dependence at fixed order (NLO, dashed lines in the lower inset), and NLO+NLL (solid lines). *Right*: pdf dependence. See (Almadov, 2000) for more details.

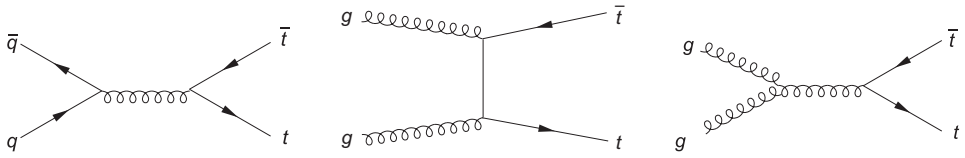

Figure 5.4: Leading order Feynman diagrams for the $t\bar{t}$ production in hadronic collisions.

cross-section, including the gg fusion process. This implies some systematic uncertainty, which is related to the kinematical difference between the two production process (which are indeed considered to be small (Meridiani, 2003)).

Reducible background: $t\bar{t}$

The two main processes for $t\bar{t}$ production in p-p interactions are gluon fusion and quark annihilation (figure 5.4). The corresponding cross-section at the LHC for different choices of the renormalization scale and of the parton density functions is shown in figure 5.3. The suggested value for the cross-section is 840 pb with 5% of uncertainties coming from the scale and 3% from the pdf's (Beneke *et al.*, 2000).

Sources of electrons in the final state are the two top quark decay chains (figure 5.5). $t \to Wb$ has a branching ratio of 99.8%: electrons arise from the semileptonic decays of the bottom quark and from the W, via direct decay

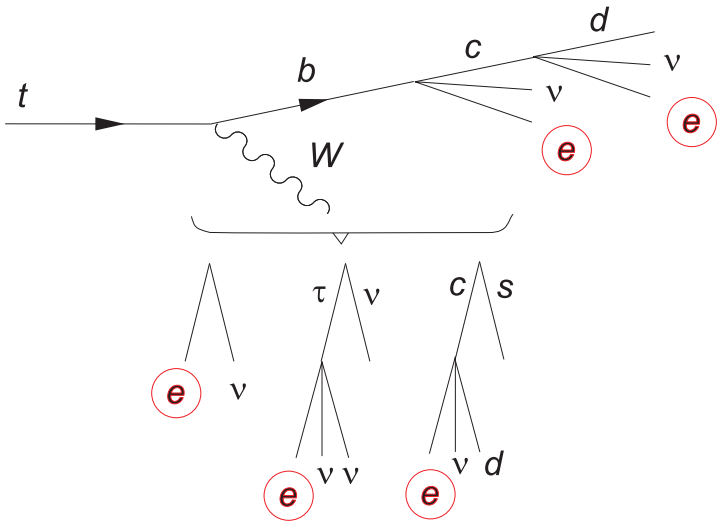

Figure 5.5: Possible sources of electrons in the top quark decay chain.

$W \to e\nu_e$ or $W \to \tau\nu \to e\nu\nu$. Semileptonic decays of mesons produced in $W \to$ hadrons give a negligible contribution to events with four electrons in the final state.
Total cross-section, branching ratios and preselection efficiency for this channel are reported in table 5.2. The comparison of the values with the signal and the other background sources show that this channel is the largest contributor to a final state with four electrons, and its effective cross-section is around a factor $\sim 10^2$ greater than the signal one. At the analysis level, the last number gives the order of magnitude of the rejection power needed to enhance the signal to $t\bar{t}$ background ratio.
The sample of events has been generated with PYTHIA 6.223. The 75800 events have been produced without any requirement on the b-quark decay, but by imposing that the W boson decays leptonically.

Reducible background: $Zb\bar{b}$

The third source of background having four electrons in the final state consists in the $Zb\bar{b}$ production and decay. The leading order diagrams corresponding to the two possible initial states producing $Zb\bar{b}$ ($q\bar{q}$ and gg) are shown in figure 5.6.
For the cross-section calculation and the event generation, the CompHEP

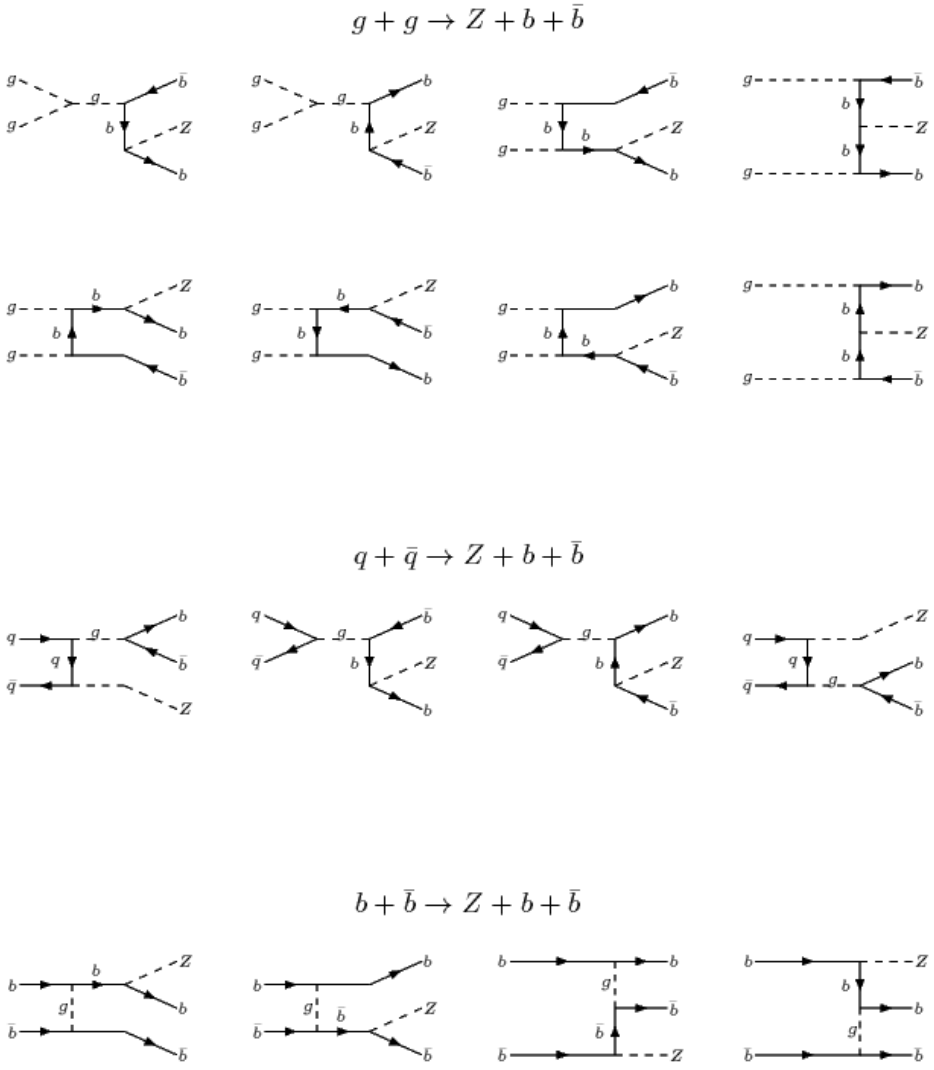

Figure 5.6: Leading order diagrams corresponding to the possible initial states producing $Zb\overline{b}$.

Background	σ_{NLO} [pb]	B.R.	$\varepsilon_{\mathrm{kin}}$	$\sigma_{\mathrm{NLO}}\times$ B.R. [fb]	$\sigma_{\mathrm{NLO}}\times$ B.R. $\times\varepsilon_{\mathrm{kin}}$ [fb]
$ZZ^{(*)}$	35.1	$1.13 \cdot 10^{-3}$	0.23	39.6	9.12
$t\bar{t}$	886	$6.31 \cdot 10^{-2}$	$3.20 \cdot 10^{-3}$	$56 \cdot 10^{3}$	178.9
$Zb\bar{b}$	115.1	1	$4.63 \cdot 10^{-4}$	115.1	53.30

Table 5.2: Cross-section, branching ratio and preselection efficiency for the different backgrounds. A mass of 175 GeV/c^2 for the top quark has been assumed.

package has been used. PYTHIA could not be used to accomplish this because it does not take into account the process $gg \to Zb\overline{b}$, which contributes to over 80% of the total cross section.
The production of the 115126 events has considered also the case of a virtual Z bosons and two b quarks, with a limit on the Z^* invariant mass as well as on the invariant mass of the b pair of 5 GeV/c^2. In this sense the background could be seen as e^+e^-bb (and the cross section reported in the following is to be considered as computed after the requirement on the invariant masses of the electron and b pairs). The b quarks have not been forced to decay into electrons.
The corresponding value for cross-section and branching ratio have been reported in table 5.2.

5.3 Events Trigger and Preselection

As explained in greater detail in the detector description (chapter 2), the CMS trigger consists basically of two steps: the Level-1 (L1) and the High-Level-Trigger (HLT). The full reconstruction is performed only for events passing these two selections. The useful triggers of the HLT trigger table for the $H \to ZZ^{(*)} \to 4e$ channel are:

- single electron, with a transverse energy threshold of 26 GeV;
- double electron, requiring a transverse energy greater than 14.5 GeV for two electrons;
- double relaxed electron, requiring two electrons with a transverse energy of 21.8 GeV.

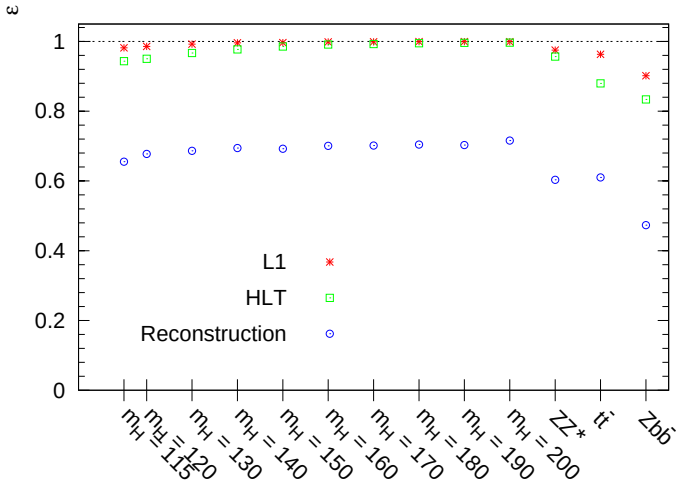

Figure 5.7: Absolute efficiency (as defined in section 5.3) for the Level-1 Trigger, the High Level Trigger and the reconstruction of four electrons candidates.

The absolute efficiency has been defined as the ratio between the number of events passing specific requirements (e.g. L1 or HLT triggers) and the total number of preselected events at the generator level. Results for the absolute efficiency of L1 and HLT are shown in figure 5.7, for different Higgs masses and for the background sources. The figure also shows the reconstruction efficiency, which is defined as the efficiency of finding at least two electrons and two positrons with an energy greater than 5 GeV. For signal events the loss in the trigger efficiency is negligible if compared to the one at the final state reconstruction level.

5.4 Signal Reconstruction and Background Rejection

In this section details on the analysis of the reconstructed events from the full detector simulation are given. All the relevant steps of the reconstruction are discussed in detail, focusing on the aspects related to the search for a peak in the invariant mass of the four final state electrons.

5.4.1 Off-line reconstruction

The off-line reconstruction electrons takes place only for events passing the HLT. As described in 4, it consists in collecting Superclusters in the calorimeter, reconstructing tracks using the GSF algorithm and combining them to form electron candidates according to precise criteria.
An additional step to resolve ambiguities is needed to avoid multiple sharing of electron tracks and clusters among several electron candidates. In order to select final candidates, electrons sharing the same track or superclusters are grouped in a single collection. The unambiguous candidates are then selected according to the best matching in E/p, between calorimeter and tracker measurements.
Once electron candidates have been collected, a further selection has been applied to define "electron" objects on the basis of some criteria of electron identification. These criteria involve the ratio of energy measured in HCAL and ECAL, geometrical matching between the supercluster and the last point of the track segment, supercluster shape parameters. They consist in (fore more detail see (Baffioni, 2005)):

- ratio of energy measured in HCAL (H) and ECAL (E): $H/E < 0.1$;
- angular distance from the supercluster and the last point of the electron track: $\Delta\phi < 0.1$ and $\Delta\eta < 0.01$;
- ratio between the energy of the seed crystal and the momentum measured at the last track point greater than 0.5
- sum of the energy deposited in arrays of crystals centered on the crystal with the maximum energy deposition: $3 \times 3/5 \times 5 > 0.5$;
- shower spread in η (the second moment of the η projection of the transverse profile): $\sigma_{\eta\eta} < 0.05$.

The distribution of the total number of electron candidates for preselected signal and background events is shown in figure 5.8. The higher number of reconstructed electrons for the background events corresponds to a higher probability of having electrons in jets and of having jets misidentified for electrons. An isolation criteria is effective in reducing the vast majority of these events.
Each electron is then classified according to the criteria exposed in chapter 4.

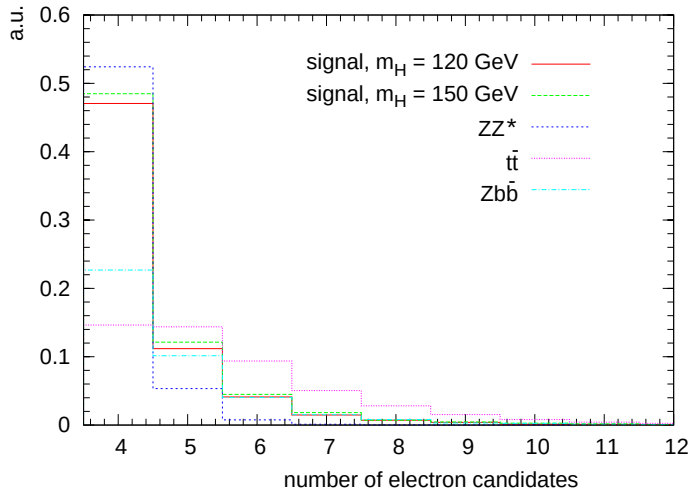

Figure 5.8: Number of electron candidates for signal and background events.

The energy scale correction and the combination of calorimetry and tracking information is then performed to estimate at best the four-momentum at the interaction point.

5.4.2 Internal Bremsstrahlung

The four electrons final state is affected by the emission of photons by the electron from the Z decay. This effect is called internal (or inner) bremsstrahlung. In these events the final state also includes photons, which are difficult to find at the reconstruction level and can then be lost. This effect is investigated in order to evaluate possible consequences on the Higgs invariant mass measurement. Events might indeed fall outside the mass peak if the internal bremsstrahlung photon is not properly reconstructed. Similar effects are irrelevant in background events, which exhibit a continuous spectrum for the invariant mass of the final state electrons.
The energy distribution of all the photons emitted by internal bremsstrahlung divided by the energy of the closest electron is shown in figure 5.9. Figure 5.10 shows the angular distance in the η-ϕ coordinates between the photon and the closest electron. The effect on the Higgs invariant mass resolution if the internal bremsstrahlung photon is not taken into account is shown in figure 5.11. If the photon is not collected by the reconstruction algorithms

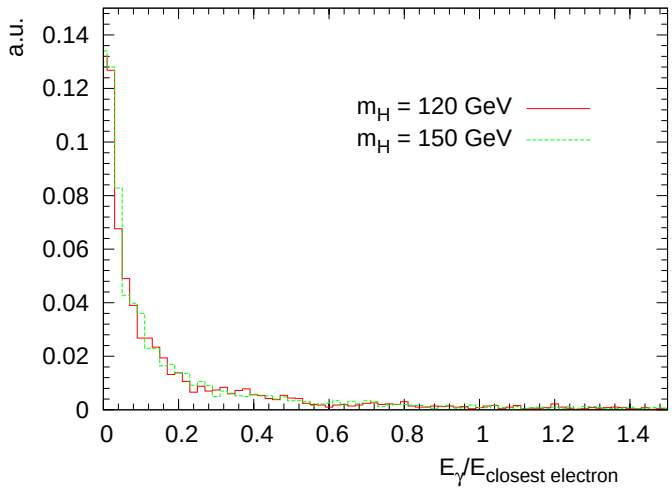

Figure 5.9: Ratio between the energy of the photon from internal bremsstrahlung and the energy of the electron closest in $\Delta R = \sqrt{\Delta\eta^2 + \Delta\phi^2}$.

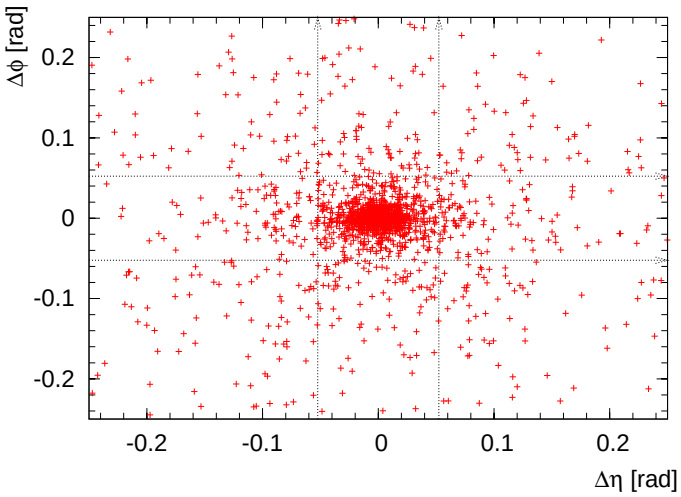

Figure 5.10: Distribution of the angular distance in the η-ϕ coordinates for the internal bremsstrahlung photon and the closest electron in $\Delta R = \sqrt{\Delta\eta^2 + \Delta\phi^2}$. The dotted lines represent the angular distance corresponding to 3 crystals (in η or ϕ, according to the axis).

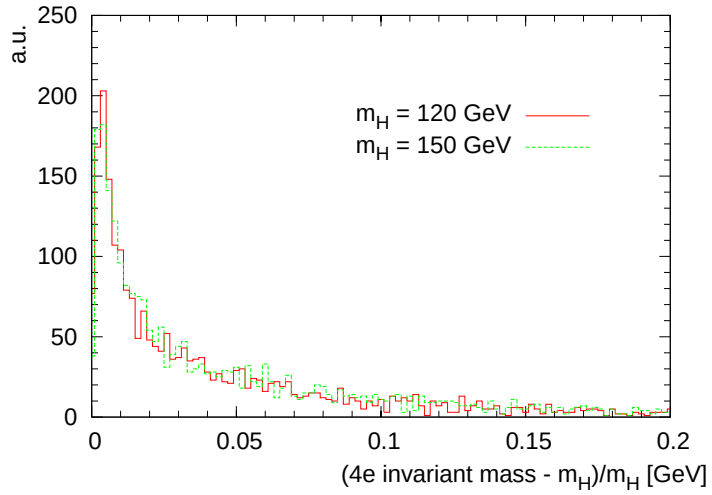

Figure 5.11: Effect of neglecting internal bremsstrahlung photons in the invariant mass computation: on the abscissa the normalized difference between the four invariant mass computed with and without considering photons in the final state is reported.

the effect is, therefore, not negligible.

However, since the photon is generally emitted close to an electron, there is a non-negligible probability that both photon and electron will also hit the calorimeter close to each other and will be collected in the same supercluster. In order to investigate this possibility, one can look at the extrapolated $\Delta\phi_{\mathrm{ECAL}}$ at the calorimeter, adding to the initial $\Delta\phi$ between the photon and the closest electron the $\Delta\phi$ due to the bend of the electron in the magnetic field. The latter quantity is given by the equation

$$\Delta\phi_{\mathrm{ECAL}} = \arctan\frac{R_{\mathrm{ECAL}}}{2\varrho}\left(1 - \left(\frac{R_{\mathrm{ECAL}}}{2\varrho}\right)^2\right)^{-1/2} \quad , \quad \varrho = p_T/(0.3 \cdot B), \tag{5.1}$$

where R_{ECAL} is the ECAL radius in meters, and ϱ is the curvature radius of the electron, with its momentum p_T measured in GeV/c and the magnetic field in Tesla.

As can be seen in the plot of the normalized difference between the invariant mass of the $4e$ and the invariant mass of the $4e + \gamma$ as a function of the $\Delta\phi_{\mathrm{ECAL}}$ (figure 5.12), the biggest effect are present for low $\Delta\phi$. The two

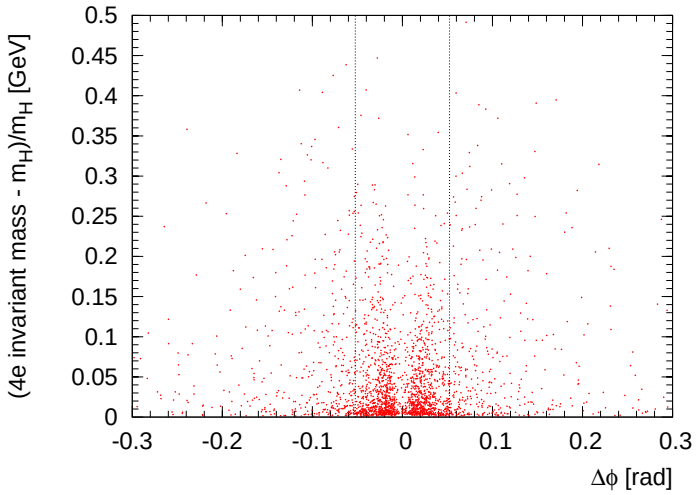

Figure 5.12: Normalized difference between the four electron invariant mass computed with and without considering photons in the final state as a function of the angular difference in φ at the ECAL entrance between the photon and its closest electron. The dotted lines represent the angular distance corresponding to 3 crystals in ϕ.

lines on the figure indicate a distance between the photon and the closest electron corresponding to three ECAL crystals. This has to be considered as the minimal distance between the two particles such that the photon is not included in the electron supercluster, thus not reconstructed. As the majority of the events are within this limit of three crystals, we can neglect for the moment the internal bremsstrahlung effect and leave it for a more evolved stage of the analysis.

5.4.3 Vertexing

Although accurate vertex fitting algorithms can be used to both select the electrons from the Higgs decay tree and to separate the signal from the different backgrounds, the approach adopted for this analysis is based on a less evolved quantity such as the transverse impact point parameters of the electron tracks. However, further improvements of the analysis are expected if the full information on the vertex is used. For this reason an event selection criteria based on common vertex compatibility among the electron tracks is under study. This will allow both to select the best four electron candidates which are supposed to come from the Higgs decay and to reject background events in which the electron tracks are not compatible with a single particle

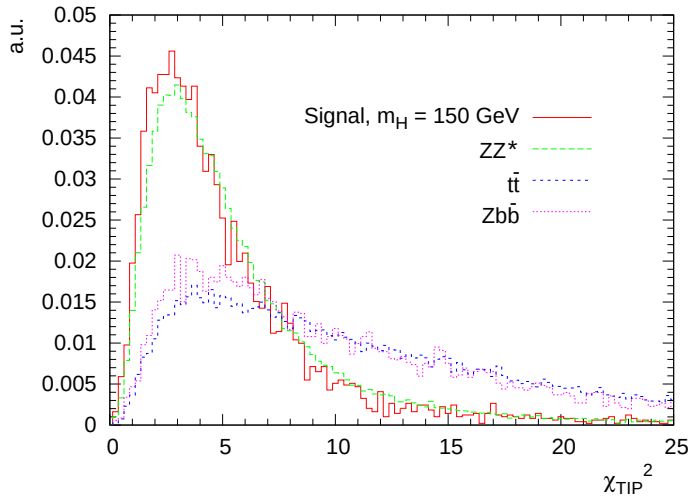

Figure 5.13: Distribution of χ^2_{TIP} (eq. 5.2) for signal and background.

decay.
The quantity chosen to estimate the vertex compatibility has been the chi-square of the four electrons tracks computed under the hypothesis of a common vertex. In particular, for each track its transverse impact parameter (TIP) is computed and subtracted from the transverse radius of the principal vertex of the events (R_T^V). The principal vertex is computed with a fit on all the tracks of the event.
The vertex compatibility is then given by

$$\chi^2_{\mathrm{TIP}} = \sum_{i=1}^{4} \left(\frac{\mathrm{TIP}_c^i}{\sigma^i_{\mathrm{TIP}_c}} \right)^2 , \tag{5.2}$$

where $\mathrm{TIP}_c = \mathrm{TIP} - R_T^V$ and σ_{TIP_c} is the error in determining TIP and R_T^V propagated to TIP_c.

The distribution of χ^2_{TIP} for signal events with $m_H = 150$ GeV/c^2 and the three kinds of background is given in figure 5.13.

Figure 5.14 shows the probability for the same data for $\chi^2(4)$ to be greater than the observed χ^2_{TIP}. The flatness of the distribution for the signal events indicates that χ^2_{TIP} is compatible with a chi-square distribution, and therefore that the events have statistical fluctuations around a common vertex.

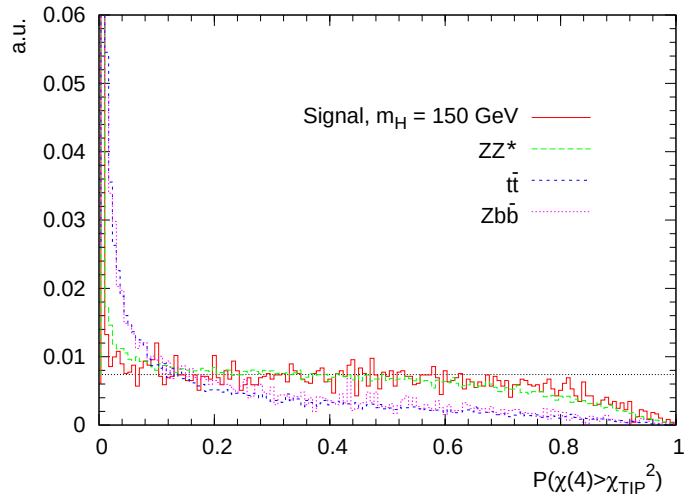

Figure 5.14: Probability of having a χ^2_{TIP} greater than $\chi^2(4)$ for signal and background. The flatness of the distribution is an indication for χ^2_{TIP} to be a χ^2 distribution, that is for the electron tracks to be compatible with a single vertex. This is true for signal and $ZZ^{(*)}$ events but not for the reducible background.

As expected, also $ZZ^{(*)}$ events show a good compatibility of the four electron tracks with a single vertex and the distributions are very similar to the signal ones. The reducible backgrounds, on the other hand, have fewer cases in which the tracks are compatible with a single vertex, since the electrons come from the decay of the quarks b and t.

5.4.4 Isolation and Electron Identification

As already noted, isolation is one of the most powerful criteria to distinguish between signal and reducible background events. The latter, in fact, have electrons in the final state which come from semileptonic decays of the quarks b and t and are often inside jets or close to hadronic tracks. It is therefore possible to apply criteria of isolation on the electron candidate in order to eliminate such cases.
Different choices for isolation algorithms combining the information of tracking and calorimetry are possible. In this analysis, the tracker only is used to apply a veto on the sum of the transverse momentum of the charged tracks inside a cone in $\Delta R = \sqrt{\Delta\eta^2 + \Delta\phi^2}$ around the electron track. The sum of

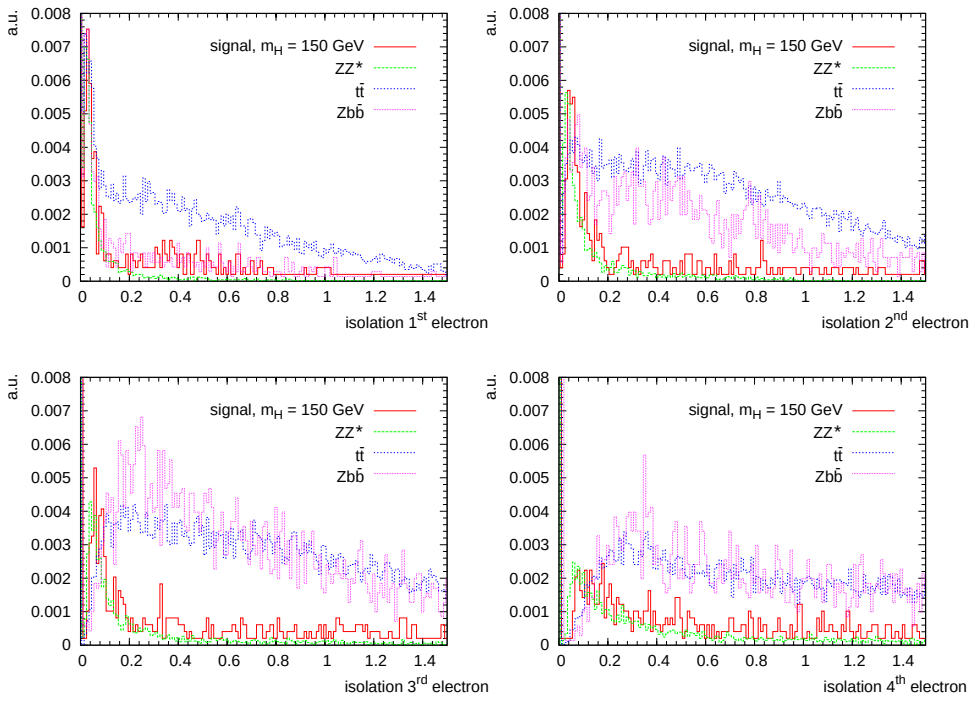

Figure 5.15: Distribution of the isolation as defined in the text for the four highest p_T electrons in the event.

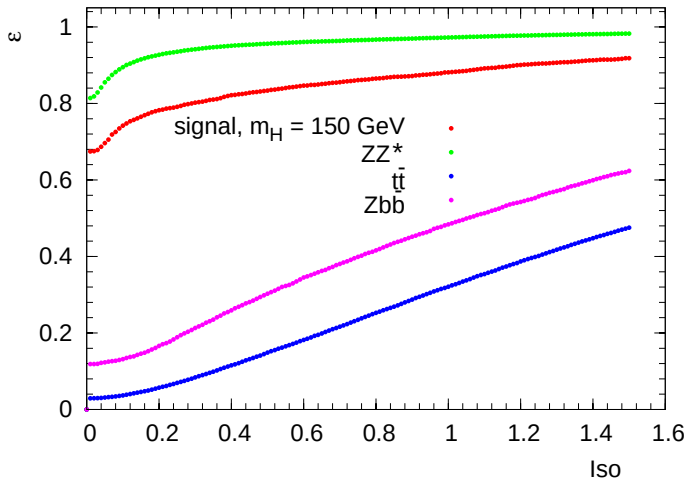

Figure 5.16: Efficiency for signal and background events requiring an isolation greater than Iso for the four highest p_T electrons in the event.

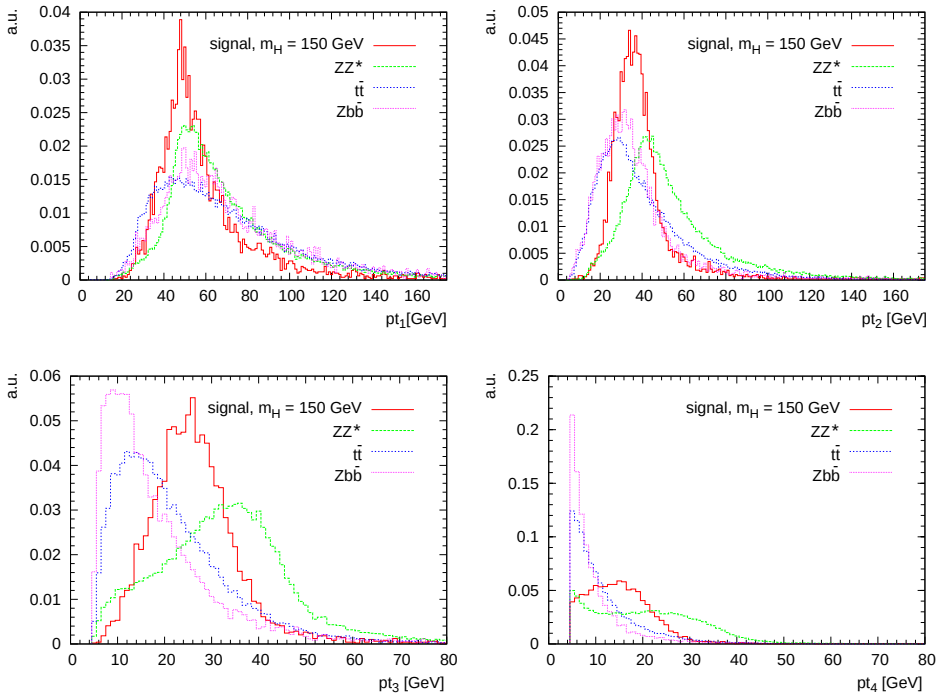

Figure 5.17: Transverse momentum distribution for the four highest p_T electrons in the event. The main differences in the signal and backgrounds spectra come from the two softest electrons

the p_T is normalized with respect to the electron momentum and the cone is chosen such that the electron track itself is not taken into account in the sum of the p_T of the tracks. The optimization of this algorithm is discussed elsewhere (Baffioni, 2005). The distribution of the isolation variable ($\mathcal{I}$) is shown in figure 5.15 for the four highest p_T electrons in the event. The results in the efficiency for signal and backgrounds are presented in figure 5.16. The efficiency has been computed requiring that all of the four highest p_T electrons have an isolation lower than a threshold. Only events in which there are at least four electrons with a transverse momentum greater than 5 GeV/c have been considered.

5.4.5 Kinematics of the reconstructed events

Differences in the kinematic of the events, already present at the generator level, transport well to the final reconstructed events. Figures 5.17 show

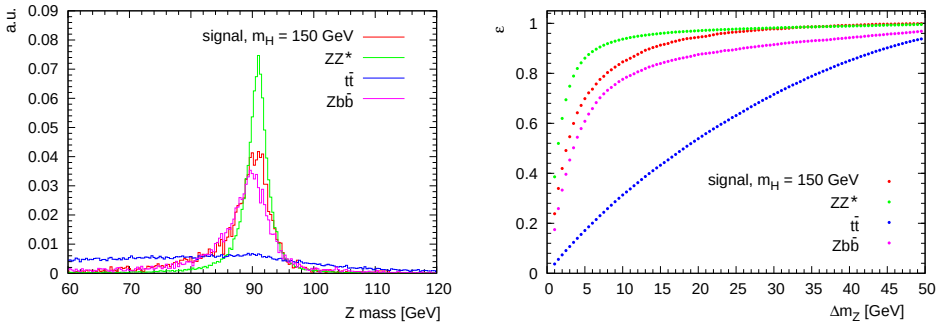

Figure 5.18: *Left*: distribution for the real Z mass, identified as the e^+e^- pair having the closest invariant mass to the Z peak. $ZZ^{(*)}$ event. *Right*: selection efficiency for signal and background events requiring the real Z mass to be in a window Δm_Z around the Z mass peak.

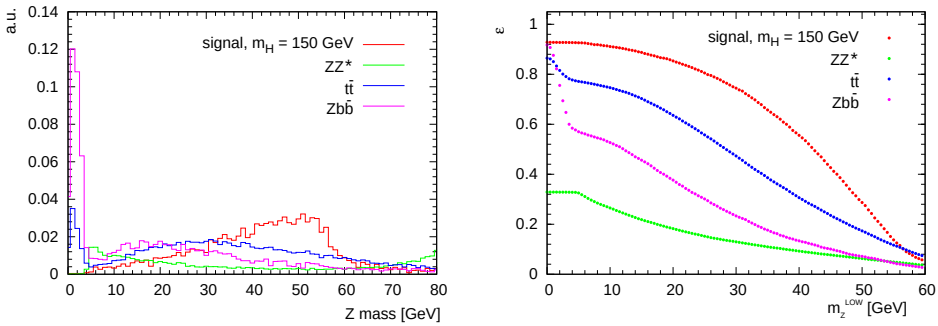

Figure 5.19: *Left*: distribution of the invariant mass of the e^+e^- pair identified as coming from the virtual Z of the event (see text for more details on the identification). *Right*: selection efficiency for signal and background events requiring the virtual Z mass greater than m_Z^{LOW} and lower than 70 GeV/c^2.

the transverse momenta distribution for the four highest p_T electrons in the event and agree with the distributions found when the true Monte Carlo information is considered.
In order to identify the electrons coming from the two different Z in a signal event, the following strategy has been adopted. First, the electron pair with the invariant mass closest to the Z mass peak has been identified as coming from the decay of the "real Z". The remaining pair with the highest invariant mass has then been selected and identified as coming from the decay of the "virtual Z". This strategy has been proven in previous analysis to have more than 90% of efficiency in correctly coupling the electrons.
Figure 5.18(a) shows the distribution of the real Z mass expected for signal and background events. The mass distribution of the second pair, which corresponds to the second Z boson in signal events, is shown in figure 5.19(a). The acceptance as a function of the size of a symmetric window centered on the Z mass peak is shown in figure 5.18(b). For the second Z distribution, the acceptance considering a variable lower limit and an upper limit fixed to 70 GeV/c^2 has been computed and is shown in figure 5.19(b).

5.5 Significance Definition

In experiment to search for new particles, the need arises to quantify the evidence for new physics signal over background. Theoretical prediction on the number of expected events for signal (N_S) and background (N_B) can be used to define the "significance" S as a characteristic of the observability of the phenomena. The methods to define the significance can be divided into event counting methods and likelihood methods, depending on whether they look for an excess of events in a predefined "signal-region" to determine N_S and N_B or if they take into account the shape of the distributions of signal and background (see for example (Bartsch and Quast, 2003)).
The most diffused counting methods use the following definition of significance:

$$\begin{aligned} S_1 &= \frac{N_S}{\sqrt{N_B}}, \\ S_{12} &= \frac{N_S}{\sqrt{N_S + N_B}}, \\ S_{cP} &= 2 \cdot (\sqrt{N_S + N_B} - \sqrt{N_B},) \end{aligned} \tag{5.3}$$

where, in particular, the last method is strictly valid only in the Gaussian limit of the Poisson distribution, that is for large N_S and N_B.

Likelihood methods, on the other hand, rely on hypothesis testing to estimate the significance of the discovery of new phenomena. A "null hypothesis", which assumes that the observed distribution of events is formed by background only, is compared via the Neyman-Pearson's test with an "alternative hypothesis" supposing that the observed distribution is due to the presence of both signal and background. A significance estimator can be defined as

$$S_{\mathrm{cL}} = \sqrt{2 \ln\ Q}, \tag{5.4}$$

where Q is given by the ratio of the likelihood of the fit to the data under the hypothesis of signal plus background and the likelihood of the fit under the background only hypothesis. In the large-statistics limit, S^2_{cL} is expected to follow a χ^2 distribution with a number of degrees of freedom given by the difference in the number of free parameters between the alternative and null hypothesis.

It turns out that if the likelihood method is applied to one bin only, namely the signal region, S_{cL} can also be used as a significance estimator in counting experiments. In this case, the ratio Q is given by the Poisson probability to observe N_{obs} events when $N_S + N_B$ are expected (alternative hypothesis) and the Poisson probability to observe N_{obs} events when N_B are expected (null hypothesis). This yields to the following expression for Q:

$$Q = \left(1 + \frac{N_S}{N_B}\right)^{N_{\mathrm{obs}}} \cdot e^{-N_S}. \tag{5.5}$$

Setting the expectation value of N_{obs} to $N_S + N_B$ completely define the likelihood estimator for event counting experiment.
For the flexibility of likelihood methods to be applied to counting experiment as well as fit of distribution shapes, the CMS collaboration as adopted S_{cL} as statistical tool to define the significance of new physics discovery.

5.6 Sequential Selection Analysis

According to the previous considerations, the developed strategy consists in a sequence of selections based on the variables illustrated above. These

selections can be divided in those for the electrons selection inside a given event and those for the signal to background separation, with a clear interplay between the two categories.
The analysis based on selections has been focused on the case of $m_H = 150$ GeV/c^2. The outline of the selection can be described as follows.

- Preselection to discard electrons which are very unlikely to come from the Higgs decay tree:
  - angular distance between the supercluster position and track at vertex: $\Delta\eta < 0.1$ and $\Delta\phi < 0.1$;
  - loose energy-momentum matching: $E/p < 3$;
  - ratio of energy measured in HCAL (H) and ECAL (E): $H/E < 3$;
  - loose isolation inside a cone $\Delta R < 0.15$:
    $\mathcal{I} = (\sum_{\text{tracks}} p_T)/(\text{electron } p_T) < 0.5$.
- Requirements of at least $2e^+$ and $2e^-$ in the event.
- Impact parameter: electrons with a significance on the impact parameter $\text{TIP}_c^i/\sigma_{\text{TIP}_c}^i$ lower than 10 are not considered as coming from a Higgs decay;
- Isolation: all the four electron tracks must have $\mathcal{I} < 0.1$
- Electron Identification:
  - ratio of energy measured in HCAL (H) and ECAL (E): $H/E < 0.1$;
  - angular distance from the supercluster and the last point of the electron track: $\Delta\phi < 0.1$ and $\Delta\eta < 0.01$;
  - ratio between the energy of the seed crystal and the momentum measured at the last track point greater than 0.5
  - sum of the energy deposited in arrays of crystals centered on the crystal with the maximum energy deposition: $3 \times 3/5 \times 5 > 0.5$;
  - shower spread in η: $\sigma_{\eta\eta} < 0.05$;
- Kinematics:
  - transverse momenta of the four highest p_T electrons greater than 7, 10, 15, 20 GeV/c respectively;

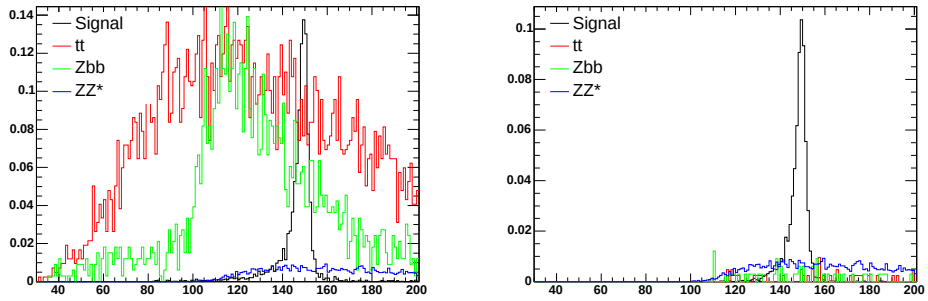

(a) (b)

Figure 5.20: Four electron invariant mass distribution for signal and background events (a) after the preselection and (b) after the selections has been applied.

- first Z mass in the Z mass peak within 15 GeV/c^2;
- second Z mass greater than 15 GeV/c^2 and lower than 70 GeV/c^2.

The starting point after the preselection step is shown in figure 5.20(a). The application of the selections then gives the distribution shown in figure 5.20(b).

The significance has been computed considering the events with the invariant mass of the four electrons inside a window between 145 GeV/c^2 and 155 GeV/c^2. The effect of the different selections is reported in table 5.3. The final number of signal events has been of 10.93 for the signal and 1.95 for the sum of the three considered backgrounds (1.4 for ZZ^*, 0.19 for $t\bar{t}$, 0.36 for $Zb\bar{b}$). The obtained significances, according to the definitions given in section 5.5 are then

$$S_1 = 7.8 \qquad S_{12} = 3.0 \qquad S_{cL} = 5.1. \tag{5.6}$$

5.7 Neural Network Analysis

In order to discriminate between signal and background events, strategies combining all the available information at a time are *a priori* more efficient than approaches based on simple selections on the main event variables, even when cuts optimization procedure are involved. Global event classification

Acc. in %	Signal	ZZ^*	$t\bar{t}$	$Zb\bar{b}$
L1	99.7	97.5	96.3	90.2
HLT	97.4	94.7	77.5	79.0
Presel. & $2e^+2e^-$	55.9	50.2	11.6	16.4
TIP	97.1	96.9	71.1	79.8
Isolation	90.3	93.5	20.1	35.1
El. ID	87.5	87.5	57.5	71.7
p_T	81.7	80.0	22.5	22.2
Z mass	93.4	97.7	32.9	90.9
Z^* mass	95.2	16.2	67.6	38.8
$4e$ inv. mass	83.7	9.33	12.0	8.33
TOTAL	29.1	0.51	0.005	0.034

Table 5.3: Relative acceptances with respect to the generation preselection for the different selections for a Higgs boson mass hypothesis of $m_H = 150$ GeV/c^2 (see the text for more detail).

based on pattern recognition procedures can exploit event topologies that would hardly be distinguished by cuts. Neural Networks provide one of such global approaches to the event selection.

5.7.1 Neural Network Structure

The main idea behind the neural networks is to address a problem with a large number of logic units highly interconnected between them rather than with a single unit performing very fast serial processing. The complexity of the network can supply a deficit in the computing rate, exactly as the human brain can perform certain computation (e.g. pattern recognition and perception) much better than a computer, even if the latter is typically six orders of magnitude faster than the former.
An elementary introduction to the neural networks will be briefly given in the following paragraphs. For a detailed and exhaustive description see for example (Haykin, 1994).
The basic structure of a neural network is a neuron, that is a single information processing unit. A neuron is composed of four basic elements (figure 5.21).

- A set of *synapses*, each of which connects the neuron with another

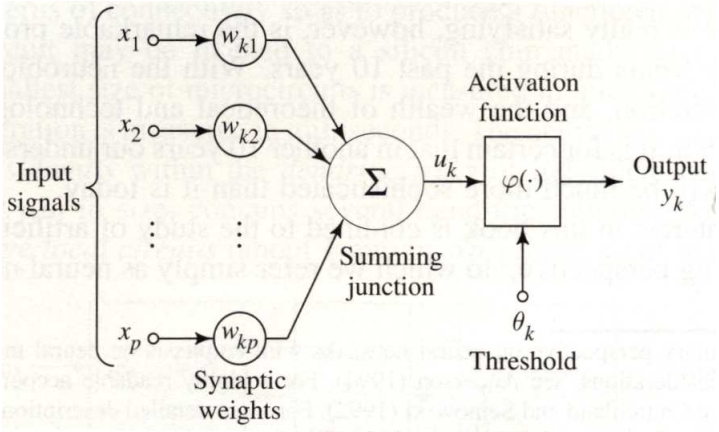

Figure 5.21: Schema of a neuron, the basic information processing unit of a neural network.

neuron and is characterized by a *weight*. Specifically, the signal x_j in input to the synapses j connected to the neuron k is multiplied by the synaptic weight w_{kj}.

- An *adder* which sum the input signals weighted by the respective synapses of the neuron.

- An *activation function*, to limit the output of a neuron in a finite interval, typically $[0, 1]$ or $[-1, +1]$.

- An external *bias* (*threshold*) to positively (negatively) shift the input of the activation function.

Mathematically speaking, a neuron can be described by the pair of equations

$$\begin{aligned} u_k &= \sum_{j=1}^{N} \omega_{kj} x_j, \\ y_k &= \varphi(u_k - \vartheta_k). \end{aligned} \tag{5.7}$$

The first equation describes the neuron input u_k as a linear combination of input signals x_j. The second represents the neuron output y_k as the results of the activation function $\varphi(\cdot)$ on an input which is biased by the constant

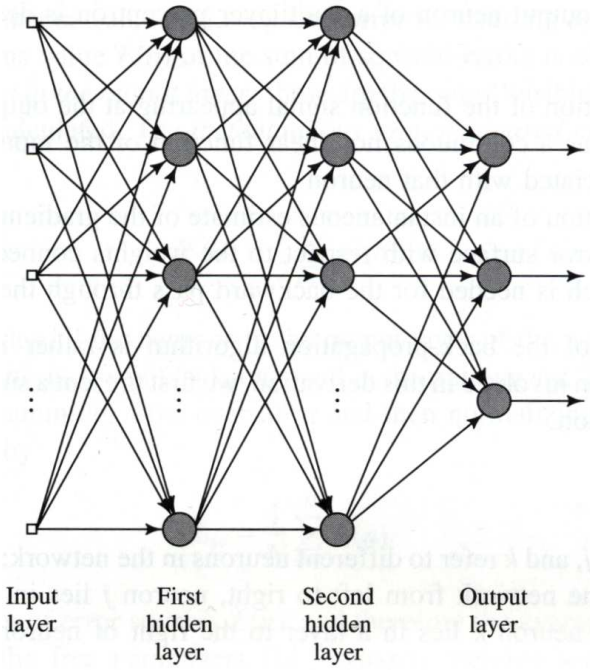

Figure 5.22: Schema of a multilayer perceptron with two hidden layers.

ϑ_k. Examples of threshold functions are:

$$\varphi(z) = \begin{cases} 0 & , \quad z < 0 \\ 1 & , \quad z \geq 0 \end{cases} \quad , \qquad \varphi(z) = \begin{cases} 0 & , \quad z \leq -\frac{1}{2} \\ z & , \quad -\frac{1}{2} < z < \frac{1}{2} \\ 1 & , \quad z \geq \frac{1}{2} \end{cases} \quad , \tag{5.8}$$

$$\varphi(z) = \frac{1}{1 + e^{-az}} \quad , \quad a > 0,$$

that is a logic function, a piecewise-linear function and a sigmoid.

Neurons are interconnected with each other through links called synapses, which allow the propagation of the information through the network. The networks can have many different structures depending on the use they are dedicated to. Here, the description will be limited to the so-called multilayer perceptron, a widely used class of feed-forward networks which will be employed in the following analysis.

5.7.2 Multi-Layer Perceptrons

As depicted in figure 5.22, a multilayer perceptron typically consists of a set of input neurons that constitute the input layer, one or more hidden layers of computation nodes and an output layer. The information propagates through the network in a forward direction on a layer-by-layer basis. The optimal choice of the synaptic weights is made with a learning procedure which consists in supervising the network while it processes a given sample of input signals. Firstly, the input signals are processed through the network up to the output layers (forward pass). Secondly, the network response is compared to a desired response to make an error signal. The signal of the error is then propagated backward through the network and the weights of the synapses are adjusted so as to make the actual network response move closer to the desired response (back-propagation step).
The back-propagation is the implementation of an adaptive procedure to optimize the network performance. From a pragmatic point of view, much care has to be taken in order to ensure the convergence of the procedure while keeping the network sufficiently general to be successfully applied to inputs other than the training sample. In other words, the network has to be efficient but does not have to specify its performance to the training sample.

5.7.3 Neural Networks and Probability

In this section, it will be shown how a feed-forward neural network can be used to approximate probability densities for an event to be signal or background. A mathematical notation will be introduced to represent a general feed-forward neural network which, in this case, is supposed to have n real-valued inputs $\mathbf{X} = (x_1, \ldots, x_n)$ (forming a feature vector) and one single output $\mathbf{Y} = y_1$.
The network can be viewed as a function F of the k weights ω_i of the synapses $\mathbf{\Omega} = (\omega_1, \ldots, \omega_k)$ that maps the vector $\mathbf{X}$ into $\mathbf{Y}$ (therefore $F \equiv F(\mathbf{X}, \mathbf{\Omega})$).
As mentioned in the previous section, the back-propagation mechanism is based on the minimization, with respect to the synapses weights $\mathbf{\Omega}$, of an error $\mathscr{E}$ for the network output. If R_i is the desired response for a given input $\mathbf{X}_i$, the error $\mathscr{E}$ is defined as

$$\mathscr{E}_N = \frac{1}{N} \sum_{i=1}^{N} \left[F(\mathbf{X}_i, \mathbf{\Omega}) - R_i \right]^2 , \tag{5.9}$$

where i is the index of the set of inputs. In a typical particle physics experiment, the set of inputs corresponds to the set of variables characterizing an event in the detector. The main task to perform is the separation of signal events S from background events B. The classes S and B are assumed to be mutually exclusive and their union is composing the complete domain $\mathcal{D}$ for the network function F.
Discriminating signal from background events is equivalent to finding a hyper-plane (decision boundary) in the domain $\mathcal{D}$, which is partitioned into signal and background regions. In this representation of the event selection, optimal selections analyses are limited to constraints on 1-dimensional distributions which define a hyper-cube having the best signal to background ratio. In general, however, there is a considerable overlap between the 1-dimensional distributions for signal and background, so the hyper-cube does not corresponds to the best performance achievable in the signal/background separation. On the other hand, neural networks allow to work directly in the whole domain $\mathcal{D}$, and thereby to exploit correlations between the feature vectors in a much better way.
In order to prove that the output of a neural network can be interpreted as a Bayesian probability, the error $\mathscr{E}$ can be rewritten by separating two terms, one relative to signal events and the other to background events:

$$\mathscr{E}_N = \frac{N_S}{N}\frac{1}{N_S}\sum_{S=1}^{N_S}(F-s)^2 + \frac{N_B}{N}\frac{1}{N_B}\sum_{B=1}^{N_B}(F-b)^2, \tag{5.10}$$

where N_S and N_B are respectively the number of signal and background events (and $N = N_S + N_B$). The desired output R_i has been set to s for signal events, to b for background events.
The limit for $N \to \infty$ is then considered. The ratios N_S/N and N_B/N go to the signal and background cross-section, defining the *a priori* probability of an event of being a signal event ($P(S)$) or a background event ($P(B)$). The two sums of equation 5.10 become two integrals whose measure is determined by the distribution of the feature vectors:

$$\mathscr{E} = P(S)\int d\mathbf{X}P(\mathbf{X}|S)(F-s)^2 + P(B)\int d\mathbf{X}P(\mathbf{X}|B)(F-b)^2, \tag{5.11}$$

where $P(\mathbf{X}, S)$ and $P(\mathbf{X}, B)$ are the probability density functions for signal and background respectively.
Using the Bayes' theorem on conditional probability it is possible to con-

struct the *a posteriori* probability for signal and background:

$$\begin{aligned} P(S|\mathbf{X}) &= P(\mathbf{X}|S)\frac{P(S)}{P(\mathbf{X})} \\ P(B|\mathbf{X}) &= P(\mathbf{X}|B)\frac{P(B)}{P(\mathbf{X})} \end{aligned} \quad , \tag{5.12}$$

where

$$P(\mathbf{X}) = P(\mathbf{X}|S)P(S) + P(\mathbf{X}|B)P(B). \tag{5.13}$$

$P(S|\mathbf{X})$ and $P(B|\mathbf{X})$ represent the probability density that an event giving a measured feature vector $\mathbf{X}$ belongs to signal or background, which is exactly the probability of interest for event classification. By using the equations 5.12 and 5.13 in equation 5.11, after a few steps one obtains

$$\mathscr{E} = \int d\mathbf{X} P(\mathbf{X})[F^2 - 2\,F\,G(\mathbf{X},s,b)] + \int d\mathbf{X} P(\mathbf{X})[s^2 P(S|\mathbf{X}) + b^2 P(B|\mathbf{X})], \tag{5.14}$$

where

$$G(\mathbf{X},s,b) \equiv s^2 P(S|\mathbf{X}) + b^2 P(B|\mathbf{X}). \tag{5.15}$$

By completing the expression of the first integrand to a square and after rearranging terms, one obtains

$$E(F) = \mathbf{E}[(F-G)^2] + \mathbf{E}[(s-G)(G-b)], \tag{5.16}$$

where the expectation operator $\mathbf{E}[\varphi]$ on the generic function φ has been defined as

$$\mathbf{E}[\varphi] \equiv \mathbf{E}_S[\varphi] + \mathbf{E}_B[\varphi], \tag{5.17}$$

with

$$\mathbf{E}_\xi[\varphi] \equiv P(\xi) \int d\mathbf{X} P(\mathbf{X}|\xi)\varphi(\mathbf{X}) \quad , \quad \xi = S, B. \tag{5.18}$$

The meaning of equation 5.16 is that if a function $F(\mathbf{X},\Omega)$ can be found, provided a large enough number of signal and background events, a minimization of $\mathscr{E}_N(F)$ leads to the solution

$$F(\mathbf{X},\boldsymbol{\Omega}) = G(\mathbf{X},s,b) \equiv sP(S|\mathbf{X}) + bP(B|\mathbf{X}). \tag{5.19}$$

Therefore, by using the equivalence $P(S|\mathbf{X}) + P(B|\mathbf{X}) = 1$, the following approximations for the probability of an event to be a signal event S or a background event B given the features vector $\mathbf{X}$:

$$\begin{aligned} P(S|\mathbf{X}) &= \frac{F-b}{s-b} \\ P(B|\mathbf{X}) &= \frac{s-G}{s-b}. \end{aligned} \tag{5.20}$$

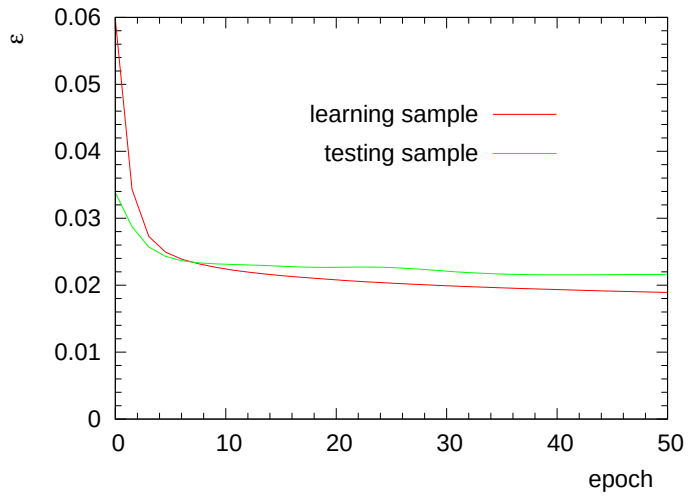

Figure 5.23: Example of trend of the neural network error $\mathscr{E}$ defined in equation 5.10.

It is then possible to use the previous expressions in common methods of hypothesis testing.

5.7.4 Neural Network analysis

The variables used as inputs for the neural network have been chosen among those exposed in section 5.4. In particular, a preselection requiring at least two electrons and two positrons with a transverse momentum greater than 5 GeV/c has been applied to the events. Then the inputs for the neural network have been:

- the four electrons p_T;
- the isolation for each of the electrons;
- the invariant mass of the real and virtual Z as defined in section 5.4.5;
- the vertex compatibility.

For each mass hypothesis for the Higgs boson, three networks have been built in order to estimate the probability for an event to be signal or one of the three backgrounds ($ZZ^{(*)}$, $t\bar{t}$, $Zb\bar{b}$).

The networks have been trained for each sample of signal and background with 150 iterations on 2000 events, which have then been excluded from the

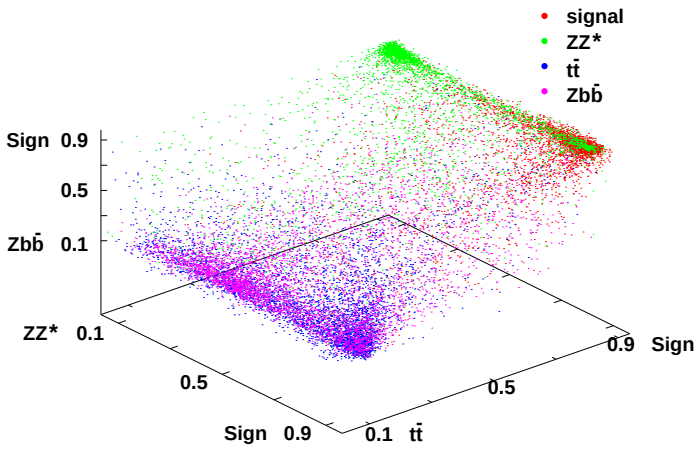

Figure 5.24: Distribution of the neural network outputs for signal and background events. On the axis the output of the three network for the hypothesis of signal against the three different backgrounds is reported for each event. As expected the signal events are classified near 1 by each network and populate the region around $(1, 1, 1)$. $ZZ^{(*)}$ events are classified as signal from the two network built for $t\bar{t}$ and $Zb\bar{b}$ events but are well discriminated by the $ZZ^{(*)}$ network. The reducible background is well classified by each neural network.

analysis. An example of the trend of the error $\mathscr{E}_N$ (eq. 5.10) as a function of the network iteration (epoch) is shown in figure 5.23.

Examining in more detail the Higgs mass point at $m_H = 150$ GeV/c^2, the network output for the signal and the different background samples is given in figure 5.25.

In the analysis, the probability for an event to be signal or one of the three different backgrounds has been computed for each event. The events, therefore, populate a 3-dimensional space where each coordinate represents one of the probabilities. Signal events would populate the region near the point $(1, 1, 1)$ while background events should have at least one of the probability close to 0. Figure 5.24 shows the 3-dimensional distribution of the events according to their probability. The axis (x, y, z) correspond respectively to the probability of being signal or $(ZZ^{(*)}), t\bar{t}, Zb\bar{b}$. Signal events populate the region near $(1, 1, 1)$, as expected. $ZZ^{(*)}$ events are instead considered

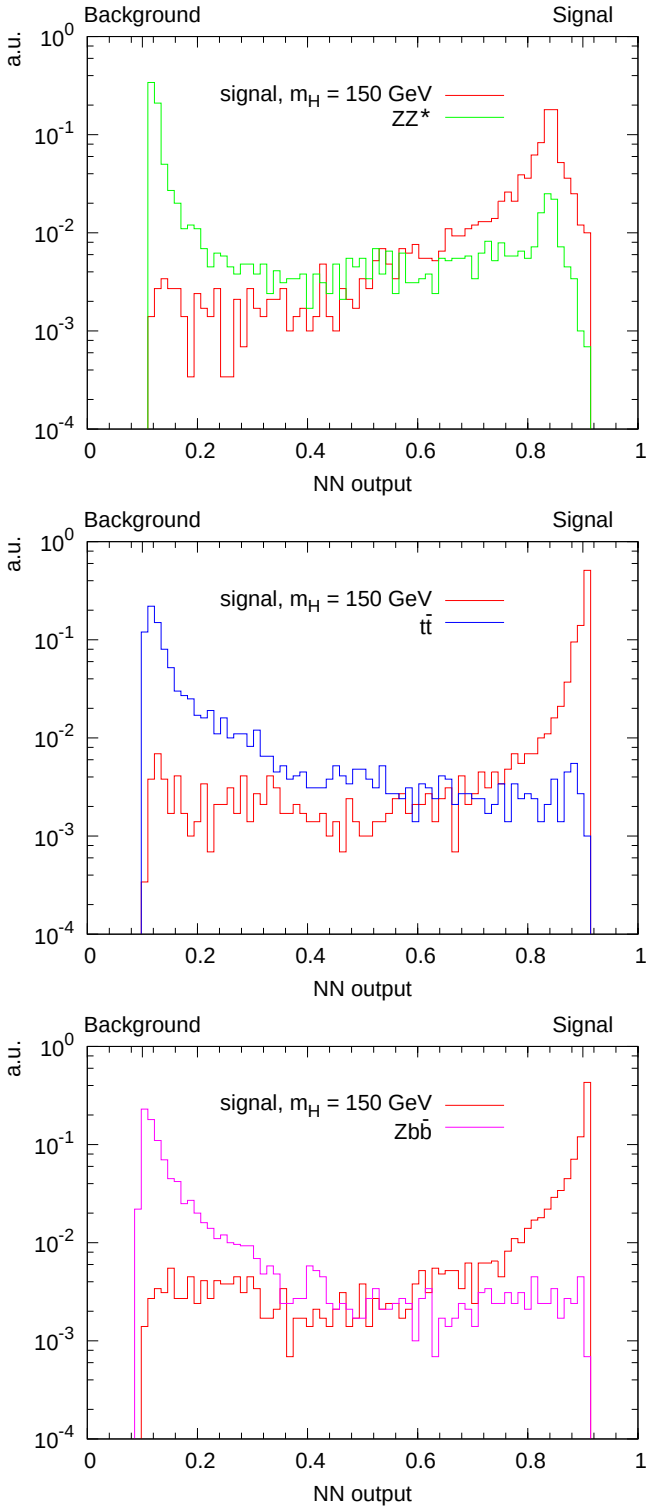

Figure 5.25: Output of the three neural networks, to distinguish signal from $ZZ^{(*)}$, $t\bar{t}$, $Zb\bar{b}$.

signal-like from the networks built against the $t\bar{t}$ and $Zb\bar{b}$ hypothesis, and are pushed on the $(x, 1, 1)$ plane. However, the network built against the $ZZ^{(*)}$ hypothesis pushes them near 0, so they finally populate the region near $(1, 1, 0)$. Analogous considerations can be done for the two other background sources and demonstrate the good discrimination achievable with the neural networks.
For the final separation of signal and background, the optimal region in the 3-dimensional space has been selected along with the optimal Higgs mass window. The optimization procedure has been made using the package MINUIT (James, 1994).

The results are shown in figure 5.26, where the event distribution before the neural network application is also shown for comparison. The expected number of events for the Higgs mass point $m_H = 150$ GeV/c^2 is of 12.21 for the signal and 1.35 for the background, to be compared to the results of the selection-based analysis of 10.93 events for the signal and 1.95 for the background. An improvement both in signal efficiency and background rejection is clearly visible.
The significances for the Higgs boson discovery are then

$$S_1 = 10.5 \qquad S_{12} = 3.3 \qquad S_{cL} = 6.2. \tag{5.21}$$

The improvement on the significance with the respect to the same mass point in the selection-based analysis is remarkable and equal to about 20%.

This analysis has been performed also for all the Higgs boson mass point from 120 GeV/c^2 to 200 GeV/c^2 in step of 10 GeV/c^2 and for the point at 115 GeV/c^2. In table 5.4 the result of the measurements of the Higgs boson mass and width is reported.

The expected number of signal and background events is shown in figure 5.27. The results for the significance are shown in figure 5.28. The integrated luminosity needed to reach a significance of 5 for all the Higgs mass hypothesis is shown in figure 5.29.

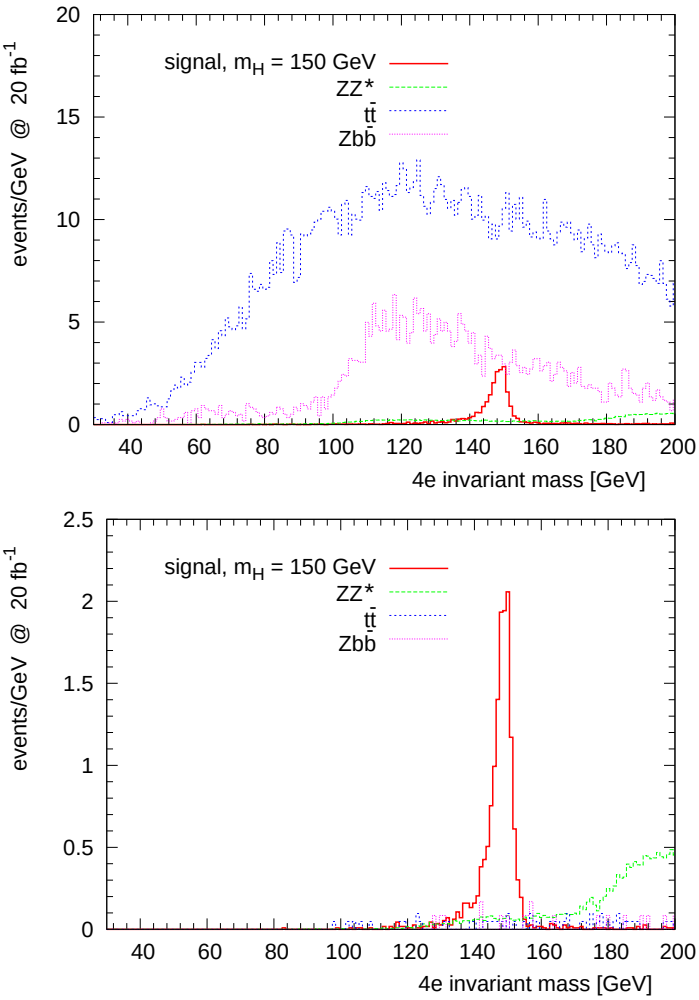

Figure 5.26: Expected distribution for the four electron invariant mass. *Top*: after the preselection. *Bottom*: after the neural network analysis has been applied to separate signal and background.

m_H^{true} [GeV/c^2]	Γ_H^{true} [GeV/c^2]	m_H^{rec} [GeV/c^2]	Γ_H^{rec} [GeV/c^2]
115	$3.22 \cdot 10^-3$	113.91	1.84
120	$3.60 \cdot 10^-3$	119.17	1.67
130	$4.94 \cdot 10^-3$	128.74	1.96
140	$8.06 \cdot 10^-3$	138.73	2.06
150	$1.66 \cdot 10^-2$	148.82	2.17
160	$7.72 \cdot 10^-2$	158.90	2.20
170	$3.83 \cdot 10^-1$	168.77	2.36
180	$6.28 \cdot 10^-1$	178.99	2.54
190	1.03	188.64	2.86
200	1.42	198.83	3.27

Table 5.4: Higgs boson reconstructed mass and width, as a results of a Gaussian fit on the peak of the invariant mass distribution of the four final state electrons. The reconstructed quantities are compared with the true values.

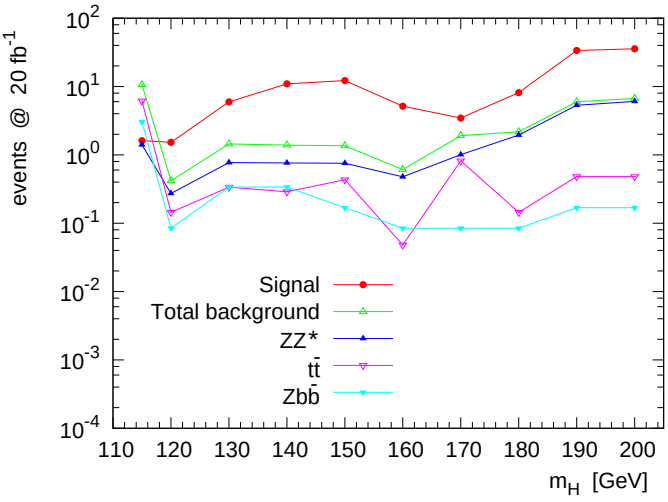

Figure 5.27: Number of expected events for signal and background after the neural network selection.

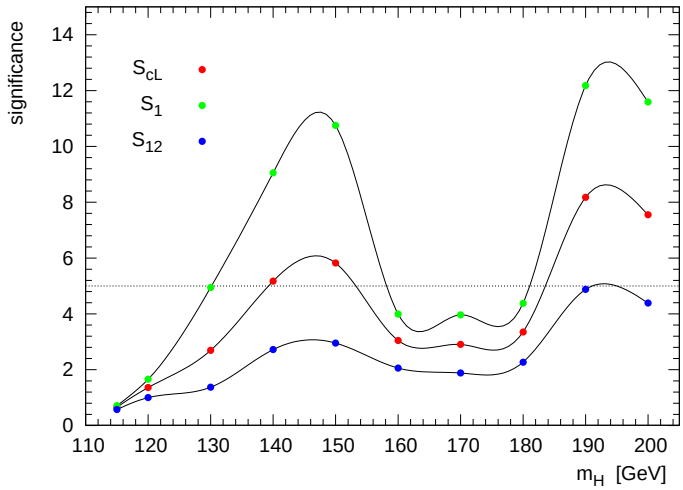

Figure 5.28: Significance achievable for an integrated luminosity of 20 fb^{-1} for different Higgs mass hypothesis.

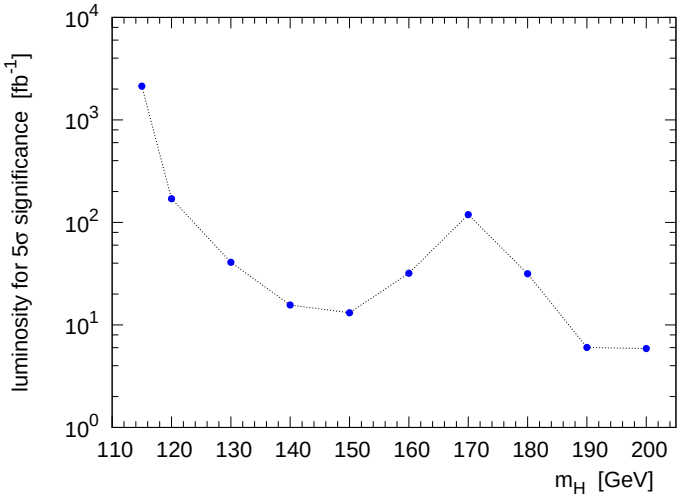

Figure 5.29: Integrated luminosity needed to reach a significance $S_{\mathrm{cL}} > 5$ for each Higgs mass hypothesis.

5.8 Conclusions

This chapter presents the analysis of the Higgs decay channel $H \to ZZ^{(*)} \to 4e$. The analysis has been performed for Higgs mass hypothesis ranging from 115 GeV/c^2 to 200 GeV/c^2. The signal and the relevant background for this channel (event with $ZZ^{(*)}$, $t\bar{t}$ and $Zb\bar{b}$ as intermediate states) have been generated and simulated using the full CMS detector simulation.
In order to have a complete view of the kinematical and topological properties of signal and background, the analysis has concentrated on the Higgs mass point at 150 GeV/c^2. A standard approach based on sequential selections has shown the possibility to reach a statistical significance greater than 5 in one year of LHC operating at 20 fb^{-1} of integrated luminosity. In parallel, a neural network approach has been developed to optimize at best the event characteristics for the background rejection while keeping a high signal efficiency. On the Higgs mass point at 150 GeV/c^2, the results of the neural network analysis show an improvement in the statistical significance with respect to sequential selections. The neural network analysis has been extended to mass points ranging from 115 GeV/c^2 to 200 GeV/c^2 and has shown that a discovery claim could be made in this channel for Higgs masses between $\sim$ 130 GeV/c^2 and $\sim$ 145 GeV/c^2 and greater than $\sim$ 185 GeV/c^2.

With respect to the previous analysis in this channel, the study presented in this thesis is based on a more accurate description and simulation of the detector and has brought a significant contribution in the electron reconstruction focused on low p_T electrons. The classification of the quality of the electron energy measurement has been successfully applied to obtain the best estimate of the electron four momentum at the interaction point. Moreover, a division of the electron into classes can be successfully applied to optimize the criteria of the electron identification.
Furthermore, the new analysis based on a neural network has shown the possibility to significantly improve the separation of signal events from the background and is leading the way towards optimized analysis techniques.

Bibliography

Almadov, A., *et al.*. (2000), *Top Quark Physics*, International Workshop on QCD, hep-ph/0003033.

Baffioni, m. (2005), *Electron Selection and Identification in CMS*, CMS AN, Note in preparation.

Barberio, E. and Was, Z. (1994), *PHOTOS: A Universal Monte Carlo for QED radiative corrections. Version 2.0*, Comput. Phys. Commun., **vol. 79**, pp. 291–308.

Bartsch, V. and Quast, G. (2003), *Expected signal observability at future experiments*, CMS NOTE 2005/004.

Beneke, M. *et al.* (2000), *Top quark physics.* `hep-ph/0003033`.

Choi, S. Y., Miller, D. J., Muhlleitner, M. M. and Zerwas, P. M. (2003), *Identifying the Higgs spin and parity in decays to Z pairs*, Phys. Lett., **vol. B553**, pp. 61–71. `hep-ph/0210077`.

Djouadi, A., Kalinowski, J. and Spira, M. (1998), *HDECAY: A program for Higgs boson decays in the standard model and its supersymmetric extension*, Comput. Phys. Commun., **vol. 108**, pp. 56–74. `hep-ph/9704448`.

Frixione, S. and Webber, B. R. (2004), *The MC@NLO 2.3 event generator.* `hep-ph/0506182`.

Godinović, N. (2003), *Optimization of the Properties of Electromagnetic Calorimeter of CMS detector and the Possibility of Measuring the Higgs Bosono Spin and Parity*, Ph.D. thesis, University of Zagreb.

Haykin, S. (1994), *Neural networks: a comprehensive fundation*, Macmillan College Publishing Company.

James, F. (1994), *MINUIT - Function Minimization and Error Analysis*, CERN Program Library Long Writeup D506.

Meridiani, P. (2003), *Optimization of the discovery potential of the Higgs Boson in the decay channel* $H \to ZZ^{(*)} \to 2e^+2e^-$ *with the CMS detector*, Ph.D. thesis, Università degli Studi di Roma "La Sapienza".

ORCA (2004), *Object-oriented Reconstruction for CMS Analysis*, http://cmsdoc.cern.ch/orca/.

Prosper, H. B. (1993), *Some Mathematical Comments on Feed-Forward Neural Networks*, DØNote 1606.

Pukhov, A. *et al.* (1999), *CompHEP: A package for evaluation of Feynman diagrams and integration over multi-particle phase space. User's manual for version 33.* `hep-ph/9908288`.

Puljak, I. (2000), *CMS discovery potential for the Higgs boson in the* $H \to ZZ^{(*)} \to 4e^{\pm}$ *decay channel. Contribution to the construction of the CMS electromagnetic calorimeter*, Ph.D. thesis, Université Paris VI.

Sjostrand, T., Lonnblad, L. and Mrenna, S. (2001), *PYTHIA 6.2: Physics and manual.* `hep-ph/0108264`.

Spira, M. (2005), *http://people.web.psi.ch/spira/proglist.html.*

Conclusions

The work presented in this thesis has focused on the electromagnetic calorimeter (ECAL) of the CMS detector and on its relevance in the discovery of the Higgs boson in the channel $H \to ZZ^{(*)} \to 4e$, for which the performance of ECAL is essential.
The calorimeter has been studied in detail both with test beam data and with simulated data using a complete description of the CMS detector.

The test beam studies have been directed to the analysis of the electronic noise and to the amplitude reconstruction of the signal acquired from the calorimeter. A procedure to evaluate the spectral power density of the signals has been determined using the Maximum Entropy method. This method allows to have a continuous approximation of the noise spectral power, contrary to traditional methods which typically have only discrete estimates depending on the number of samples of the digitized signal.
The amplitude has been reconstructed for two different cases: one in which signals saturate the electronic readout of the calorimeter and another in which a non-white noise is present in the electronics. For the first case, an amplitude reconstruction method using non-saturated samples on the signal rise has been developed and tested, showing the possibility to reach precision better than 2(5)% in the amplitude determination up to energies of 2(3) TeV.
To estimate the signal amplitude in the case of non-white noise in the electronics, on the other hand, a reconstruction method in the frequency domain has been developed. This method achieves a performance comparable to that of the reconstruction methods operating in the time domain (which have been officially adopted in CMS) and constitutes a valid alternative to them when no white noise in the electronics is present.

Using the full CMS detector simulation, a detailed study of the electron reconstruction inside CMS has pointed out and analyzed the problems which affect the measurements of the electron energy with the calorimeter.

A particular care has been given to electrons of low transverse momentum ($p_T < 30$ GeV/c) for which these effects become crucial. Namely the bremsstrahlung effect, which is due to the tracking material in front of the calorimeter and constitutes the major problem, has been examined in depth. A classification of the electron "quality" based on tracking and calorimetry observables has been proposed to distinguish cases in which the electron brings all of its initial energy to the calorimeter from cases in which part (or all) of its energy is lost in bremsstrahlung and never recollected by the calorimeter. According to the information from the electron classification, a scaling of the energy has been computed in order to correct the measurement to be as close as possible to the initial electron energy. A parametrization of the energy resolution for the different electron classes has allowed to not only evaluate the error associated with the energy measurement but also to optimally combine the measurement of the calorimeter with the absolute value of the momentum measured by the tracker. This combination yields the best possible estimate of the four momentum of the electron at the interaction point.

These results have been directly applied in the analysis of the Higgs boson signal in the channel $H \to ZZ^{(*)} \to 4e$, where the electron and positron coming from the Z with the lowest mass have typically low transverse momentum and can take advantage of the previous studies on the electron reconstruction.
The simulation of signal and background has been performed using the full CMS detector simulation and two basic approaches have been adopted for the analysis. One s based on sequential selections and the other is based on a neural network.
While the first provides the necessary understanding of the event topology and characteristics of the signal with respect to the background, ensuring the robustness of the analysis, the second exploit at best all this information in order to perform an optimized rejection of background events maintaining high efficiency for the signal.
Although the analysis does not yet include a complete evaluation of the consequences related to the theoretical uncertainties on the production cross-section for signal and background, and of possible detector effects (e.g. miscalibration of the electromagnetic calorimeter, tracker alignment etc.), the results show that a significance greater than 5 can be reached both with standard selections and with a neural network approach for a Higgs mass hypothesis of 150 GeV/c^2. In particular, the neural network analysis ex-

tended to mass points ranging from 115 GeV/c^2 to 200 GeV/c^2 shows that a discovery claim could be made in this channel for Higgs masses between $\sim$ 130 GeV/c^2 and $\sim$ 145 GeV/c^2 and greater than $\sim$ 185 GeV/c^2.

Acknowledgements

The work of this thesis has been carried out within the "da Vinci" Ph.D. collaboration program between the Università di Milano-Bicocca and the Ecole Polytechnique de Palaiseau. This collaboration could not be possible without the support of Antonino Pullia and Maurice Haguenauer, who started it and gave me the opportunity to work inside the two institutes. Their constant support has been a great motivation all along the work.
I wish to thank Yves Sirois and Tommaso Tabarelli de Fatis, for their valuable supervision. They always opened my mind on the different physics issues and challenges that we faced within this work, as well as on the meaning and methods of the research in physics.
I am grateful to my referees Philippe Bloch and Ezio Menichetti, for their careful reading of the manuscript and very interesting and stimulating suggestions.
To Stefano Ragazzi, Marco Paganoni and Maurizio Bonesini for their advise in the different stages of my work, Claude Charlot and Ivica Puljak for the very pleasant working time together (even during the "night-shifts").
To Matteo Cacciari for his suggestions on theoretical issues, Filippo Resnati and Stéphane Bimbot for the fruitful discussion on the Neural Networks and more, to Amandine Cagnioncle for the language support.
To the LLR and Milano-Bicocca groups, from the "jeunes" to the more experienced physicists and computer scientists.
A special thank to Alessandra and Matteo for their support. And to Maya and Stéphane and his parents, who I feel all like my french family. Last but certainly not least, who always supported me, sharing my feelings and my every-day life, and do not need an explicit mention.

Résumé

Le Modèle Standard des intéractions électrofaibles est en excellent accord avec les expériences, mais il ne donne pas encore de réponses satisfaisantes à plusieurs questions de physique fondamentale, dont la plus importante est l'origine de la masse des particules qui composent l'Univers. Un des méchanismes proposés pour expliquer la nature massive des particules (et donc pour justifier la brisure spontanée de la symmétrie $SU(2)_L \times U(1)_Y$ qui est à la base du Modèle Standard) se fonde sur l'existence d'un champ scalaire qui se manifeste sous forme d'une particule scalaire massive (nommée boson de Higgs) qui n'a pas encore été découverte.
Les recherches menées au cours de l'expérience LEP2 ont imposé une limite inférieure ($m_H > 114.4$ GeV/c^2 à 95% C.L.) et une limite supérieure ($m_H < 237$ GeV/c^2 à 95% C.L.) sur la masse du boson de Higgs, et elles ont indiqué 114 GeV/c^2 comme meilleure valeur d'ajustément aux données experimentales.
Le travail présenté dans cette thèse a été mené au sein de la collaboration de CMS (Compact Muon Solenoid). CMS est une des deux expériences à vocation généraliste (avec ATLAS) qui vont être installées au LHC (le Large Hadron Collider en construction au CERN de Genève) conjointement à deux expériences dédiées à l'étude de la physique du quark b (LHCb) et des ions lourds (ALICE).

LHC est un collisionneur hadronique (pp) avec une énergie nominale de 14 TeV dans le centre de masse et une luminosité prouvant atteindre $10^{34}\,\mathrm{cm}^{-2}\mathrm{s}^{-1}$. Une de ces motivations principales est la recherche du boson de Higgs, particule responsable de la brisure spontanée de symétrie dans le Modèle Standard et donc de la nature massive des bosons de jauge ($W^{\pm}$ et Z) et des fermions présents dans la nature. Les limites actuelles sur la masse du boson de Higgs, obtenues par des recherches directes et indirectes au cours de l'expérience LEP (L*arge* E*lectron* P*ositron collider*), semblent montrer qu'il s'agirait d'une particule "légère": dans ce cas, le canal de découverte

favori (pour $m_H \lesssim 140\,\text{GeV}$) est $H \to \gamma\gamma$, grâce à la facilité de sélection des événements au-dessus d'un bruit de fond principalement hadronique. Par ailleurs, un canal d'une importance remarquable, capable non seulement de mener à la découverte du boson de Higgs (pour $m_H \gtrsim 140$ il est le second par ordre d'importance après $H \to WW^*$) mais aussi d'en mesurer quelques unes de ses caractéristiques fondamentales pour en comprendre la nature (spin et parité) est le canal $H \to ZZ^{(*)} \to 4\ell$. Ce canal, qui considére en particulier un état final constitué de quatre électrons, combiné à la désintégration du boson de Higgs en deux photons, donne à la calorimétrie électromagnétique du détecteur CMS un rôle d'une extrême importance.

Cette thèse se focalise sur la caractérisation du calorimétre électromagnétique de CMS (ECAL) à partir de données provenant de test en faisceau et de simulations détaillées du détecteur, ainsi que sur l'étude des performances du détecteur attendues de CMS pour la découverte du boson de Higgs dans la canal $H \to ZZ^{(*)} \to 4\ell$.

Après une introduction théorique du Modèle Standard (chapitre 1) le collisionneur LHC et le détecteur CMS sont présentés dans le chapitre 2.

Le troisième chapitre montre les résultats des études sur le bruit électronique présent dans la chaîne d'acquisition du signal de ECAL et sur les méthodes de reconstruction de ce signal. En particulier, en ce qui concerne le premier aspect, la puissance spectrale du bruit de fond a été évaluée en utilisant la méthode "Maximum Entropy". À l'invers des techniques conventionnelles qui ne donnent qu'une information discrète liée au nombre d'échantillons de numérisation du signal, cette méthode permet d'obtenir une estimation continue de la puissance spectrale du bruit de fond, en simplifiant la recherche du bruit de fond cohérent.
Les études de reconstruction du signal ont été focalisés sur les cas où il sature la chaîne électronique. La méthode développée utilise l'information des échantillons qui ne sont pas saturés pour reconstruire l'amplitude des signaux. Elle a démontré la possibilité de parvenir à une précision de l'ordre du pourcent jusqu'à des énergies de quelques TeV.
Une méthode de reconstruction de l'amplitude dans l'espace des fréquences a aussi été développée, pour le cas où un traitement détaillé du bruit électronique serait nécessaire.

Le quatrième chapitre présente des études sur la reconstruction des

électrons dans CMS. Le but est d'analyser les principaux effets concernant la mesure de l'énergie des électrons en utilisant le calorimètre électromagnétique. En particulier, l'effet du bremsstrahlung, dûe au matériel du trajectomètre situé devant le calorimètre, est le principal problème à résoudre, puisqu'il cause une perte considérable de l'énergie des électrons qui donne souvent des problèmes de reconstruction. Pour déterminer la qualité de la mesure d'énergie de l'électron, on a proposé une classification des électrons basée sur des observables du calorimètre et du trajectomètre. En accord avec cette classification, on a calibré l'échelle en énergie pour la ramener le plus près possible de l'énergie initiale de l'électron. Une paramétrisation de la résolution en énergie a permis d'attribuer une erreur à la mesure et donc de combiner l'information du calorimètre avec celle du trajectomètre pour atteindre la meilleure estimation de l'impulsion de l'électron au point d'interaction. Une attention particulière a été portée sur les électrons de basse impulsion transverse, qui constituent un large pourcentage des électrons venant de la désintégration du boson de Higgs dans le canal $H \to ZZ^{(*)} \to 4\ell$.
En utilisant l'estimation finale de l'énergie de l'électron, le pic de masse du boson de Higgs est trouvé à la valeur attendue et la résolution sur la masse du boson est améliorée.

Le cinquième chapitre montre les résultats de l'analyse de la désintégration du boson de Higgs $H \to ZZ^{(*)} \to 4\ell$.
L'analyse a été mené pour des hypothèses de masse du Higgs de 115 GeV/c^2 à 200 GeV/c^2. Le signal et le bruit de fond pour ce canal (événements avec $ZZ^{(*)}$, $t\bar{t}$, $Zb\bar{b}$ comme états intermédiaires) ont été générés et simulés en utilisant la simulation complète du détecteur CMS.
Pour acceder à une vision complète des propriétés cinématiques et topologiques du signal et du bruit de fond, l'analyse s'est concentrée sur un point de masse du Higgs de 150 GeV. Une approche standard basée sur des sélections séquentielles a montré la possibilité d'atteindre une significance statistique plus grande que 5 en prenant pour LHC une luminosité intégrée de 20 fb^{-1}.
En parallèle, un réseau de neurones a été développé pour optimiser la séparation du signal et du bruit de fond. La significance obtenue par cette méthode est méilleure que celle obtenue par les sélections séquentielles.
Le technique des réseaux de neurones a aussi été employée pour analyser tout les point de masse, et a montré qu'une découverte du boson de Higgs avec une luminosité intégrée de 20 fb^{-1} peut être réalisée pour des masses entre $\sim$ 130 GeV/c^2 et $\sim$ 145 GeV/c^2 et plus grandes que $\sim$ 185 GeV/c^2.

Riassunto

Il Modello Standard delle interazioni elettrodeboli è in eccellente accordo con le verifiche sperimentali, ma non è in grado di fornire delle risposte soddisfacenti a diverse domande fondamentali, di cui la più importante è l'origine della massa delle particelle che compongono l'Universo. Uno dei meccanismi proposti per spiegare la natura massiva delle particelle (e dunque per giustificare la rottura spontanea della simmetria $SU(2)_L \times U(1)_Y$ sulla quale è costruito il Modello Standard) si fonda sull'esistenza di un campo scalare che si manifesta sotto forma di una particella scalare massiva (detta bosone di Higgs) la cui esistenza non è ancora stata provata.
Le accurate ricerche condotte nel corso dell'esperimento LEP2 hanno imposto un limite inferiore ($m_H > 114.4$ GeV/c^2 à 95% C.L.) ed uno superiore ($m_H < 237$ GeV/c^2 a 95% C.L.) alla massa del bosone di Higgs, indicando 114 GeV/c^2 come miglior valore risultante dalla procedura di adattamento ai dati sperimentali.
Il lavoro presentato in questa tesi è stato condotto nell'ambito della collaborazione CMS (Compact Muon Solenoid). CMS è uno dei due esperimenti a carattere generale (insieme ad ATLAS) che verranno installati a LHC (Large Hadron Collider) situato presso i laboratori del CERN di Ginevra, congiuntamente a due esperimenti finalizzati allo studio della fisica del quark b (LHCb) e degli ioni pesanti (ALICE).

LHC è un collisionatore adronico (pp) con un'energia nominale di 14 TeV nel centro di massa ed una luminosità prevista di 10^{34} cm^{-2}s^{-1}. Una delle motivazioni principali per questa macchina è la ricerca del bosone di Higgs, particella responsabile della rottura spontanea della simmetria elettrodebole nel Modello Standard e quindi della natura massiva dei bosoni di gauge ($W^{\pm}$ e Z) e dei fermioni presenti in natura. I limiti attuali sulla sua massa ottenuti da ricerche dirette ed indirette nel corso dell'esperimento LEP propendono per una particella "leggera": in questo caso, il canale di scoperta favorito (per $m_H \lesssim 140$ GeV) è $H \to \gamma\gamma$, grazie alla facilità di selezione degli eventi

dal fondo principalmente adronico. Tuttavia un canale d'importanza notevole, in grado non soltanto di portare alla scoperta del bosone di Higgs (per $m_H \gtrsim 140$ è il secondo canale più importante dopo $H \to WW^*$) ma anche di misurarne le caratteristiche principali per comprenderne la natura (spin e parità) è il canale $H \to ZZ^{(*)} \to 4\ell$. Tale canale, considerando in particolare uno stato finale costituito da quattro elettroni, combinato al decadimento del bosone di Higgs in due fotoni, attribuisce alla calorimetria elettromagnetica un ruolo di fondamentale importanza.

Questa tesi si concentra sulla caratterizzazione del calorimetro elettromagnetico di CMS (ECAL), sia utilizzando dati provenienti da test su fascio sia con simulazioni dettagliate del rivelatore, e sullo studio delle prestazioni attese da CMS per la scoperta del bosone di Higgs nel canale $H \to ZZ^{(*)} \to 4\ell$.

Dopo un'introduzione teorica al Modello Standard (capitolo 1) vengono presentati il collisionatore LHC ed il rivelatore CMS (capitolo 2).

Il terzo capitolo illustra i risultati degli studi sul rumore elettronico presente nella catena d'acquisizione del segnale e sui metodi di ricostruzione del segnale. In particolare, per quanto concerne il primo aspetto viene proposto il metodo "Maximum Entropy" per la valutazione della potenza spettrale del rumore. Contrariamente alle tecniche convenzionali che forniscono un'informazione discreta legata al numero di campionamenti nella digitalizzazione del segnale, questo metodo permette di avere una stima continua della potenza spettrale, semplificando la ricerca di rumore coerente.
Gli studi di ricostruzione del segnale sono volti ai casi in cui il segnale satura la catena elettronica di rilettura. Il metodo sviluppato utilizza l'informazione dei campionamenti non saturati per ricostruire l'ampiezza dei segnali e ha dimostrato la possibilità di raggiungere precisioni dell'ordine della parte su cento fino ad energie di qualche TeV.
Si è inoltre sviluppato un metodo di ricostruzione dell'ampiezza nello spazio delle frequenze, nel caso in cui si renda necessario un trattamento specifico del rumore di fondo.

Il quarto capitolo presenta gli studi sulla ricostruzione degli elettroni in CMS e si prefigge di analizzare gli effetti principali riguardanti la misura dell'energia degli elettroni col calorimetro elettromagnetico. In particolare, il problema principale è costituito dalla bremmstrahlung che, dovuta

alla presenza del materiale del tracciatore davanti al calorimetro, causa spesso problemi di ricostruzione. Per determinare la qualità della misura d'energia, si è proposto una classificazione degli elettroni fondata su osservabili del calorimetro e del tracciatore. Seguendo questa classificazione si è fissata la scala di energia delle misure, riportandola il più vicino possibile all'energia iniziale dell'elettrone. Una parametrizzazione della risoluzione energetica ha permesso d'attribuire un errore alla misura e di combinare, quindi, l'informazione del calorimetro con quella del tracciatore per avere la miglior stima dell'impulso dell'elettrone nel punto d'interazione. Un'attenzione particolare è stata posta sugli elettroni di basso momento trasverso, che costituiscono una larga frazione degli elettroni provenienti dal decadimento del bosone di Higgs nel canale $H \to ZZ^{(*)} \to 4\ell$.
Utilizzando la stima finale dell'energia dell'elettrone, il picco di massa del bosone di Higgs risulta intorno al valore atteso e la risoluzione sulla massa del bosone viene migliorata.

Il quinto capitolo mostra i risultati dell'analisi del decadimento del bosone di Higgs $H \to ZZ^{(*)} \to 4\ell$.
L'analisi è stata condotto per ipotesi di massa dell'Higgs da 115 GeV/c^2 a 200 GeV/c^2. Il segnale ed il fondo per questo canale (eventi con $ZZ^{(*)}$, $t\bar{t}$, $Zb\bar{b}$ nello stato intermedio) sono stati generati e simulati utilizzando la simulazione completa di CMS.
Al fine di avere una visione completa delle proprietà cinematiche e topologiche del segnale e del fondo, l'analisi si è concentrata sul punto di massa del bosone di Higgs a 150 GeV. Un approccio standard basato su selezioni successive ha mostrato la possibilità di raggiungere una significanza statistica maggiore di 5 considerando per LHC una luminosità integrata pari a 20 fb^{-1}. In parallelo si è sviluppata una rete neurale per ottimizzare la separazione del segnale dal fondo mantenendo un'elevata efficienza di selezione degli eventi di segnale. La significanza ottenuta da questo metodo ha migliorato i risultati ottenuti dalle selezioni successive.
La tecnica delle reti neurali è stata applicata anche allo studio di tutti i rimanenti punti di massa, mostrando come la scoperta del bosone di Higgs sia possibile a luminosià integrate pari a 20 fb^{-1} per masse comprese tra ~ 130 GeV/c^2 e ~ 145 GeV/c^2 e maggiori di ~ 185 GeV/c^2.